uOttawa

L'Université canadienne
Canada's university

FACULTÉ DES ÉTUDES SUPÉRIEURES ET POSTOCTORALES

uOttawa

L'Université canadienne
Canada's university

FACULTY OF GRADUATE AND POSDOCTORAL STUDIES

Barbara Minor

AUTEUR DE LA THÈSE / AUTHOR OF THESIS

M.A.Sc. (Civil Engineering)

GRADE / DEGREE

Department of Civil Engineering

FACULTÉ, ÉCOLE, DÉPARTEMENT / FACULTY, SCHOOL, DEPARTMENT

Barbs (Submerged Groynes) for River Ben Bank Protection: Application of Three-dimensional Numerical Model

TITRE DE LA THÈSE / TITLE OF THESIS

Dr. C. Rennie

DIRECTEUR (DIRECTRICE) DE LA THÈSE / THESIS SUPERVISOR

Dr. R. Townsend

CO-DIRECTEUR (CO-DIRECTRICE) DE LA THÈSE / THESIS CO-SUPERVISOR

EXAMINATEURS (EXAMINATRICES) DE LA THÈSE / THESIS EXAMINERS

Dr. I. Nistor

Dr. R. Droste

Dr. P. Van Geel

Gary W. Slater

Le Doyen de la Faculté des études supérieures et postdoctorales / Dean of the Faculty of Graduate and Postdoctoral Studies

Barbs (Submerged Groynes) for River Bend Bank Protection: Application of a Three-Dimensional Numerical Model

Barbara Minor

Thesis submitted to the
Faculty of Graduate and Postdoctoral Studies
In partial fulfillment of the requirements
For the Master of Applied Science degree in Civil Engineering

The Ottawa-Carleton Institute for Civil Engineering
Department of Civil Engineering
Faculty of Engineering
University of Ottawa

Your file Votre référence
ISBN: 978-0-494-25807-1
Our file Notre référence
ISBN: 978-0-494-25807-1

Abstract

A three-dimensional numerical model was used to examine the turbulent flow field and associated sediment transport due to a series of barbs in a channel bend. It was observed that the results simulated by the model showed good agreement with measured data and adequately simulated the important features of sediment transport. Statistical analysis of the predicted and measured sediment transport results found an average regression coefficient of determination of 0.8 for the 90 and 135° channels. It was found that the predicted velocity data followed expected trends. The following objectives were achieved: validation of the application of a three-dimensional numerical model to bend sections of a channel containing barbs; simulation of the effects of different arrangements of barb groups; and analysis of the data to determine the relation of the flow field to associated scour and deposition in a complex fluvial environment. These novel data are useful for improved analyses of the bank protection capabilities of these structures and for the development and improvement of design guidelines.

Acknowledgments

I would like to thank both of my thesis supervisors, Dr. Rennie and Dr. Townsend, for their support and guidance. I am grateful to Dr. Rennie for his graduate level courses and all of his advice. These were invaluable for the completion of this thesis.

I also wish to thank my parents, Cameron and Kathryn, for their continuous support and encouragement.

Table of Contents

List of Figures

List of Tables

List of Symbols

a	reference level
c	sediment concentration
cm	centimeters
$c_\mu, c_{\varepsilon 1}, c_{\varepsilon 2}, \sigma_k, \sigma_\varepsilon$	turbulence model closure coefficients
D	sediment particle diameter
D_{50}	median particle size by weight
D_*	scaled particle parameter
e_{ij}	rate of strain tensor
F_R	resistance force
g	gravitational acceleration
h	hours
H	horizontal distance
h	barb weir section height
k	turbulent kinetic energy
km	kilometers
L	weir length
m	meters
mm	millimeters
m/s	meters/second
m^3/s	cubic meters per second
n	total number of data points
N/m	Newtons per square meter
P	pressure
$\overline{P}$	time-averaged mean pressure
p	instantaneous pressure fluctuation
q_b	volumetric bedload transport rate
r^2	regression coefficient of determination
R_h	hydraulic radius
R_{ij}	Reynolds stresses
s	seconds
S	slope
Sc	Schmidt number
S_s	sediment specific gravity
T	transport stage parameter
t	time
U_i	fluid velocity
$\overline{U_i}$	time-averaged mean velocity
u_*	grain shear velocity
u_{*cr}	critical shear velocity
u_i	instantaneous fluid velocity fluctuation
V	vertical distance
W	barb width
w	fall velocity of sediments

x_i	position vector
y_o	channel forming flow depth
y_s	scour depth measured without barbs in the channel
y_s'	scour depth with barbs in the channel

Greek Symbols

δ_{ij}	Kronecker delta
γ	specific weight of water
μ	dynamic fluid viscosity
ν	kinematic fluid viscosity
ν_T	eddy viscosity
ρ	density of water
σ_{ij}	pressure and viscous stresses
τ_o	mean shear stress applied by the fluid on the bed
τ_b	near-bank boundary shear stress
τ_{bc}	critical bank shear stress
τ_{cr}	critical shear stress
θ	barb alignment angle
Γ	diffusion coefficient

1.0 Introduction

1.1 Problem Statement

The erosion of streambanks alters channel morphology, threatens structures and land adjacent to the channel, and increases the sediment load in many channels. The increased sediment load can have several negative impacts, including destruction of aquatic habitat, and reduced navigability of the channel. Streambank erosion is influenced by numerous factors. These include water discharge, sediment load, bed and bank material properties, channel slope, channel geometry, and vegetation. In addition, human activities in the vicinity of a channel may instigate or hasten morphological changes (Przedwojski and Blazejewski, 1995).

Streambank erosion is of particular concern in channel bends due to the complex interaction between the flow field and sediment transport. In channel bends, secondary currents are generated primarily by the channel curvature. In combination with the primary downstream flow, the secondary currents create a helical flow through the channel. Furthermore, the secondary currents introduce a transverse shear that changes the shear distribution across a channel section and subsequently influences the sediment distribution. As a result of this complex flow field, there is an increase in the shear stress and erosion in the outer bank region. The most common location of erosion on non-cohesive banks is at the toe of the bank. Traditional methods of streambank protection, such as revetments and emergent groynes, were developed to prevent erosion along the outer bank of channel bends. These methods have generally provided sufficient

protection. However, they have typically been uneconomical and, in some cases, have forfeited the diversity of the stream's ecosystem. This has led to the development of innovative and cost effective bank protection methods, such as barbs, a type of submerged groyne (USDA, 2005).

Barbs are low-profile linear structures that are primarily used to prevent the erosion of stream banks. They are a variation of a groyne, similar to spur dikes and bendway weirs. Historically, groyne structures have been built such that the groyne emerges out of the water and is overtopped only at the highest flows. More recently, there has been interest in low-profile submerged groynes, such as barbs, because they require less material to construct and are less obtrusive. Barbs are typically anchored, in series, to the outside bank in stream bends and extend in an upstream direction from the bank into the flow. A series of barbs is designed to redirect flow away from the outer stream bank and disrupt the velocity gradient and shear stress distribution close to the outer bank. As a result of this disruption the location of the thalweg shifts away from the outside bank. In addition, this process counteracts the secondary currents formed due to channel curvature. Therefore, unlike other traditional methods of bank protection, barbs are a proactive type of bank protection that attack the erosion mechanism. Furthermore, a zone of low velocity, and low Froude number, is generated upstream of the barb structure along the outer bank. Thus a series of barbs, installed correctly, protects the outer bank from erosion and promotes sediment deposition. In addition to this, it has been observed that vortices are generated at the tips of the barbs creating local scour holes that can enhance aquatic habitat (Shields et al., 1998).

Many field installations of these structures have been performed using good judgment and experience rather than following specific criteria. In addition, there is limited documentation of the design criteria that have been used for the field installation of barbs and for the long-term performance of these structures. Recently there has been an effort to provide recommendations and guidelines for the design of barbs (e.g., Matsuura and Townsend, 2004 and USDA, 2005). However, it must be noted that these are only suggestions. There remains a need for studies to identify the optimum barb dimensions, spacing, and orientations in the bend flow field for different bend geometries and hydraulic conditions. Furthermore, an understanding of the interaction between the complex flow field and the sediment transport through the channel bend is required in order to predict the long-term performance of these structures. The purpose of this study was to simulate the turbulent flow field and associated scour and deposition of the bed sediments due to a series of barbs in both a 90° channel bend and a 135° channel bend using a three-dimensional numerical model. The numerical model was calibrated to the scour measurement data obtained from a previous physical laboratory study (Matsuura, 2004).

1.2 Objectives

The objectives of this study were to:

- Validate the application of a three-dimensional numerical model to moveable-bed bend sections of a hydraulically narrow rectangular channel containing barbs;

- Simulate the effects of different arrangements of barb groups in the bend section by varying channel bend angle, barb alignment, and the location of the barbs; and
- Analyze the data to determine the relation of the flow field to associated scour and deposition in a complex fluvial environment.

These novel data are useful for improved analyses of the bank protection capabilities of these structures and for the development and improvement of design guidelines.

2.0 Background

2.1 Governing Equations

The governing equations of fluid flow are based on the **law of conservation of mass** (continuity) and **Newton's second law of motion** (conservation of momentum). For this study it is assumed that the fluid is incompressible, of constant density, and Newtonian. Thus, viscosity is assumed to be constant and well defined.

The **law of conservation of mass** states that mass cannot be created or destroyed. Although matter can change form, its mass must remain constant. Therefore, the rate of mass flow into a control volume must equal the net rate of mass flow out of the control volume, expressed as

$$\frac{\partial \rho}{\partial t} + \frac{\partial (\rho u_i)}{\partial x_i} = 0 \tag{2.1}$$

For an incompressible and non-diffusive flow with a constant density the law of conservation of mass becomes

$$\frac{\partial U_i}{\partial x_i} = 0 \tag{2.2}$$

The Navier-Stokes equation is a differential form of **Newton's second law of motion**. For an incompressible fluid it is expressed as

$$\rho\left(\frac{\partial U_i}{\partial t}+U_j\frac{\partial U_i}{\partial x_j}\right)=\frac{\partial \sigma_{ij}}{\partial x_j}+\rho g_i \tag{2.3}$$

where g_i is the gravitational acceleration vector and σ_{ij} includes pressure and stress terms.

For an incompressible Newtonian fluid

$$\sigma_{ij}=-P\delta_{ij}+2\mu e_{ij} \tag{2.4}$$

where P is the pressure, δ_{ij} is the Kronecker delta, μ is the viscosity, and e_{ij} is the rate of strain tensor. The Kronecker delta is defined by

$$\delta_{ij}=\begin{Bmatrix}0 & for\ i\neq j\\ 1 & for\ i=j\end{Bmatrix} \tag{2.5}$$

The rate of strain tensor is expressed as

$$e_{ij}=\frac{1}{2}\left(\frac{\partial U_i}{\partial x_j}+\frac{\partial U_j}{\partial x_i}\right) \tag{2.6}$$

Therefore, the Navier-Stokes equation for an incompressible Newtonian flow can be written as

$$\rho\left(\frac{\partial U_i}{\partial t} + Uj\frac{\partial U_i}{\partial x_j}\right) = -\nabla P + \mu\nabla^2 U_i + \rho g_i \qquad (2.7)$$

The Navier-Stokes equation (Equation 2.7) and the law of conservation of mass equation (Equation 2.2) and their derivations can be found throughout numerous literature including Schlichting (1979), Rodi (2000), and Bernard (2002). They are non-linear partial differential equations that cannot be solved analytically. Direct numerical simulation (DNS) has been used successfully to solve these equations. However, these solutions are limited to low Reynolds numbers and simple boundary conditions by the current capacity of computer technology. Furthermore, the solutions are limited by the accuracy of the boundary conditions. In natural channels, the boundary conditions are complex, and may be difficult to define sufficiently for DNS.

One method used to simplify the Navier-Stokes equations utilizes Reynolds averaging (Reynolds, 1895). For turbulent flows the instantaneous velocity, U_i, and pressure, P, can be decomposed into time-averaged mean quantities, $\overline{U_i}$ and $\overline{P}$, and instantaneous fluctuations, u_i and p. Overbars represent mean quantities. This is expressed as

$$U_i(t) = \overline{U_i} + u_i \text{ ; and} \qquad (2.8)$$

$$P(t) = \overline{P} + p. \qquad (2.9)$$

Equations 2.8 and 2.9 are then substituted into the Navier-Stokes equation (Equation 2.7) and the law of conservation of mass equation (Equation 2.2). The Reynolds-averaged law of conservation of mass equation becomes

$$\frac{\partial \overline{U_i}}{\partial x_i} = 0 \tag{2.10}$$

The resulting Reynolds-averaged Navier-Stokes (RANS) equation can be expressed as

$$\frac{\partial \overline{U_i}}{\partial t} + \overline{U_j}\frac{\partial \overline{U_i}}{\partial x_j} = -\frac{1}{\rho}\frac{\partial \overline{P}}{\partial x_i} + \frac{1}{\rho}\frac{\partial}{\partial x_j}\left(\mu\frac{\partial \overline{U_i}}{\partial x_j} - \rho\overline{u_i u_j}\right) + \rho g_i \tag{2.11}$$

where $\overline{u_i u_j}$ are the Reynolds stresses.

The Reynolds stresses represent the flux of momentum due to turbulence. They are a symmetric tensor and thus introduce six new unknown terms;

$$\overline{u_i u_j} = \begin{bmatrix} \overline{u^2} & \overline{uv} & \overline{uw} \\ \overline{vu} & \overline{v^2} & \overline{vw} \\ \overline{wu} & \overline{wv} & \overline{w^2} \end{bmatrix}. \tag{2.12}$$

A turbulence closure model is required to solve for these values.

2.2 Turbulence Modeling

In Section 2.1 it was shown that the details of a flow field can be described by the Navier-Stokes equations. However, due to the limited capacity of computers at this time, DNS is an expensive option that has only been achieved for uncomplicated flows with low Reynolds numbers and simple boundary conditions. For this study, and for most engineering problems, the fluid motion is turbulent, the boundary conditions are complex, and the channel geometry is complicated.

The RANS equations use mean values to provide a simplified method for solving the Navier-Stokes equations. The resulting RANS equations (2.10 and 2.11) introduce additional unknown terms, identified as the Reynolds stresses (Equation 2.12), which represent the flux of momentum due to turbulence. As a result there are more unknown terms than equations. This introduces the turbulence "closure" problem. A turbulence closure model is used to provide additional equations which relate the Reynolds stresses to the other mean flow variables. A two-equation model combining the eddy-viscosity concept (Boussinesq, 1877) with the κ-ε Model (Jones and Launder, 1972) is used in this study.

The eddy-viscosity concept assumes that behaviour of the turbulent stresses is similar to the behaviour of the viscosity stresses. Using this method the Reynolds stresses are modeled as

$$R_{ij} = -\overline{u_i u_j} = \nu_T \left(\frac{\partial U_i}{\partial x_j} + \frac{\partial U_j}{\partial x_i} \right) \tag{2.13}$$

where R_{ij} represents the Reynolds stresses and $\left(\frac{\partial U_i}{\partial x_j} + \frac{\partial U_j}{\partial x_i} \right)$ is the rate of strain of the mean fluid. For high Reynolds numbers the eddy viscosity, ν_T, can be expressed as

$$\nu_T = c_\mu \frac{k^2}{\varepsilon} \tag{2.14}$$

where c_μ is given in Table 2.1, ε is the turbulence dissipation, and the turbulent kinetic energy, k, is given as

$$k = \frac{1}{2} \overline{u_i u_i} \, . \tag{2.15}$$

The turbulent kinetic energy equation is commonly modeled as

$$\frac{\partial k}{\partial t} + U_j \frac{\partial k}{\partial x_j} = \nu_T \frac{\partial U_i}{\partial x_j} \left(\frac{\partial U_i}{\partial x_j} + \frac{\partial U_j}{\partial x_i} \right) + \frac{\partial}{\partial x_j} \left[\left(\nu + \frac{\nu_T}{\sigma_k} \right) \frac{\partial k}{\partial x_j} \right] - \varepsilon \tag{2.16}$$

and the dissipation equation is modeled as

$$\frac{\partial \varepsilon}{\partial t} + U_j \frac{\partial \varepsilon}{\partial x_j} = \frac{\partial}{\partial x_j}\left[\left(\nu + \frac{\nu_T}{\sigma_\varepsilon}\right)\frac{\partial \varepsilon}{\partial x_j}\right] + c_{\varepsilon 1}\frac{\varepsilon}{k} R_{ij}\frac{\partial U_i}{\partial x_j} - c_{\varepsilon 2}\frac{\varepsilon^2}{k} \tag{2.17}$$

The five closure coefficients, c_μ, $c_{\varepsilon 1}$, $c_{\varepsilon 2}$, σ_k, and σ_ε in Equations 2.14, 2.16, and 2.17 are empirical constants. Their values (Launder and Spalding, 1973) are given in Table 2.1.

Table 2.1 Numerical values of closure coefficients

Coefficient	c_μ	$c_{\varepsilon 1}$	$c_{\varepsilon 2}$	σ_k	σ_ε
Value	0.09	1.44	1.92	1.0	1.3

The κ-ε Model can be used to provide reasonably accurate statistics for a wide range of flow conditions (Rodi, 2000). It is considered one of the more accurate and commonly used models.

2.3 Sediment Transport

2.3.1 Initiation of Motion

A sediment particle submerged in an open channel flow has several forces acting upon it. These forces include the submerged weight, the lift force, the drag force, and a resistance force caused by interactions between sediment particles. These forces are illustrated in Figure 2.1 acting on a spherical, non-cohesive sediment particle of diameter, D. F_R is defined as the resistance force.

The initiation of movement is commonly assumed to occur when the mean shear stress applied by the fluid on the bed, τ_o, is equivalent to a critical shear stress, τ_{cr}. Assuming uniform flow, the bed shear stress, τ_o, is defined as

$$\tau_o = \gamma R_h S \tag{2.18}$$

where γ is the specific weight of water, R_h is the hydraulic radius, and S is the slope. Alternatively, the initiation of movement can be defined in terms of shear velocity, u_*, and a critical shear velocity, u_{*cr}. The shear velocity is defined as

$$u_* = \sqrt{\frac{\tau_o}{\rho}} \tag{2.19}$$

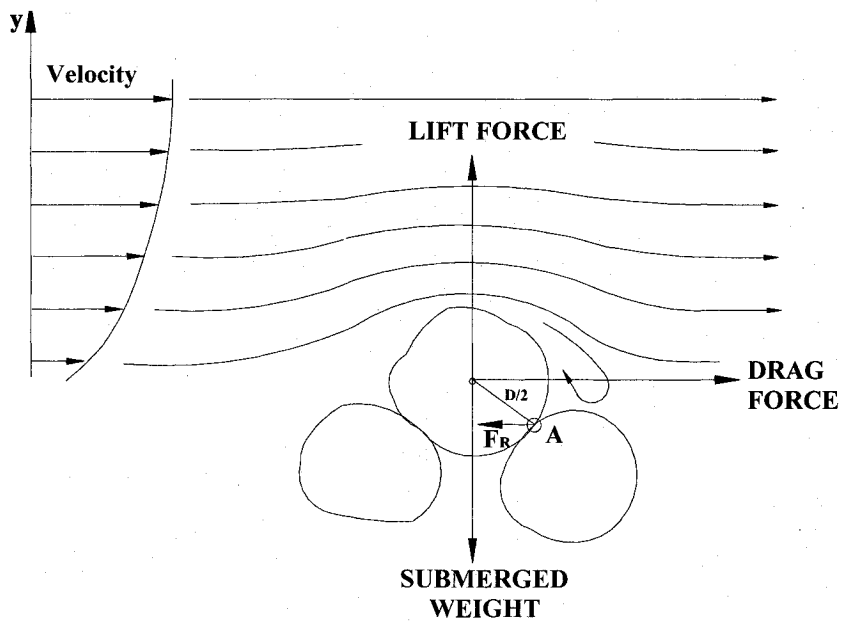

Figure 2.1 Forces acting on a submerged sediment particle in open channel flow

With respect to the forces shown in Figure 2.1, initiation of motion will occur when the mobilizing forces (lift force and drag force) exceed the stabilizing forces (submerged weight and resistance force). A definition of the critical shear stress, τ_{cr} (or the critical shear velocity, u_{*cr}), can be found by taking the sum of the moments about a downstream contact point (identified as "A" in Figure 2.1). The movement of a sediment particle depends on various factors such as the physical properties of the grain (i.e., size, shape, and density), and the structural arrangement of the particles (i.e., degree of packing, degree of grain exposure, imbrication, and armouring). Furthermore, Knighton (1998) points out that; "Sediment entrainment is a function not only of the shear stress acting on the bed but also of the intensity of turbulence above it which influences the magnitude and frequency of sweep and ejection events. Therefore, the definition of τ_{cr} (or u_{*cr}) will vary depending on the assumptions made and the influencing factors that are included.

Shields (1936) related a dimensionless critical shear stress to a particle Reynolds number, Re_* based on experimental data. The dimensionless critical shear stress, known as the Shields parameter or critical mobility parameter, is defined as

$$\textit{Shields / critical mobility parameter} = \frac{\tau_o}{(S_s - 1)\rho g D} = \frac{u_{*cr}^2}{(S_s - 1) g D} \tag{2.20}$$

The Reynolds number is given as

$$\mathrm{Re}_* = \frac{u_* D}{\nu} \tag{2.21}$$

The Shields entrainment function shown in Figure 2.2 defines the threshold of movement. Shields' experimental data are typically plotted as the Shields parameter versus the particle Reynolds number. In Figure 2 the Shields parameter is plotted versus the scaled particle parameter (Equation 2.23). Motion of sediment particles occurs above the plotted curve but not below. Further explanation of the Shields curve can be found in several textbooks including Simons and Sentürk (1992) and Knighton (1998).

2.3.2 Bedload Transport

The transport of bed material determines the form of a channel. The bedload can be defined as the coarse material moving on or near the bed of a channel, or bed material collected in or computed from samples collected in a bed load sampler. Bedload transport typically includes the material sliding and rolling along the bed and the saltation load (Raudkivi, 1998). This study focuses on bed load transport of non-cohesive sediments. The van Rijn model (van Rijn, 1984) is used to predict the bedload transport, which is a commonly used model for transport of sand.

The van Rijn method was derived by considering both the transport of particles moving by sliding/rolling and the particles moving by saltation. The model was calibrated using experimental data with grain sizes of the sediment particles ranging from 0.2 to 2 mm.

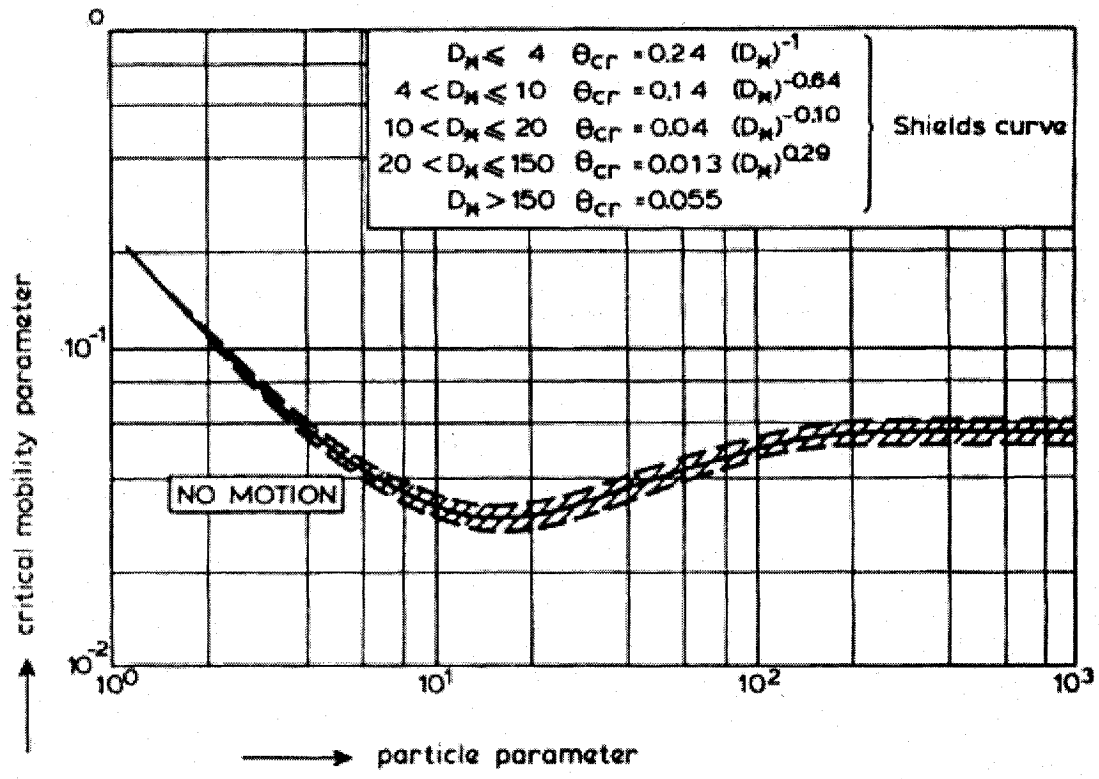

Figure 2.2 Initiation of motion according to Shields (from van Rijn, 1984)

The flow was assumed to be steady and uniform. The resulting van Rijn bedload transport equation is given by

$$q_b = 0.053 D_{50}^{1.5} [(S_s - 1)g]^{0.5} \frac{T^{2.1}}{D_*^{0.3}} \tag{2.22}$$

The van Rijn method was derived by considering both the transport of particles moving by sliding/rolling and the particles moving by saltation. The model was calibrated using experimental data with grain sizes of the sediment particles ranging from 0.2 to 2 mm. The flow was assumed to be steady and uniform. The resulting van Rijn bedload transport equation is given by

$$q_b = 0.053 D_{50}^{1.5} [(S_s - 1)g]^{0.5} \frac{T^{2.1}}{D_*^{0.3}} \tag{2.22}$$

where q_b is the volumetric transport in m^2/s, D_{50} is the median particle size by weight, S_s is the sediment specific gravity, and g is the gravitational acceleration. D_* and T are the scaled particle parameter and transport stage parameter, respectively, expressed as

$$D_* = D_{50} \left[\frac{(Ss - 1)g}{\nu^2} \right]^{\frac{1}{3}} \tag{2.23}$$

$$T = \frac{u_*^2 - u_{*cr}^2}{u_{*cr}^2} \tag{2.24}$$

where ν is the kinematic viscosity, u_* is the grain shear velocity given in Equation 2.19, and u_{*cr} is the critical shear velocity which can be found with the Shields diagram by using Equation 2.20.

Like most of the bedload transport models, the van Rijn method is considered a poor predictor of bedload (Gomez and Church, 1989 and Habersack and Laronne, 2002) because the formulae are derived from laboratory conditions that are not typical of natural channels. The flow is considered steady and uniform, the sediment supply into the channel is constant, and the experiments are conducted only for a specific range of sediment sizes. It must be noted that in natural channels the bed material transport is

random, spatially variable, and temporally variable. It is affected by many factors including variations in the grain size distribution throughout the reach, variations in the sediment supplied to the reach over time, turbulence, the presence of bed forms, and changes in flow rate.

2.4 Bank Stability

2.4.1 Secondary Currents

Secondary currents introduce a transverse shear that changes the shear distribution across a channel section and subsequently influences the sediment distribution. These currents exist in both straight channels and in channel bends (ASCE, 1998).

The velocity distribution in a cross-section of a straight channel is shown in Figure 2.3.

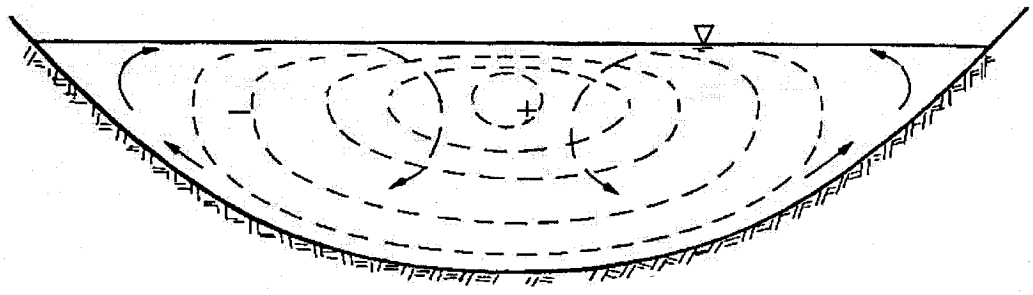

Figure 2.3 Diagrammatic illustration of equal velocity contour and superimposed spiral motion in open channel (from Raudkivi, 1998).

The circular dashed lines in Figure 2.3 represent equal velocity contours which show high velocities at the center of the channel and lower velocities near the bed and the banks.

This is the typical velocity distribution for a straight channel. The spiral action of the secondary currents is represented by the lines with the arrows which indicate the direction of circulation. Secondary currents in straight channels are classified as Prandtl's second kind, and are generated by anisotropy of cross-stream and vertical turbulent velocity fluctuations at channel boundaries, which result in momentum transfer imbalances (Nezu et al. 1993).

In channel bends the secondary currents are generated primarily by the channel curvature (Prandtl's first kind), because pressure imbalances are required to counter the centrifugal force (Daugherty et al. 1985). As a river flows through a bend, a circulation cell is created with flow directed towards the outer bank near the water surface and towards the inner bank near the bed (Figure 2.4). In combination with the primary downstream flow, the secondary currents create a helical flow through the channel (Figure 2.5). In plan, the primary and secondary currents interact to make a path of maximum velocity that begins on the inner bank near the beginning of the bend and crosses through the zone of maximum curvature to arrive at the opposite bank on the downstream side of the bend.

Knighton (1998) discusses other significant features of flow patterns through channel bends, including the superelevation of the water surface against the outer bank. In addition to this, a cell of opposite circulation develops near the outer bank (Markham and Thorne, 1992). Figure 2.4 shows this flow cell directed vertically up near the outer bank, whereas the secondary flow is typically directed vertically down towards the toe of the outside bank.

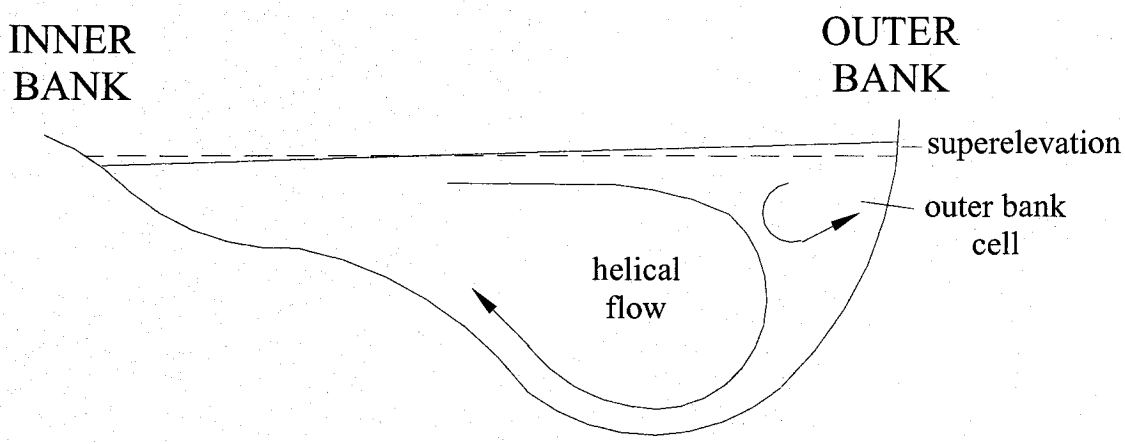

Figure 2.4 Secondary flows in a channel bend cross-section.

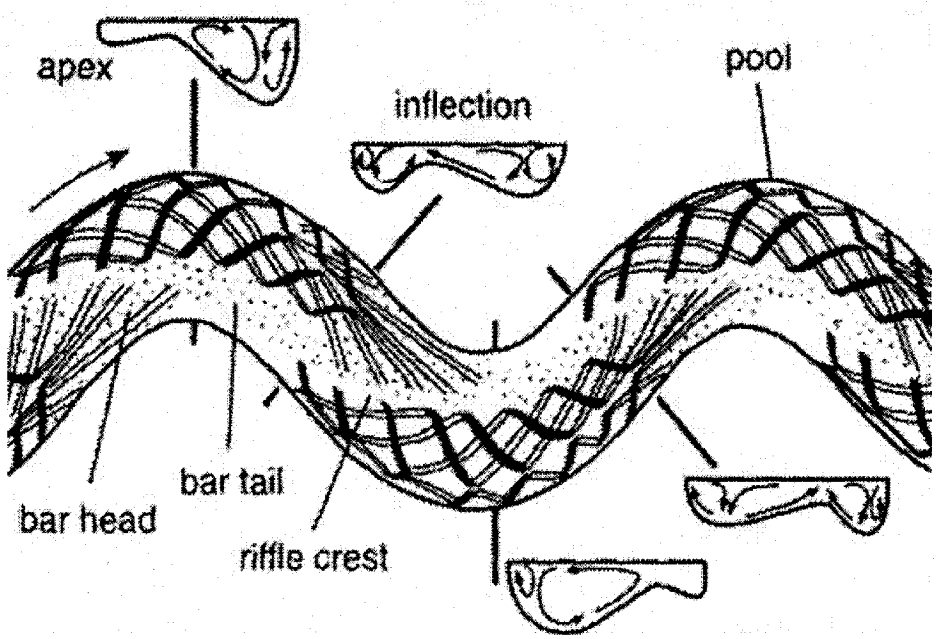

Figure 2.5 Helical flow through a series of meander bends (Knighton, 1998)

The secondary flow interacts with the primary flow to determine shear stress distribution, with maximum shear stress on the outer bank downstream of the bend apex (Dietrich 1987, and Figure 2.6). Consequently, there is increased erosion in the outer bank region. Conversely, there is a decrease in velocity and shear stress along the inside bank which encourages deposition of sediment and the formation of point bars.

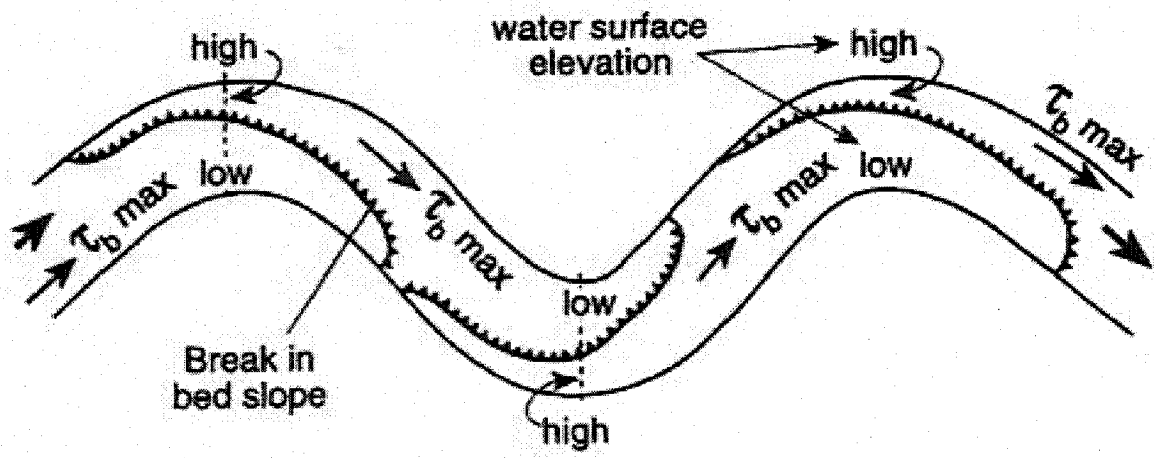

Figure 2.6 Boundary shear stress distribution through a series of meander bends (from Knighton, 1998)

2.4.2 Bank Erosion and Failure

The two important features that must be considered when examining the erosion of banks are the boundary shear stress distribution across the section and the critical shear stress of the banks. For non-cohesive sediments bank erosion will typically occur when the near-bank boundary shear stress exceeds the bank critical shear stress. The shear stress is closely connected to other fluvial variables including velocity, secondary currents, and turbulence. In general, the shear stress is influenced by the factors discussed in Section

2.3.1. However, the distribution of boundary shear stress across a channel bend section is complex due to the transverse shear produced by the secondary currents. Due to this complexity there is not a straightforward method or formula for calculating the shear stress distribution. Instead, the distribution must be estimated from empirical trends or from turbulence models (ASCE, 1998).

The critical shear stress of the banks is a function of the bank angle, and the bank material characteristics including grain size, shape, density, gradation, and structural arrangement of sediment particles. It must be noted that the erosion process of non-cohesive banks differs from that of cohesive banks.

Due to hydraulic action, the most common location of erosion on non-cohesive banks is at the toe of the bank. Figure 2.7 shows the distribution of critical bank shear stress and near-bank boundary shear stress. The critical shear stress of the bank is represented by τ_{bc} and the near-bank boundary shear stress is represented by τ_b. It can be seen that both the critical shear stress of the bank and the near-bank boundary stress increase with depth. Non-cohesive bank materials are frequently non-uniform, with sediment sizes increasing with depth (ASCE, 1998). As a result, the critical shear stress of the bank increases with depth as the sediment size increases. It can be seen in Figure 2.7 that as the depth decreases there is a point at which the near-bank boundary shear stress exceeds the critical shear stress of this bank. Erosion of the bank occurs below this point. If the bank materials are uniform the critical shear stress will remain constant with depth and the bank will be more susceptible to erosion at its toe. Due to this, non-cohesive banks

generally fail due to surficial bank erosion and sequential failures of small segments of bank material.

Cohesive materials behave differently than non-cohesive sediments due to a physical-chemical reaction between particles. Thus, for cohesive materials the "resistance to erosion depends more on the strength of the cohesive bonds between particles than the physical properties of the particles themselves" (Knighton, 1998). Furthermore, the critical shear stress of cohesive banks does not increase as much with depth as the near-bank boundary shear stress. Thus, erosion typically occurs at the toe of the bank, which leads to a progressive increase in the bank angle. As the bank angle increases the bank becomes unstable and fails. This usually occurs as a sudden failure of a large block of bank material. Furthermore, cohesive banks have low permeability. During conditions of rapid drawdown of the river stage, the banks are not able to drain quickly and become unstable. Once again this typically results in an abrupt failure of a large block of bank material.

The erosion of stratified banks that consist of both non-cohesive and cohesive sediments is more complex. Seepage of groundwater through the permeable layers removes the non-cohesive particles and causes the upper layers to drop and crack (Petersen, 1986). This process compromises the stability of the bank by creating a shear failure surface.

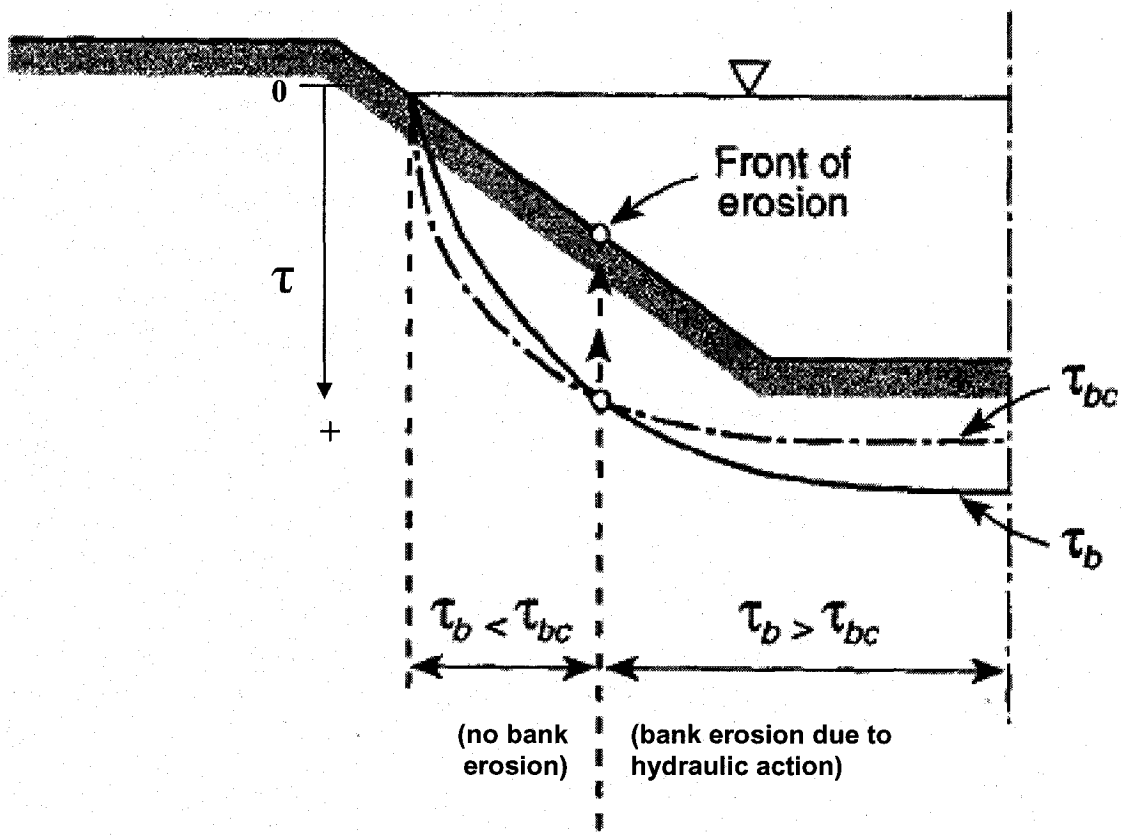

Figure 2.7 Critical bank shear stress and near-bank boundary shear stress distributions for a non-cohesive bank (adapted from Kovacs and Parker, 1994)

2.5 Bank Stabilization

Traditional methods of streambank stabilization typically utilize revetments, constructed of riprap or gabions, or emergent structures such as groynes and dykes. More recently, the need for innovative and cost effective methods has led to the development of low-profile, flow deflection structures such as bendway weirs and barbs. In addition, stabilization techniques have been incorporating bioengineering technology for the protection of streambanks. Streambanks are generally stabilized to prevent the loss of

land due to erosion. In cases where property and infrastructure are not threatened streambanks may be stabilized in order to improve the alignment of the stream or to improve navigation. Successful stabilization works should not force a river into unnatural conditions. Instead, "...stabilization works must control the river by guiding it along a natural alignment with channel cross-sections that accommodate the river's water and sediment regime" (Petersen, 1986). Otherwise, erosion problems may be translated downstream. River training structures should be designed to withstand the design flow of the channel. In addition, the effect of structures on the channel should be evaluated and understood.

2.5.1 Revetments

Revetments are non-erodible structures constructed on sloping, eroding soil banks. Traditional revetment material includes concrete blocks, rock rip-rap, and gabion baskets. In recent years bioengineering techniques have been incorporated into traditional methods (e.g., joint planting). The bioengineering techniques utilize live vegetation and woody debris, thus adding diversity to, and enhancing a stream's ecosystem.

Important factors to consider in the design of revetments include the following:

- Design flood;
- Bank slope; and
- Toe protection.

Determination of the design flood is necessary to establish the required distance up the bank that the revetment should be placed. Petersen (1986) recommends that the bank should be graded to a slope of 1V:2H to 1V: 4H. USDA (1996) suggests that typical engineering slopes are approximately 1V: 3H. Essentially the bank slope must be less than the critical side slope. Failure of revetment structures has typically been due to a lack of protection at the toe of the bank. Therefore, all forms of revetment structures must include protection at the toe of the bank, down to an elevation below the expected depth of scour. In addition, erosion control fabric can be placed where extra protection is required.

One of the most popular materials in the United States in the 1980s for revetments was mattresses made from pre-fabricated **concrete blocks**. In 1984, approximately 1350 km of this type of revetment had been placed on the Lower Mississippi River (Petersen, 1986). A revetment with a concrete mattress is presented in Figure 2.8. This type of revetment is flexible and adjusts to irregularities in the bed and bank. However, there are several disadvantages associated with using concrete blocks. The equipment required and the installation of these mattresses is expensive. In addition, the spaces between the concrete blocks allow for erosion of the bed material under the mattress. With respect to the stream habitat, the placement of concrete blocks on the streambank and stream bed destroys the diversity of the stream's ecosystem.

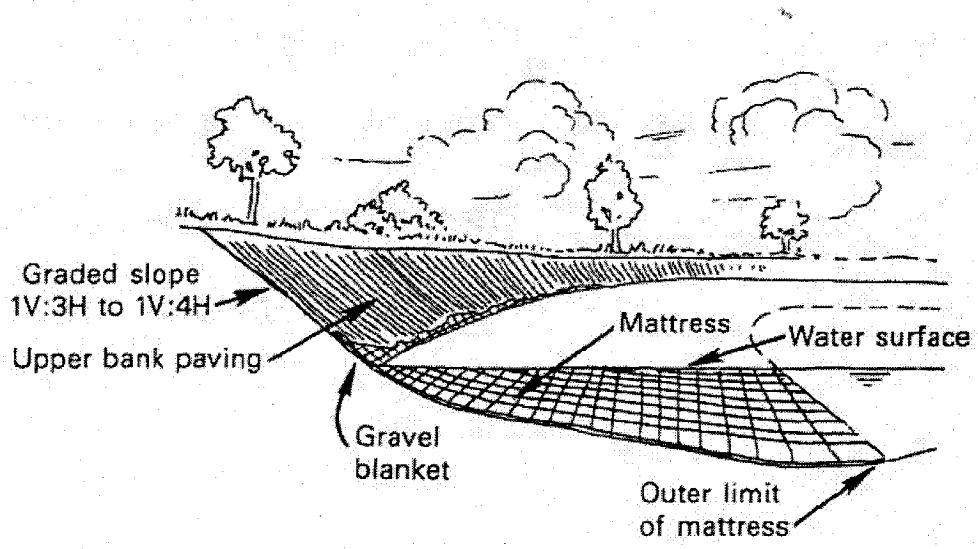

Figure 2.8 Concrete mattress revetment (Petersen, 1986)

Alternatively, **rock rip-rap** can provide effective streambank protection when designed and placed properly. Rock rip-rap has several advantages including (from Przedwojski and Blazejewski, 1995 and USDA, 1996):

- Relatively easy to place;
- Construction is quick and economical;
- Structural flexibility;
- Self-adjusts to eroding foundations to some extent;
- Low-maintenance;
- Durable;
- Has a long life;
- Natural appearance; and
- May be designed for high velocity/shear stress conditions.

A rock rip-rap revetment is shown in Figure 2.9. From this figure it can be seen that large rocks have been placed on a graded slope. Generally, well graded, angular rocks provide the best stability and protection. The thickness of the rip-rap layer will also influence the stability. The rip-rap size is determined based on the critical bank shear stress. Four methods for designing the rip-rap size are summarized in USDA (1996). They include the Isbash Curve, Far West States-Lane, US Army Corps of Engineers Method, and the Federal Highway Administration method. Other methods can be found in Simons and Senturk (1992). At the toe of the bank the rip-rap is placed down to an elevation below the expected depth of scour. In addition, the largest stones are placed at this location. A transition zone, designed as a bedding, filter, or geotextile, can be included to distribute the weight of the rip-rap to the underlying soil, and prevent transport of fine material through voids in the rip-rap. A transition zone can be seen in Figure 2.9.

It should also be noted from Figure 2.9 that vegetation or bioengineering methods can be applied to the slope above the rip-rap for additional stability. Furthermore, vegetation can be used to increase the stability of the rip-rap itself. **Joint planting** involves inserting live stakes into voids in the rip-rap or tamping the stakes into place while the rip-rap is being placed. This combination of traditional and bioengineering bank stability techniques, shown in Figure 2.10, has several benefits including (USDA, 1996): roots improve drainage as they remove moisture from the soil; root systems reinforce the soil; and vegetation dissipates some of the energy along the streambank.

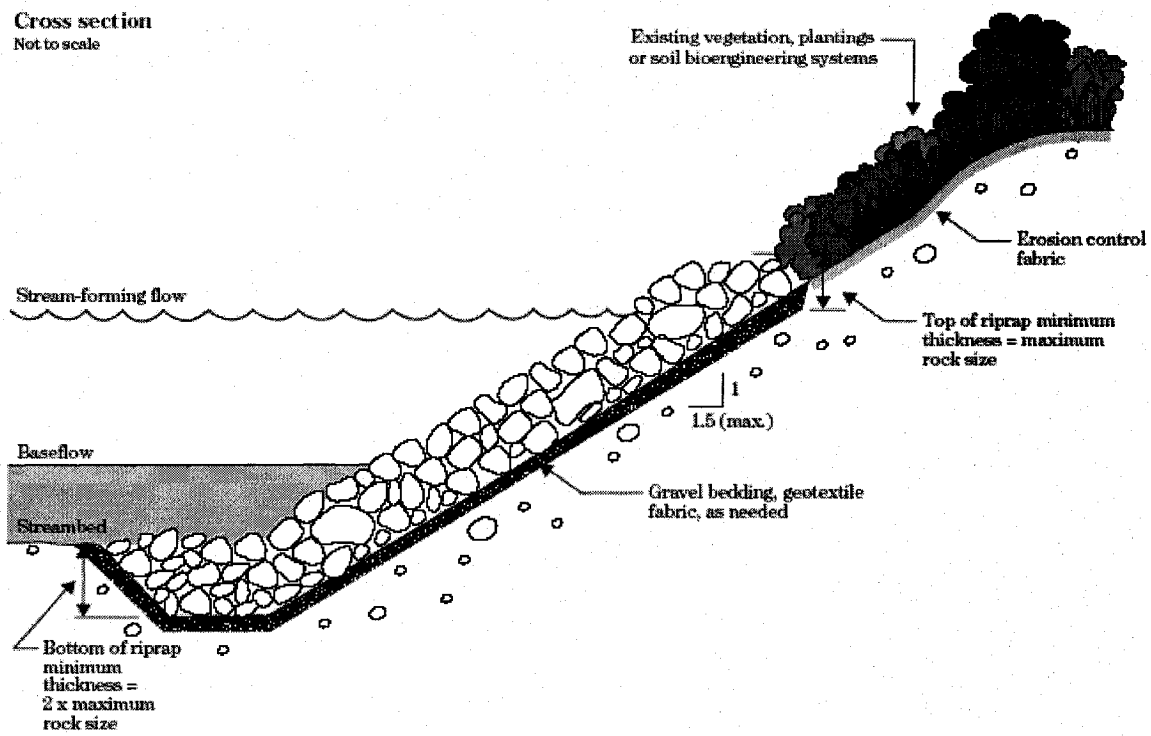

Figure 2.9 Rock rip-rap revetment (USDA, 1996)

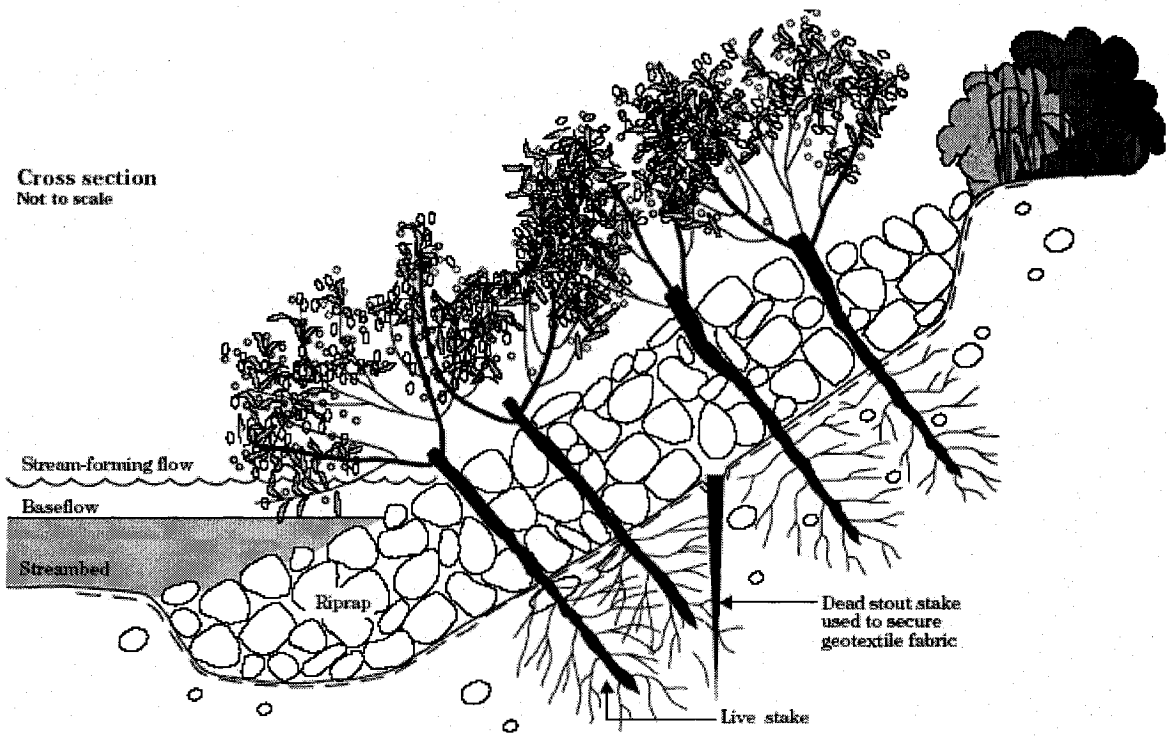

Figure 2.10 Vegetated rip-rap revetment (USDA, 1996)

Gabions are rectangular wire baskets that are filled with relatively small rock rip-rap. They are an effective alternative to a rock rip-rap revetment in locations where large diameter rip-rap is not available locally. In addition, gabions can be used to provide structural stability to slopes steeper than 1V: 1.5H. However, the wire mesh baskets are prone to tear if they are exposed to ice or debris. Similar to the rock rip-rap revetment, the addition of live stakes to a gabion revetment can increase its stability. A vegetated rock gabion revetment is presented in Figure 2.11.

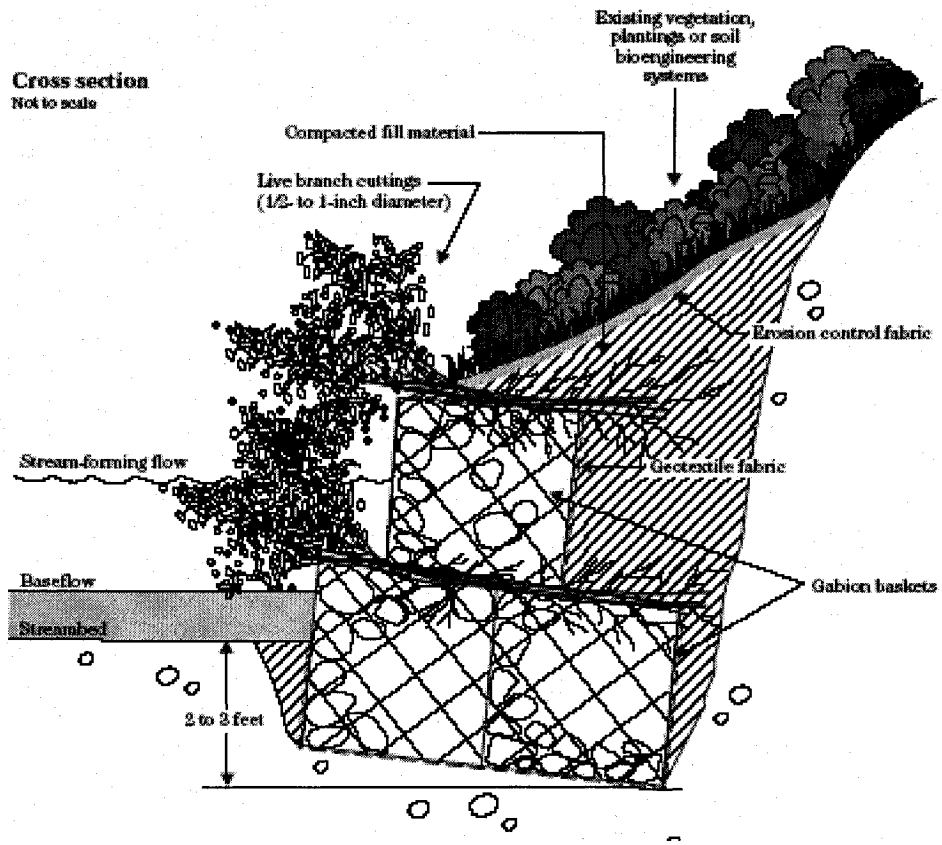

Figure 2.11 Vegetated rock gabion revetment (USDA, 1996)

2.5.2 Flow Deflection Structures

Flow deflection structures include groynes, dikes, jetties, bendway weirs, and barbs. All of these flow deflectors can be defined as structures that extend from a river bank, either at an angle or perpendicular to the flow, and prevent erosion by deflecting flow away from the bank. Flow deflection structures may be constructed from a variety of materials including stone, gravel, rock, earth, or logs. The material chosen is generally dependent on what is available locally. These structures are often installed in series along an eroding streambank. Traditionally, flow deflection structures have been built such that the structure emerges out of the water and is overtopped only at the highest flows. More recently, there has been interest in low-profile submerged flow deflectors, such as bendway weirs and barbs, because they require less material to construct and are less obtrusive.

2.5.2.1 Bendway Weirs

Bendway weirs were originally developed for use in large rivers. The concept of this structure was first conceived in 1988 for use in the Mississippi River (USACOE, 1998). A bendway weir can be defined as a submerged rock structure that extends into the flow away from the bank. They are typically placed in series along the outside bank of a channel bend. The length of the structures ranges from approximately 122 m to 488 m and they are usually angled 20^{o} to 30^{o} upstream into the flow.

A bendway weir functions by redirecting the water flowing over the weir away from the outside bank at an angle perpendicular to the weir. In addition, the bendway weir disrupts

the secondary currents and shear stress distribution close to the outer bank. As a result, it has been observed that the flow patterns become more parallel with the banks and the location of the thalweg shifts away from the outside bank (USACOE, 1998).

Advantages of bendway weirs include the following (Derrick, 1997):

- Flow can be redirected and predicted;
- Weirs work best under high-flow, high-energy conditions;
- Flow is considered controlled within the weir field;
- Weirs can be retrofitted after project completion to improve the hydraulic performance of a project; and
- Weir costs are competitive or lower than traditional stabilization methods.

Due to the success of these structures in large rivers, the design has been modified for use on smaller streams. Small bendway weirs and barbs are smaller variations of the large river bendway weir.

2.5.2.2 Barbs

Similar to bendway weirs, barbs are typically anchored, in series, to the outside bank in stream bends and extend in an upstream direction from the bank into the flow. A unique feature of barbs is that they have trapezoidal cross-sections and that the top of the barb gently slopes downward as it extends away from the bank (USDA, 2005). A series of barbs is designed to redirect flow away from the outer stream bank and disrupt the

velocity gradient and shear stress distribution close to the outer bank. As a result of this disruption the location of the thalweg shifts away from the outside bank. Furthermore, a zone of low velocity and low Froude number is generated upstream of the barb structure along the outer bank. Thus a series of barbs, installed correctly, protects the outer bank from erosion and promotes sediment deposition. In addition to this, it has been observed that vortices are generated at the tips of the barbs creating local scour holes that can enhance aquatic habitat (Shields et al.1998).

Barbs consist of a key and a weir section. These two sections are defined in Figures 2.12 and 2.13. The key section is set back into the bank material and acts as an anchor. The weir section extends in an upstream direction away from the bank. Note that the bank-line is defined by the bankfull discharge.

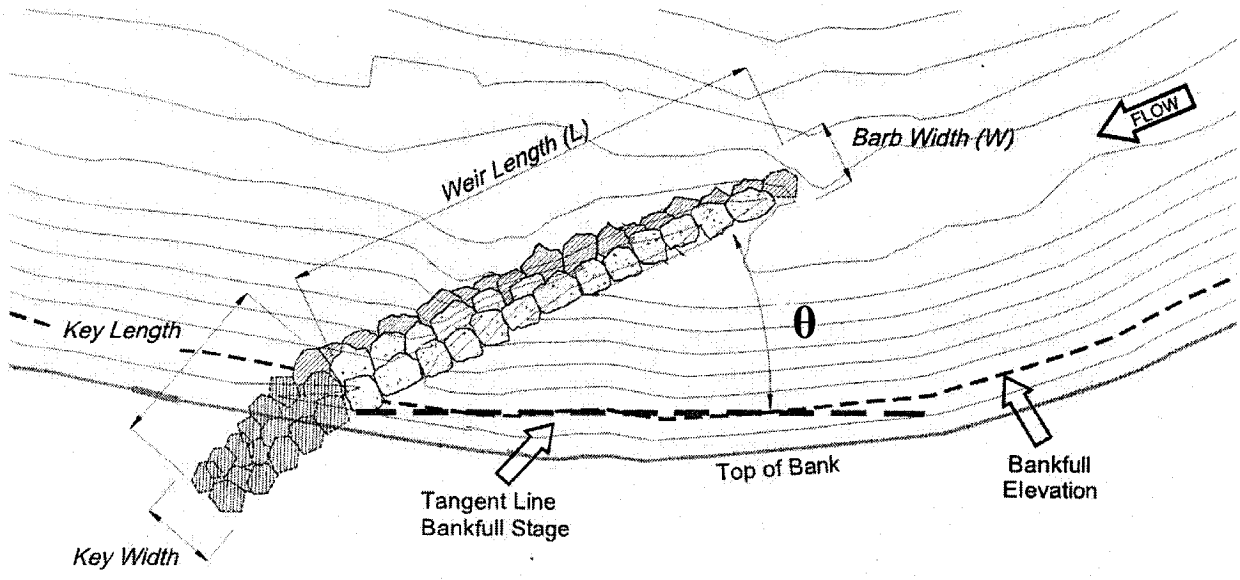

Figure 2.12 Plan view of barb (USDA, 2005)

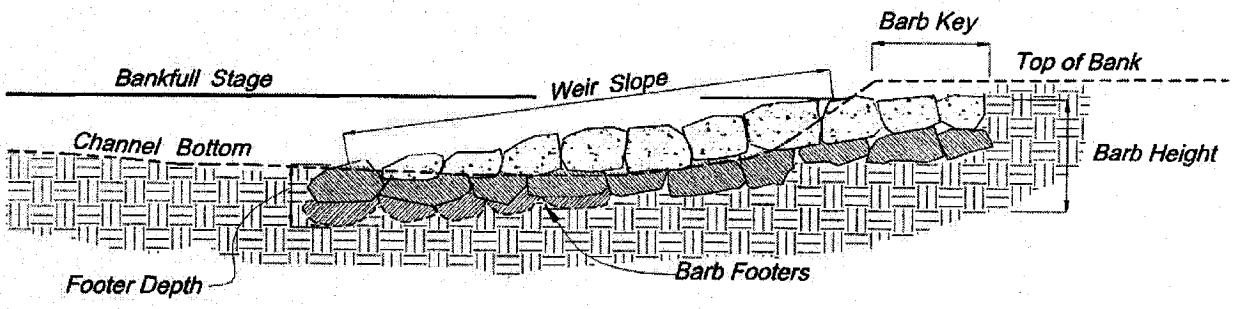

Figure 2.13 Profile view of barb (USDA, 2005)

Figure 2.14 illustrates how a series of barbs influences the direction of the flow attacking the outer bank of a channel bend. It can be seen that as the flow passes over the weir section of a barb, it is redirected downstream at a right angle to the length of the weir section. This redirection of flow helps to protect the outer bank against erosion. In addition, this process counteracts the secondary currents formed due to channel curvature. Therefore, unlike other traditional methods of bank protection, barbs are a proactive type of bank protection that attack the erosion mechanism.

Barbs have been used extensively in the United States since the late 1980s. However, limited documentation exists of barb design criteria and performance. In 2005 an updated document was released by the USDA, which included review of the field performance of new projects and of relevant literature pertaining to barbs (USDA, 2005). The design guidelines presented in Table 2.2 are based on this document.

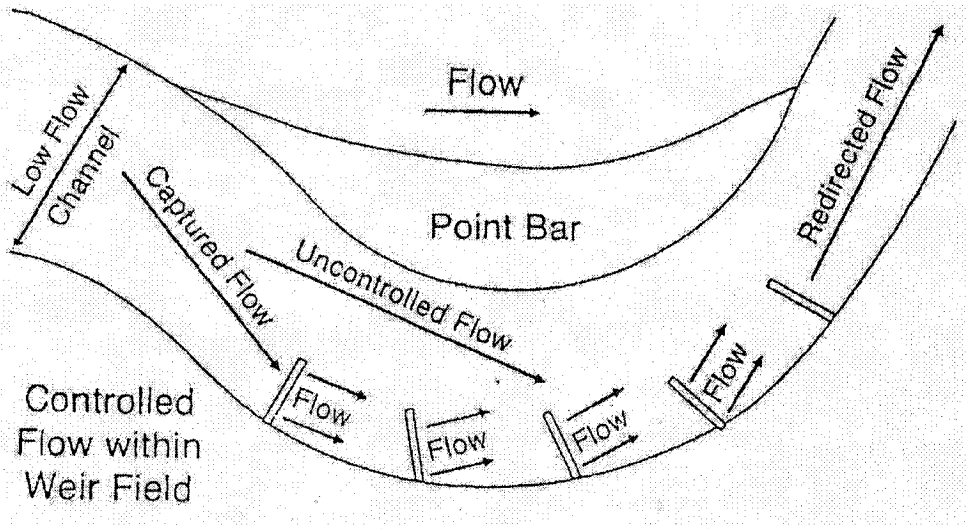

Figure 2.14 Direction of flow through a channel bend containing barbs (from Derrick, 1997a)

Table 2.2 General design guidelines (adapted from USDA, 2005)

Parameter	**Design Guidelines**
Weir length, L	-each barb should extend from the bank-line to the proposed thalweg location -length should not exceed 1/3 of the channel cross-section
Key length	-extends into the bank 1/4 to 1/3 the weir length
Barb width, W	-typically narrow at the weir tip ($W = d_{100}$) -progressively widens towards the bank -width ranges from one to three times the d_{100}
Key width	-equal to the barb width at the bank
Barb alignment angle, θ	-optimum angle 20° to 30°
Barb height and weir slope	-barb height at the bank is set at bankfull stage -the barb slopes down between 5% and 8% with distance away from the bank
Key height	-the key height is equal to the barb height at the bank.
Barb footers	-Typically placed to a depth of D_{100} or 2.5 times the exposed height of the rock above the streambed (whichever is greater)

Barbs are typically constructed of rocks. Using a standard rip-rap sizing criteria for turbulent flow, the following equations may be used to calculate the appropriate material size (USDA, 2001).

$$D_{50\text{-barb}} = 2 \times D_{50\text{-riprap}} \quad (3.1)$$

$$D_{100\text{-barb}} = 2 \times D_{50\text{-barb}} \quad (3.2)$$

$$D_{minimum} = 0.75 \times D_{50\text{-riprap}} \quad (3.3)$$

However, the USDA (2005) recommends that a physics-based threshold stability analysis be performed to determine the minimum size of the weir and footer rock.

There are contradicting guidelines for the location of barbs in a channel. The most recent guideline (USDA, 2005) recommends placing the last barb in a series in the downstream quarter of a channel bend or near the downstream end of bank erosion. The number of barbs placed in series is dependent on the barb spacing, the length of the eroding bend, channel geometry, amount of bedload, and the desired result (USDA, 2001). The spacing of the barbs is typically determined using the methodology illustrated in Figure 2.15.

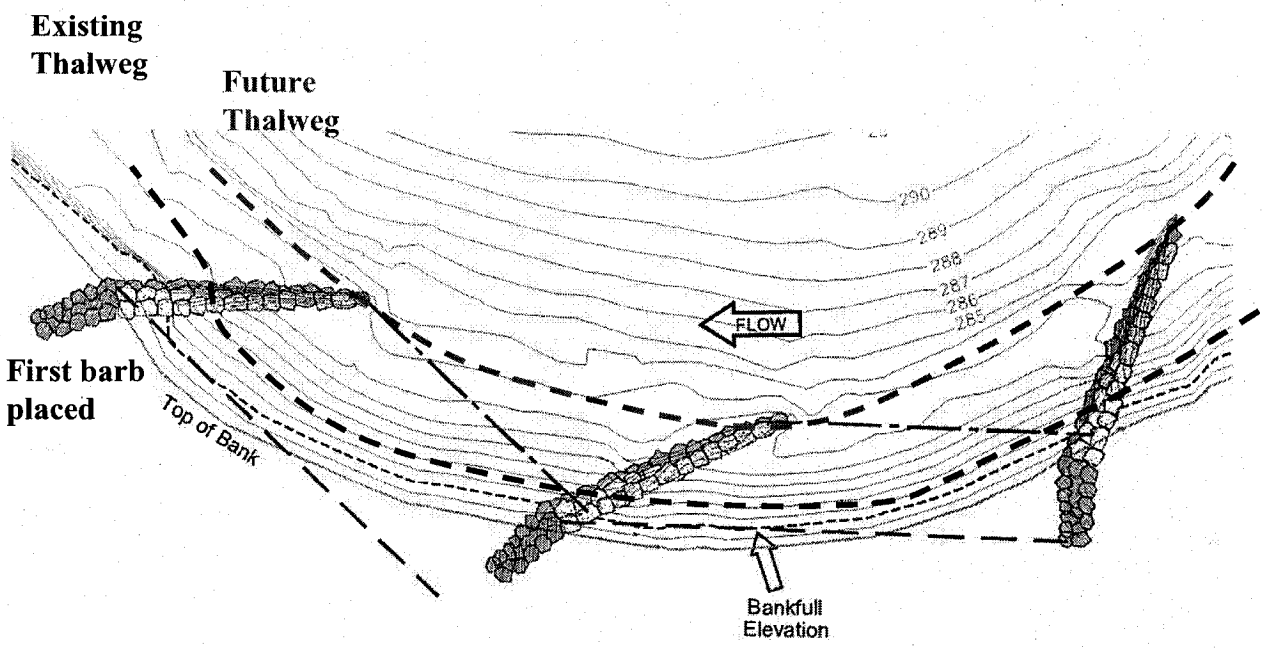

Figure 2.15 Barb spacing methodology (USDA, 2005)

Once a barb has been placed in the downstream quarter of the channel bend (or near the downstream end of bank erosion), draw a tangent to the bank-line. At the tip of the barb draw a line parallel to the bank tangent line and extend it upstream until it intersects the bank-line.

This is the approximate location of the next barb. Repeat this process until the locations of all of the barbs are established. In addition, it can be seen in Figure 2.15 how, with the addition of barbs, the location of the thalweg shifts away from the outer bank and towards the tips of the weir section.

Installed correctly, a series of barbs can effectively protect the outer bank of channel bends from erosion and promote sediment deposition. The USDA (2001) suggests that the performance of barbs can be improved when used in conjunction with bioengineering methods. The addition of vegetation to barbs and the surrounding streambank provides additional stability and enhances wildlife and aquatic habitat. Another technique is incorporating large woody debris into the rock barbs. This arrangement further enhances the aquatic habitat by providing cover and food.

2.6 Previous Related Work

Many field installations of these structures are performed using good judgment and experience rather than following specific criteria. In addition, there is limited documentation of the design criteria that have been used for the field installation of barbs and for the long-term performance of these structures. Recently there has been an effort to provide recommendations and guidelines for the design of barbs (e.g., USDA, 2005), yet it must be noted that these are only suggestions.

There has been a considerable amount of studies performed on groyne structures. However, most of these studies have been limited to the examination of a single, emergent groyne perpendicular to the stream bank in a straight channel (e.g., Tingsanchali and Maherswaran, 1990. Ouillon and Dartus, 1997. Nagata et al., 2005). There have been several studies on groyne fields (i.e., a series of barbs). However, they typically investigate only groynes perpendicular to the flow field. Uijttewaal et al. (2001) and Sukhodolov et al. (2004) examined flow patterns in a series of emergent

perpendicular groynes in a straight channel. Sukhodolov et al. (2002) described changes in bed morphology due to the installation of a series of groynes in the field.

Scour around a single submerged spur dike in a straight channel has recently been studied for orientations perpendicular to the bank (Kuhnle et al., 1999) and angled upstream (Kuhnle et al., 2002). The laboratory experiments conducted by Kuhnle et al. (2002) in a straight flume examined the effect of three different alignment angles on the volume of scour. The three alignment angles tested were 45, 90, and 135°. Therefore, the effects of a submerged spur dike angled: (i) upstream into the flow; (ii) perpendicular to the bank; and then downstream into the flow were studied. The focus of this study was to determine the angle that enhanced the potential for aquatic habitat and minimized near-bank erosion. Based on their experimental results, Kuhnle et al. (2002) found that the spur dike angled downstream ($\theta = 135^{o}$) had the greatest amount of near-bank erosion. The 90° spur dike caused the least amount of near-bank erosion. However, the spur dike angled upstream ($\theta = 45^{o}$) created the largest scour hole at its tip, which is ideal for improving in-stream habitat. Kuhnle et al. (2002) concluded that, as long as the far-bank was not threatened, a single spur dike angled upstream ($\theta = 45^{o}$) in a straight channel was the best design because it minimized near-bank erosion and maximized the volume of scour.

While these studies have provided useful data most natural channels are not straight and typically bank protection is required along the outer bank of channel bends. Przedwojski (1995) investigated changes in bed morphology due to the installation of a series of groynes along the outer bank of a river bend. This field study examined only groynes that

were slightly angled upstream. A laboratory study by Matsuura and Townsend (2004) examined the scour patterns of groyne fields in 90 and 135° narrow channel bends with varied height, spacing and alignment angles of submerged groynes. The associated flow field was not analyzed. Most recently, Jia et al. (2005) used a three-dimensional numerical model to simulate the flow field around a single submerged weir in a channel bend. Results were validated using experimental velocity data, measured with an acoustic Doppler velocimeter device. The velocity was adjusted to ensure that sediment transport did not occur through the channel. This study examined only one submerged groyne, located at the channel bend apex, with an alignment angle of 20°.

There remains a need for further studies to identify the optimum groyne dimensions, spacing, and orientations in the bend flow field for different bend geometries and hydraulic conditions. Most importantly, an understanding of the interaction between the complex flow field and the sediment transport through the channel bend is required in order to improve design guidelines and to predict the long-term performance of these structures.

3.0 Methodology

A three-dimensional numerical model was used to simulate the turbulent flow field and associated scour and deposition of the bed sediments due to a series of barbs in both a 90 and a 135° channel bend. The numerical model was calibrated to the scour measurement data obtained from the physical laboratory experiments described in Matsuura and Townsend (2004) and Matsuura (2004).

3.1 Experimental Data

The scour measurement data that are presented in Matsuura and Townsend (2004) and Matsuura (2004) were collected in the Engineering Hydraulics Laboratory at the University of Ottawa. The channel that was used for the testing is shown in Figure 3.1.

From this figure it can be seen that the channel was comprised of three rectangular-shaped sections: the entrance section was 0.460 m wide by 0.254 m deep by 9.75 m long; the exit section was 0.460 m by 0.406 m by 2.44 m long; and there were two exchangeable bend sections 0.460 m wide by 0.406 m deep which were installed separately. The two bend angles used were 90 and 135°. The exit sections and the bend section were 0.152 m deeper than the rest of the channel. This allowed for a 0.152 meter deep sand bed to be placed in the bend and exit sections.

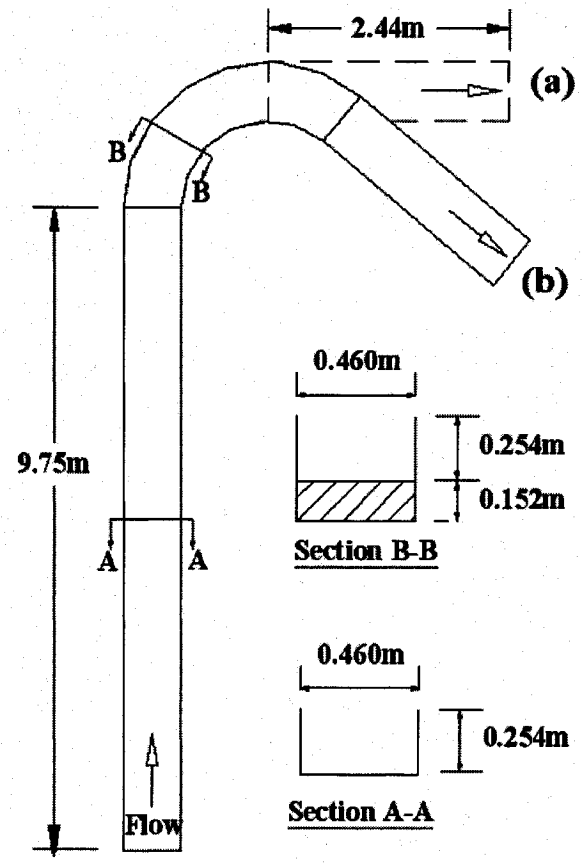

Figure 3.1 Experimental channel showing: (a) 90° bend arrangement; and (b) 135° bend arrangement (adapted from Matsuura, 2004)

3.1.1 Experimental Procedures

The experimental procedures were largely based on design recommendations suggested by USDA (1999) which has since been updated to USDA (2005). The parameters that were varied for each experiment were channel bend angle, barb alignment, and the location of the barbs. Scour tests were performed separately with the 90° channel bend section and the 135° channel bend section. For each channel bend section there were three different barb alignment angles ($\theta = 20^{\circ}, 30^{\circ}, 40^{\circ}$) assessed, two different barb

height to flow depth ratios (h/y_o = 0.5 and 0.375), and a constant channel width (W = 0.460 m). For the 90° channel bend four different group-types (A, B, C, and D) were evaluated. Two different group-types were examined in the 135° channel bend. The group-types were defined by the location of the first barb in the group relative to the bend entrance, L. This location ranged from 0.81 m < L < 1.41 m. The barb locations divided by channel width for the 90° channel and the 135° channel are presented in Tables 3.1 and 3.2, respectively. Barb location is defined, in meters, as the distance along the outside bank, from the channel bend entrance, to the location of the barb along the outer channel bank. Channel width was 0.460 m.

Table 3.1 Barb locations in 90° channel bend (adapted from Matsuura, 2004)

Alignment angle, θ	Group-type	Barb location / Channel width			
		Barb 1	Barb 2	Barb 3	Barb 4
20	A	2.67	3.56	4.82	N/A
	B	3.08	4.01	4.98	N/A
	C	1.78	3.14	4.40	N/A
	D	1.33	2.31	3.27	4.40
30	A	2.67	3.56	4.82	N/A
	B	3.08	4.08	5.07	N/A
	C	1.78	2.75	3.61	4.57
	D	1.33	2.17	3.08	4.08
40	A	2.67	3.39	4.22	N/A
	B	3.08	3.87	4.68	N/A
	C	1.78	2.58	3.36	4.23
	D	1.33	2.11	2.94	3.78

Table 3.2 Barb locations in 135° channel bend (adapted from Matsuura, 2004)

Alignment angle, θ	Group-type	Barb location / Channel width					
		Barb 1	Barb 2	Barb 3	Barb 4	Barb 5	Barb 6
20	B	3.08	3.98	4.82	5.72	7.20	N/A
	C	1.78	3.14	4.06	4.95	5.87	N/A
30	B	3.08	4.01	4.82	5.57	6.87	N/A
	C	1.78	2.75	3.61	4.41	5.29	6.29
40	B	3.08	3.87	4.62	5.24	6.20	N/A
	C	1.78	2.58	3.36	4.18	5.07	5.98

In order to prevent ripple formation, armouring, and suspended sediment transport, the sand placed in the 0.152 meter deep bend and exit sections had a median diameter of 0.85 mm with a geometric standard deviation of approximately 1.3. The channel slope was set at 0.001. Throughout the experiments, a constant discharge of 0.0132 m^3/s, measured with a 90° v-notch weir, was maintained with an average velocity of 0.28 m/s, and an average flow depth of 0.102 m.

Initial test runs were conducted in both the 90 and 135° channels without any barbs to determine the maximum scour depth, scour profile, thalweg location, and bank scour. It was observed that equilibrium was established at approximately 26 h. Channel bed surface elevations were measured to an accuracy of ± 0.8 mm with a laser meter. The bed elevations were recorded at seventeen locations across the channel, on cross-sections spaced at 10 degree intervals through the bend. The cross-sections were spaced at 0.150 meter intervals downstream of the bend exit. As a result, a set of reference bed elevations was established for the 90 and 135° channels. All subsequent test runs were compared to these reference data sets. The reference bed elevation contour maps for the 90 and 135° channels are presented in Figure 3.2 and Figure 3.3 respectively.

Test runs were performed for each of the barb group-types listed in Tables 3.2 and 3.3. These test runs lasted approximately 5 h each. In order to complete the laboratory study within a reasonable amount of time, it was not possible to run all experiments for the full 26 h. However, because the equilibrium condition is approached asymptotically, maximum scour values at approximately 5 h were found to be approximately 87% of the equilibrium reference tests. Also, it was observed that highly representative stable scour depths with barbs in place were achieved at approximately 5 h. It was decided, based on these results, that all model barb tests would be run for 5 h.

3.1.2 Experimental Results and Conclusions

Comparisons of the experimental results were performed based on the percent reduction in local scouring and the movement of the thalweg away from the outside channel bank. The percent reduction was calculated using Equation 3.1.

$$Percent\ reduction = \frac{\sum y_s - \sum y_s'}{\sum y_s} \times 100\% \qquad (3.1)$$

The scour depth measured without barbs in the channel is defined as y_s, and the scour depth with barbs in the channel is given as y_s'. Scour depths were measured at 0.0254 m from the outside wall of the channel within the region of maximum scour observed during the initial test runs. (The regions of maximum scour in the 90 and 135° channels were observed to commence 1.22 m to 1.41 m from the channel bend entrance).

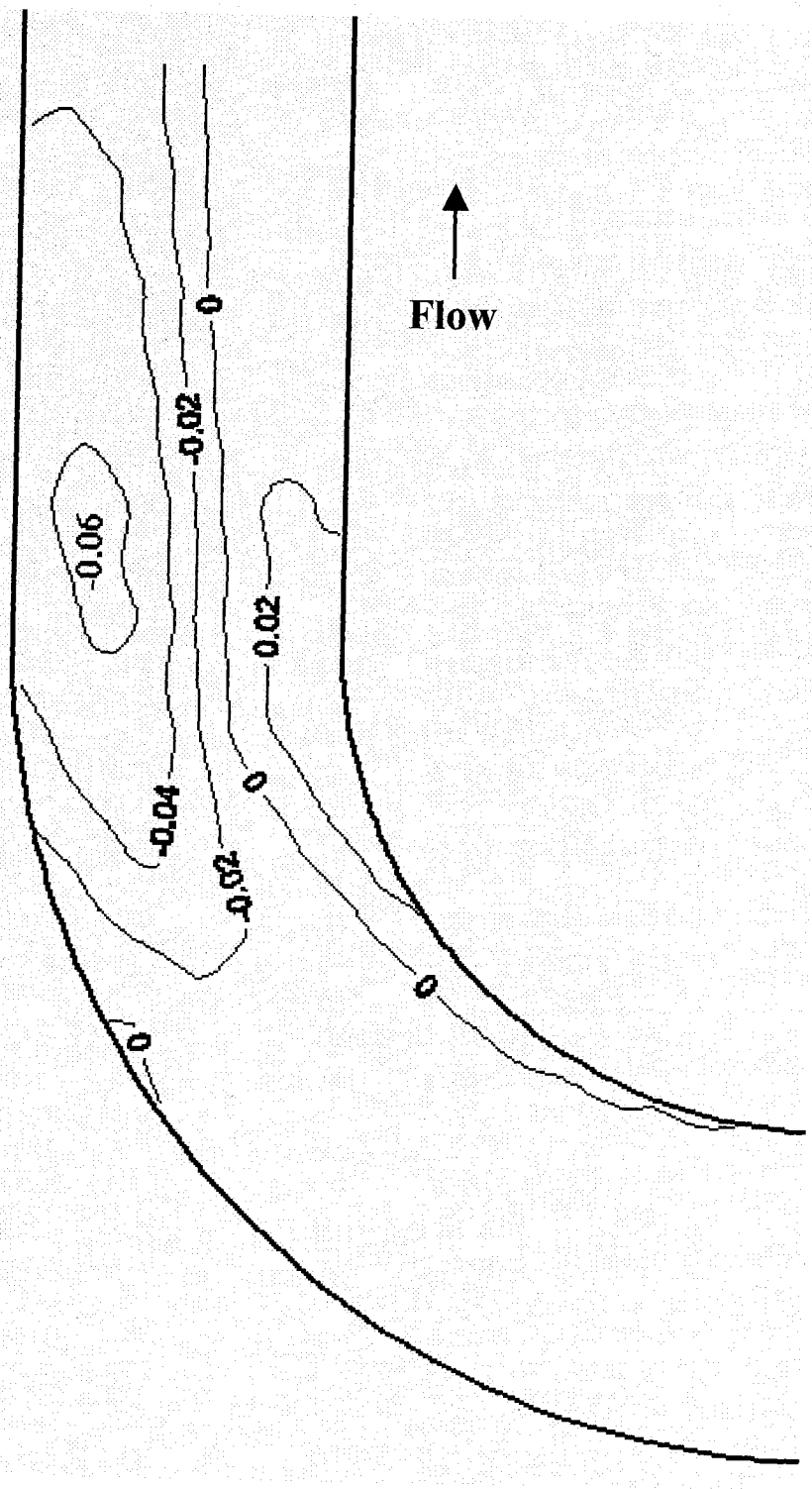

Figure 3.2 Measured reference bed elevation contour map for 90° bend (m)

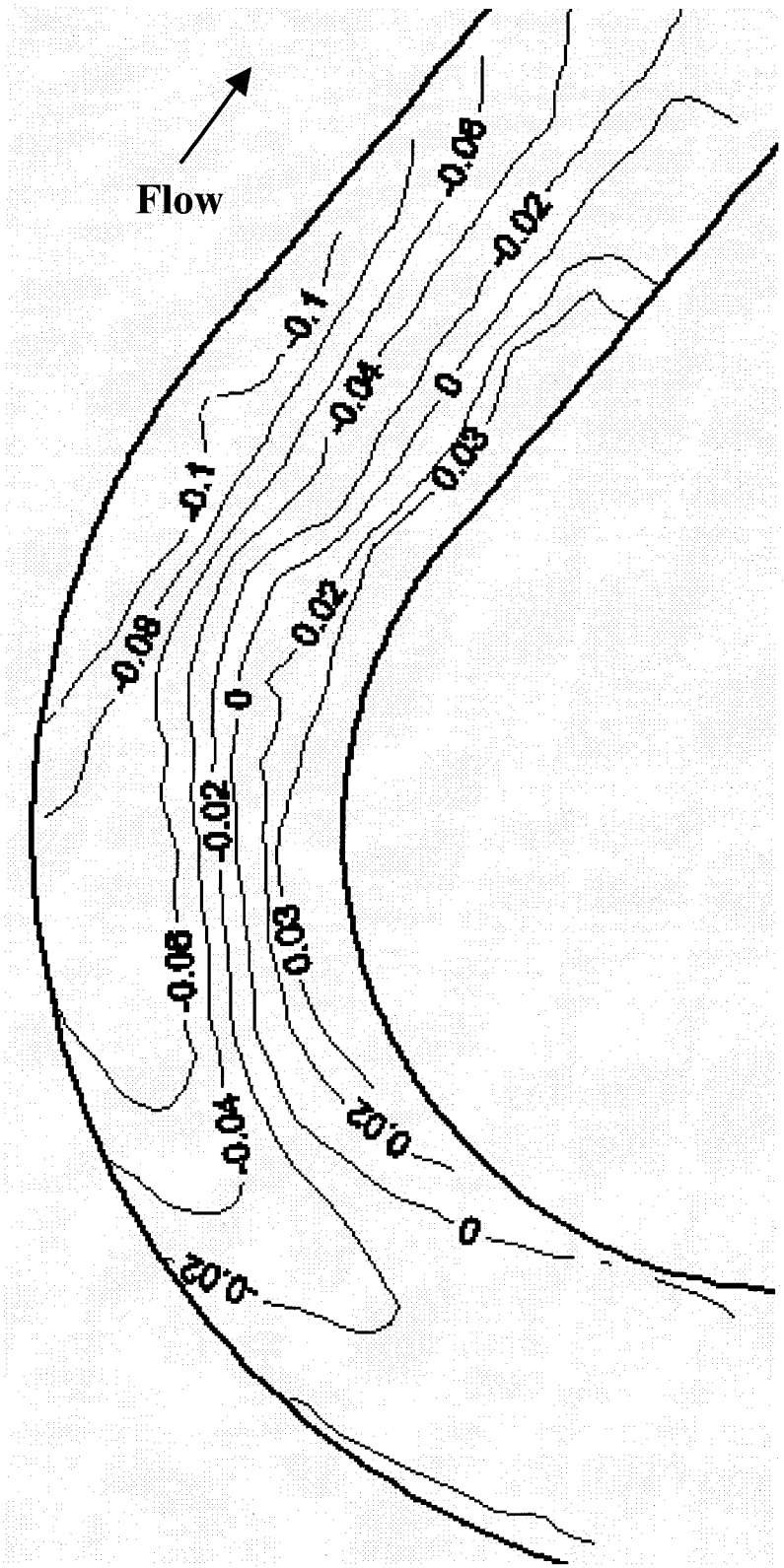

Figure 3.3 Measured reference bed elevation contour map for 135° bend (m)

Analysis of the experimental data suggested the following (Matsuura and Townsend, 2004):

- Locating the first barb upstream of the section affected by erosion does not appear to improve the barb group performance;
- Locating the last barb immediately downstream of the bend exit significantly reduces the percent local scouring;
- Scouring of the channel bed in the vicinity of the barbs is less severe if the weir-section height of the structures is kept small relative to the channel-forming flow depth. ($0.33 \leq h/y_o \leq 0.5$). If this is satisfied then barb performance largely depends on barb alignment and first and last barb locations;
- A 30^o barb alignment angle is the preferred alignment; and
- Barb group type B provided the best overall protection.

Further details of the experimental methods and data are available in Matsuura (2004) and Matsuura and Townsend (2004).

3.2 Numerical Model

The three-dimensional numerical model used for this study was Sediment Simulation in Intakes with Multiblock option (SSIIM), Version 1.1. This model, developed at the Norwegian University of Science and Technology, utilizes a rigid-lid by default. The program can account for the effects of multiple sediment sizes, sorting, inflowing bed load and suspended load, bed forms and/or the effects of sloping beds. In addition, SSIIM is capable of modeling sediment transport through channels with complex geometries.

3.2.1 Hydrodynamic Calculation

As described in the SSIIM User's Manual (Olsen, 2004) the SSIIM program solves the Navier-Stokes equations (Equation 2.11) with the κ-ε model (Equation 2.17) on a three-dimensional, structured non-orthogonal grid. A control volume method is used for the discretization, together with the power-law scheme or the second order upwind scheme. The SIMPLE method is used for the pressure coupling. Olsen (2004) suggests Patankar (1980), Melaaen (1992), and Olsen (1991) for a further description of these methods.

3.2.2 Sediment Transport Calculation

SSIIM calculates sediment transport by size fractions. Fraction, diameter, and fall velocity data must be given by the user. Suspended load and bedload transport are calculated separately. The sediment deposition pattern is obtained by using the velocities to solve the convection-diffusion equations for the different sediment sizes. The convection-diffusion equation is given by

$$\frac{\partial c}{\partial t} = U_j \frac{\partial c}{\partial x_j} + w\frac{\partial c}{\partial z} = \frac{\partial}{\partial x_j}\left(\Gamma_T \frac{\partial c}{\partial x_j}\right) \tag{3.2}$$

where c is the sediment concentration or, in this case, the volume fraction. The fall velocity of the sediments is given as w. The diffusion coefficient, Γ, is from the κ-ε model. It is defined as

$$\Gamma = \frac{\nu_T}{Sc} \tag{3.3}$$

where Sc is the dimensionless Schmidt number. This number is a correction factor for the deviation between the turbulent diffusivity and the eddy-viscosity. SSIIM uses a default value of 1.0.

For the suspended load close to the bed the SSIIM program uses the following equation developed by van Rijn (1984).

$$c_{bed} = 0.015 \frac{D^{0.3}}{a} \frac{\left[\frac{\tau - \tau_c}{\tau_c}\right]^{1.5}}{\left[\frac{(\rho_s - \rho_w)g}{\rho_w \nu^2}\right]^{0.1}} \tag{3.4}$$

The sediment particle diameter is given as D. The reference level, a, is set equal to the roughness height and the kinematic viscosity of the fluid is denoted as ν.

The volumetric bedload, q_b, is calculated using van Rijn's bedload transport formula (Equation 2.22).

The order in which the flow and sediment transport calculations are performed is presented in Figure 3.4. Olsen (1991) explains that a time series of several macro time steps is used to solve the velocity and turbulence equations. The macro time step is divided into a time series of micro time steps, where the flow field from the macro step is

assumed to be correct and the suspended sediment calculations are solved. The micro time step is further divided into a time series of sub-micro time steps, where the bed sediment grain size distribution and the change in bed elevation are recalculated.

3.2.3 Outblocking Option

This option allows for a region of the structured grid to be blocked out by a solid object. For example, this option was used to define the location of the submerged groynes in the channel bend sections.

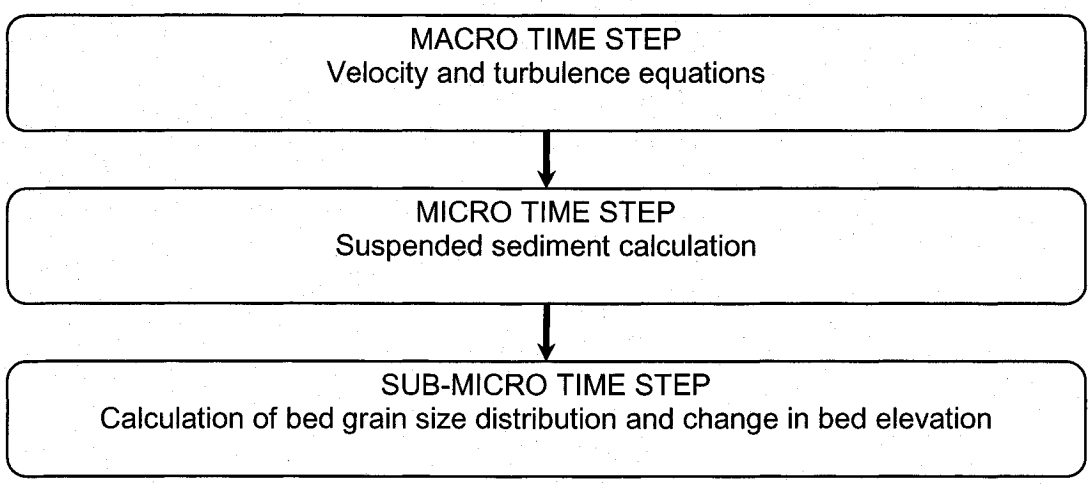

Figure 3.4 Time step hierarchy for multiple grain sizes (Olsen, 1991)

The user is able to choose if wall laws will be applied and, if so, whether they will be applied to: (i) the sides of the block; (ii) the sides and the top of the block; or (iii) the sides, the top, and the bottom of the block. Up to forty-nine regions in the grid can be blocked out.

The grid changes as modeling progresses. This results in a vertical movement of the grid intersections. For modeling scour around submerged structures it is possible to fix grid surfaces to prevent movement of the grid intersection. A maximum of nine surfaces can be fixed.

3.3 Numerical Simulation

3.3.1 Reference Data Set

The three-dimensional numerical model was initially used to simulate the sediment transport and flow through the 90 and 135° channel bend without barbs in place. These simulations were performed to analyze the sensitivity of the model to the input parameters before the barbs were added to the channel. Furthermore, the simulation of the channels without barbs provides a reference set of bed elevation and flow data. The results of subsequent numerical simulations of the 90 and 135° channels that contain barbs will be compared to this reference data set. This comparison will provide insight into the effect that a series of barbs has on bed elevation patterns and the flow field.

The values of channel geometry, discharge, average flow depth, channel slope, and sediment grain size that were measured in the laboratory were used for the numerical simulation in order to remain consistent with the experimental data. Also, the simulation time was set equal to the length of time taken to run the laboratory experiment. The SSIIM model allows for some of its default parameters to be changed, while others are hardcoded and cannot be changed by the user. Furthermore, several of the SSIIM modules have not been well tested and are prone to instabilities. The parameters that were

adjusted to calibrate the model were the Shields critical shear stress and bed roughness. The time step and grid size were varied to analyze their effect on the model convergence. During the calibration process and the analysis of time step and grid size, computation times typically exceeded 120 h. However, it was found that the parameters listed in Table 3.3 allowed for the model to converge within a practical amount of time. The values of the parameters used for the simulation are presented in Table 3.3.

Table 3.3 Numerical model input parameters for reference channels

Parameter	Value
Channel width	0.460 m
Discharge	0.0132 m^3/s
Flow depth,	0.10 m
Channel slope	0.001
Sediment grain size	0.00085 m
Simulation time – 90° channel	26 h
Simulation time – 135° channel	26 h
Approximate computation time – 90° channel*	5 h
Approximate computation time – 135° channel*	5 h
Time step – 90° channel	50 s
Time step – 135° channel	10 s
Grid size – 90° channel	123 longitudinal x 18 transverse x 12 vertical
Grid size – 135° channel	164 longitudinal x 18 transverse x 12 vertical
Shields critical shear stress – 90° channel	0.055
Shields critical shear stress – 135° channel	0.030
Manning number – 90° channel	0.0167
Manning number – 135° channel	0.0167

*simulations conducted on a Pentium IV, 2.46 GHz, 256 MB RAM

For the 90° channel without barbs, a simulation time of 26 h was used for the numerical modeling. For the time step it was necessary to find a value that allowed the model to converge, yet did not result in excessive computation time. A time step of 50 s proved to

be a good compromise. A structured grid containing 123 cells in the longitudinal direction, 18 cells in the transverse direction, and 12 cells in the vertical direction was used. This grid was used for both the reference simulation and the numerical simulations of the channel containing barbs.

A similar procedure was used for the 135° channel bend. As a first step, the three-dimensional model was used to simulate the sediment transport and flow through the 135° channel bend without barbs in place. The structured grid for this channel bend contained 164 cells in the longitudinal direction, 18 cells in the transverse direction, and 12 cells in the vertical direction. Once again, this grid was used for both the reference simulation and the numerical simulations of the channel containing barbs. The discharge, flow depth, channel slope, and sediment grain size remained the same as for the 90° channel bend. A simulation time of 26 h was used. A Manning number of 0.0167 and a time step of 10 s proved to yield favorable results. It is noted that the 135° channel required a lower Shields critical shear stress value than the 90° channel.

For both the 90 and 135° channels the following maps were generated: a bed elevation contour map; depth-averaged horizontal velocity map; and shear stress distribution map. Currently the validation of a numerical model within the hydrological sciences is not based on formal criteria (Bates et al., 2005). The validation of numerical models is often subjective and poorly defined (Oreskes and Belitz, 2001). Statistical analyses were performed for each simulation to validate the application of the SSIIM model to moveable-bed bend sections of a hydraulically narrow rectangular channel containing

barbs. This included the analysis of the regression coefficient of determination (r^2); the regression slope; the mean absolute deviation (MAD); and the standard deviation of absolute deviation (SDAD). The r^2 gives the model precision. The regression slope and intercept give the accuracy of the model. The MAD is a measure of the mean error. It is calculated by Equation 3.5.

$$MAD = \frac{\sum abs(measured - predicted)}{n} \tag{3.5}$$

Therefore, the MAD is calculated by taking the sum of the absolute value of the predicted elevation subtracted from the measured elevation. This is then divided by n, the total number of data points.

The SDAD is a measure of the variability of error. It is calculated with Equation 3.6.

$$SDAD = \sqrt{\frac{\sum (abs(measured - predicted) - MAD)^2}{n-1}} \tag{3.6}$$

It is noted that there is not a defined level of precision or level of accuracy for the validation of a numerical model. However, it is recognized that a high r^2 (i.e. close to 1) indicates greater precision and a regression slope close to 1 suggests greater accuracy. Furthermore, it is acknowledged that discrepancies between measured and predicted data do not necessarily mean that the model is wrong or invalid (Bates et al., 2005). An

analysis of the boundary condition data and the measured data must be performed to identify and explain possible sources of error.

3.3.2 Channel Containing Barbs

The height and length of the barbs used for the simulation of both the 90 and 135° channel were the same. For all numerical simulations, only the barb height to flow depth ratio of 0.5 was used. The laboratory experiments used barbs whose lengths did not extend further than 22 percent of the total channel width in the transverse direction. Therefore, the length of the barb differed depending on the barb alignment angle. The barb lengths are presented in Table 3.4. These are also the barb lengths that were used for the numerical simulations of both the 90 and 135° channels.

Table 3.4 Length of barbs

Barb alignment angle, θ	Length of barb (m)
20	0.297
30	0.196
40	0.160

For the laboratory experiments it was found that a barb width greater than 1 centimeter resulted in severe scouring. Thus, the barb width was kept below this value. However, for the numerical simulation the width of the barb was limited by the grid sizes listed in Table 3.3. For example, the 90° channel had a transverse grid spacing of 2.54 cm and a longitudinal grid spacing of 2.0 cm. When the locations of the barbs were defined in the SSIIM program, a minimum of two cells in the longitudinal direction were blocked out. Therefore, the minimum width of a barb is approximately 4.7 cm. The width will vary to

some extent depending on the barb alignment angle. Figure 3.5 illustrates, in plan view, how a barb is defined in the SSIIM model. The thicker lines outline the area of the grid that has been blocked out (i.e., the barb).

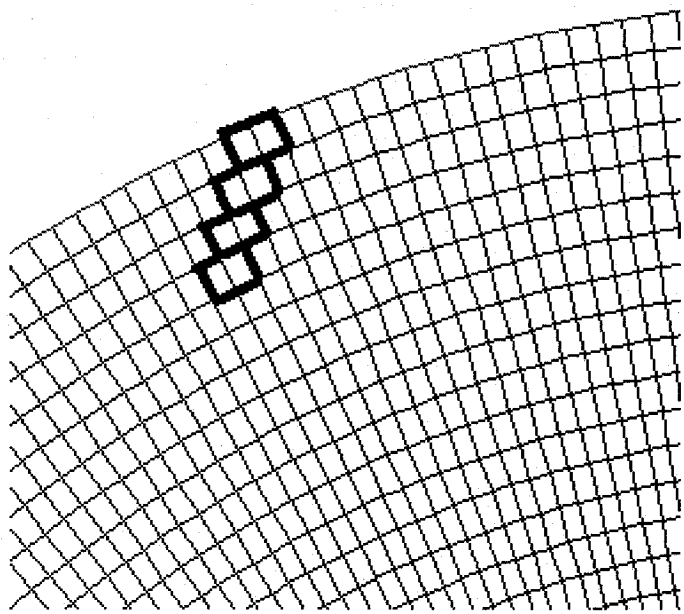

Figure 3.5 SSIIM grid showing cells blocked out to define a barb (plan view)

It can be observed that, in addition to being wider, the simulated barbs do not have smooth sides. Furthermore, the barbs in the SSIIM model are impermeable whereas the barbs used for the laboratory experiments were constructed of a wire mesh and were slightly permeable.

For the laboratory experiments, the height of the barbs at the bank was half of the mean flow depth and decreased with a 10 degree slope away from the bank. This slope was also

used for the simulated barbs in the 90° channel. Figure 3.6 shows an example of a transverse cross-section of a grid containing a barb.

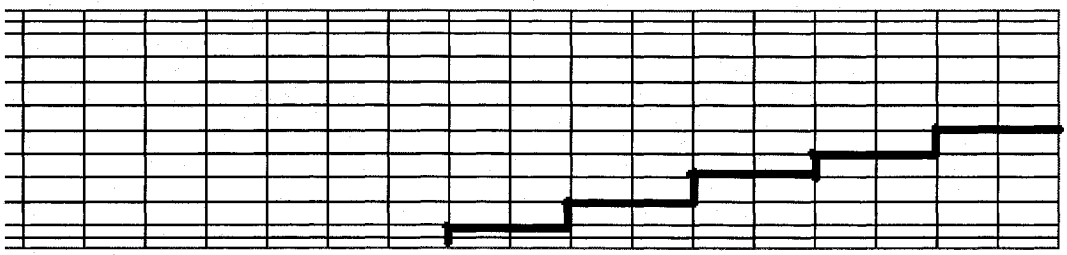

Figure 3.6 Cross-section of SSIIM grid showing cells blocked out to define a barb

Once again, the thicker lines outline the area of the grid that has been blocked out (i.e., the barb). It can be seen that a barb slope can be defined. However, it can be noted that the barb crest slopes down in steps rather than being a smooth, constant slope.

As discussed in Section 3.2, the grid changes as modeling progresses and results in a vertical movement of the grid intersections. For this reason, for every simulation the grid surfaces were fixed to prevent this movement. However, this option is limited to a maximum of nine surfaces, where each step must be defined as a separate surface. Given the dimensions of the barbs, a maximum of only three sloped barbs could be defined for the 90° channel. For this reason barb Group D was not simulated for the 90° channel. The experiments for the 135° channel contained a minimum of five barbs. Thus, it was not possible to define the slope for the barbs used in the numerical simulations of the 135° channel.

3.3.2.1 90° Channel

As a result of the laboratory experiments the optimum barb arrangement for the 90 and 135° channel bends was found to be Group B with a barb alignment angle of 30°. The barb arrangements that were chosen to be simulated were chosen based on these findings. Five barb arrangements in the 90° channel were simulated. The numerical model was used to simulate Group B for the three alignment angles (θ = 20°, 30°, and 40°). Also, three barb groups (A, B, and C) were simulated with a barb alignment angle of 30°. The barb arrangements for the numerical simulations of the 90° channel containing barbs are detailed in Table 3.5.

Table 3.5 Barb locations in 90° channel bend for numerical simulation

Alignment angle, θ	Group-type	Barb location / Channel width		
		Barb 1	Barb 2	Barb 3
20	B	3.08	4.01	4.98
30	A	2.67	3.56	4.82
	B	3.08	4.08	5.07
	C	1.78	2.75	3.61
40	B	3.08	3.87	4.68

The measured bed elevation contour maps for the barb arrangements listed in Table 3.5 are presented in Figures A.1, A.2, A.3, A.4, and A.5 in Appendix A.

Laboratory experiments for the 90° channel containing barbs were run for 5 h. As with the reference channels, the simulation time for the model was set equal to the length of time for the laboratory runs. An analysis of the convergence parameters showed that a time step of 50 s, in combination with the grid used for the 90° reference channel, allowed the model to converge yet did not result in excessive computation time. After

calibrating the numerical model to the experimental data the following parameters were found to yield the best results: a Shields critical shear stress of 0.037; and a Manning number equal to 0.015. The values of measured discharge and flow depth from the laboratory experiments were used for the numerical simulations. These values varied slightly for different experimental tests. The input parameters for the 90° channel containing barbs are listed in Table 3.6.

Table 3.6 Numerical model input parameters for 90° channel containing barbs

Parameter	Value
Channel width	0.460 m
Channel slope	0.001
Sediment grain size	0.00085 m
Simulation time	5 h
Approximate computation time*	10 h
Time step	50 s
Shields critical shear stress	0.037
Manning number	0.015
Grid size	123 longitudinal x 18 transverse x 12 vertical
Discharge – Group B, $\theta = 20^{\circ}$	0.0134 m^3/s
Discharge – Group B, $\theta = 30^{\circ}$	0.0132 m^3/s
Discharge – Group B, $\theta = 40^{\circ}$	0.0132 m^3/s
Discharge – Group A, $\theta = 30^{\circ}$	0.0132 m^3/s
Discharge – Group C, $\theta = 30^{\circ}$	0.0132 m^3/s
Flow depth - Group B, $\theta = 20^{\circ}$	0.102 m
Flow depth - Group B, $\theta = 30^{\circ}$	0.10 m
Flow depth - Group B, $\theta = 40^{\circ}$	0.102 m
Flow depth - Group A, $\theta = 30^{\circ}$	0.10 m
Flow depth – Group C, $\theta = 30^{\circ}$	0.10 m

*simulations conducted on a Pentium IV, 2.46 GHz, 256 MB RAM

As with the reference data set, the following maps were generated: a bed elevation contour map; depth-averaged horizontal velocity map; shear stress distribution map; and the difference between the predicted and measured bed elevations were presented as a contour map. Also, a statistical analysis was performed for each simulation to determine

the r^2, the MAD, and the SDAD. The SSIIM input files for the 90° reference channel and for the 90° channel containing Group B, with an alignment angle of 30°, are included in Appendix D.

3.3.2.2 135° Channel

A similar procedure was used for the 135° channel bend. Three barb arrangements were simulated. The numerical model was used to simulate Group B for the three alignment angles (i.e., $\theta = 20°$, 30°, and 40°). The barb arrangements for the numerical simulations of the 135° channel containing barbs are detailed in Table 3.7.

Table 3.7 Barb locations in 135° channel bend for numerical simulation

Alignment angle, θ	Group-type	Barb location / Channel width				
		Barb 1	Barb 2	Barb 3	Barb 4	Barb 5
20	B	3.08	3.98	4.82	5.72	7.20
30	B	3.08	4.01	4.82	5.57	6.87
40	B	3.08	3.87	4.62	5.24	6.20

The measured bed elevation contour maps for the barb arrangements listed in Table 3.7 are presented in Figures A.6, A.7, and A.8 in Appendix A.

A simulation time of 5 h was used to correspond to the time frame used during laboratory tests. After calibrating the numerical model to the experimental data the following parameters were found to yield the best results: a Shields critical shear stress of 0.030; and a Manning number equal to 0.015. A time step of 5 s, with the grid used for the 135° reference channel, allowed the model to converge yet did not result in excessive computation time. The values of measured discharge and flow depth from the laboratory

experiments were used for the numerical simulations. For all simulations of the 135° channel containing barbs the flow depth was 0.103 m and the discharge was 0.132 m^3/s. The input parameters for the 135° channel containing barbs are listed in Table 3.8.

Table 3.8 Numerical model input parameters for 135° channel containing barbs

Parameter	Value
Channel width	0.460 m
Channel slope	0.001
Sediment grain size	0.00085 m
Simulation time	5 h
Approximate computation time*	10 h
Time step	5 s
Shields critical shear stress	0.030
Manning number	0.015
Grid size	164 longitudinal x 18 transverse x 12 vertical
Discharge – all barb arrangements	0.0132 m^3/s
Flow depth – all barb arrangements	0.103 m

*simulations conducted on a Pentium IV, 2.46 GHz, 256 MB RAM

As with the reference data set and the 90° channel containing barbs, the following maps were generated: a bed elevation contour map; depth-averaged horizontal velocity map; shear stress distribution map; and the difference between the predicted and measured bed elevations were presented as a contour map. In addition, a statistical analysis was performed for each simulation to determine the r^2, the MAD, and the SDAD.

4.0 Results and Analysis

4.1 90° Channel

4.1.1 90° Reference Channel

The three-dimensional numerical model was initially used to simulate the sediment transport and flow through the 90° channel bend without barbs in place. The input parameters listed in Table 3.3 were used for the simulation. The resulting bed elevation contour map, depth-averaged velocity vector map, and shear stress distribution maps are presented in Appendix B in Figures B.1, B.2, and B.3, respectively.

Figure B.1 presents a contour map of the predicted reference bed elevations in meters. The distribution of bed shear stress across a channel bend section is complex due to the transverse shear produced by the secondary currents. The secondary flow cell is typically directed vertically down towards the toe of the outside bank. There is an increase in the shear stresses in the outer bank region which results in erosion in the outer bank region. Conversely, there is a decrease in velocity and bed shear stress along the inside bank which encourages deposition of sediment and the formation of point bars.

The measured bed elevations, presented in Figure 3.2, agree with this pattern of erosion and deposition. It can be observed that a scour hole has developed along the outer bank, with the deepest point measuring –0.07 m and located 0.15 m after the bend exit. From Figure B.1 it can be seen that these patterns of sediment deposition and erosion through the bend are sufficiently simulated by the numerical model. The location and magnitude

of the measured and predicted point bar are observed to be comparable. The maximum measured elevation was +0.04 m while the maximum predicted elevation was +0.05 m. The predicted scour hole is of greater magnitude than the measured scour hole and located further downstream. The numerical model predicted a maximum scour depth of −0.09 m, located +0.30 m downstream of the bend exit. Also, it is observed from Figure B.1 that the predicted scour hole is located closer to the outside bank and its shape is elongated. Nevertheless, the numerical model adequately simulated the patterns of sediment erosion and deposition through the channel.

A statistical analysis of the measured and predicted bed elevations for the 90° channel bend was performed to determine the regression coefficient of determination, the mean absolute deviation and the standard deviation of absolute deviation. In Figure 4.1 the measured bed elevation data is plotted versus the bed elevation data predicted by the numerical model. A linear regression line of the data gives an r^2 of 0.81. The MAD of predicted from measured bed elevations was found to be 0.0111 m. The SDAD was 0.0104 m. The regression equation is shown in Figure 4.1, with a slope of 1.198. A slope that is not equal to one suggests an overestimation of scour and/or deposition by the numerical model.

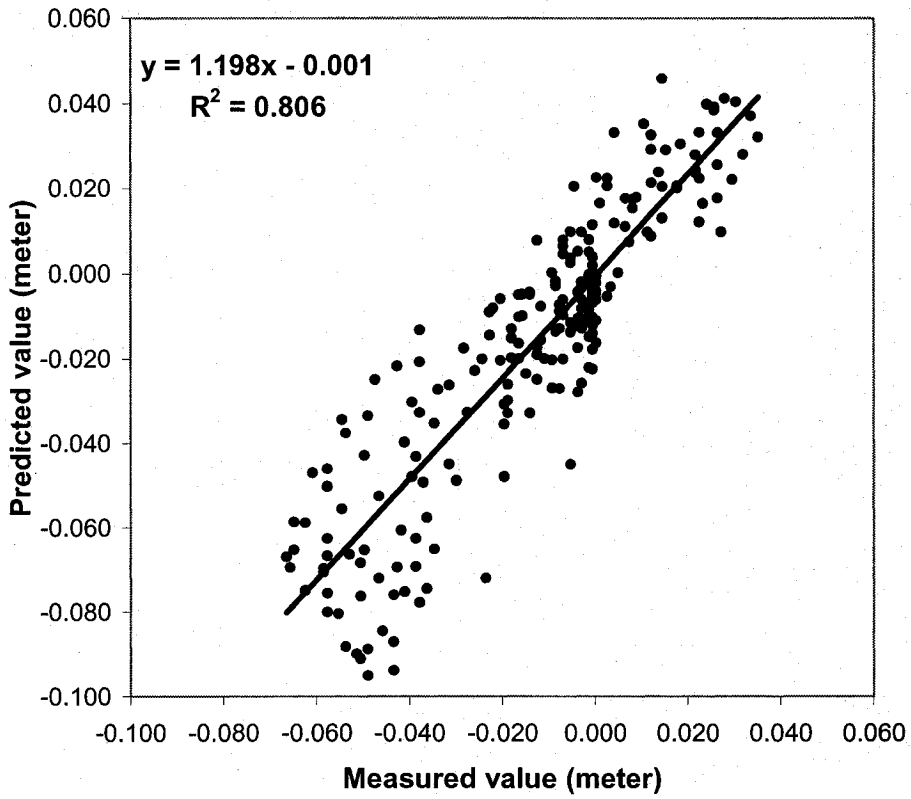

Figure 4.1 Predicted versus measured bed elevation for 90° reference channel

The differences between the measured and predicted bed elevations (i.e., predicted – measured) are presented in Figure 4.2. From this contour map it can be seen that the numerical model is predicting slightly higher bed elevations in the region of the point bar. However, the greatest discrepancies between measured and predicted bed elevations are in the region of the outer bank scour hole. The model is predicting lower bed elevations in this area. Therefore, it appears that the numerical model is over-estimating erosion in the outer bank region. To a lesser degree, the model is also over-estimating deposition in the near-bank region.

Detailed measurements of the velocity field were not taken during the laboratory experiments. For the 90° reference channel an average velocity of 0.285 m/s was recorded. This was determined simply by dividing the discharge, measured with the v-notch weir, by the cross-sectional flow area. Regardless, the predicted velocity field for the 90° reference channel was analyzed in order to observe trends in the data. The average magnitude of the simulated depth-averaged horizontal velocity vectors was 0.232 m/s. The simulated depth-averaged horizontal velocity vectors for the 90° channel are presented in Figure B.2. A maximum depth-averaged magnitude of 0.320 m/s was observed 25° into the channel bend in the center of the channel. The minimum value of depth-averaged velocity was 0.00551 m/s, located along the inner bank.

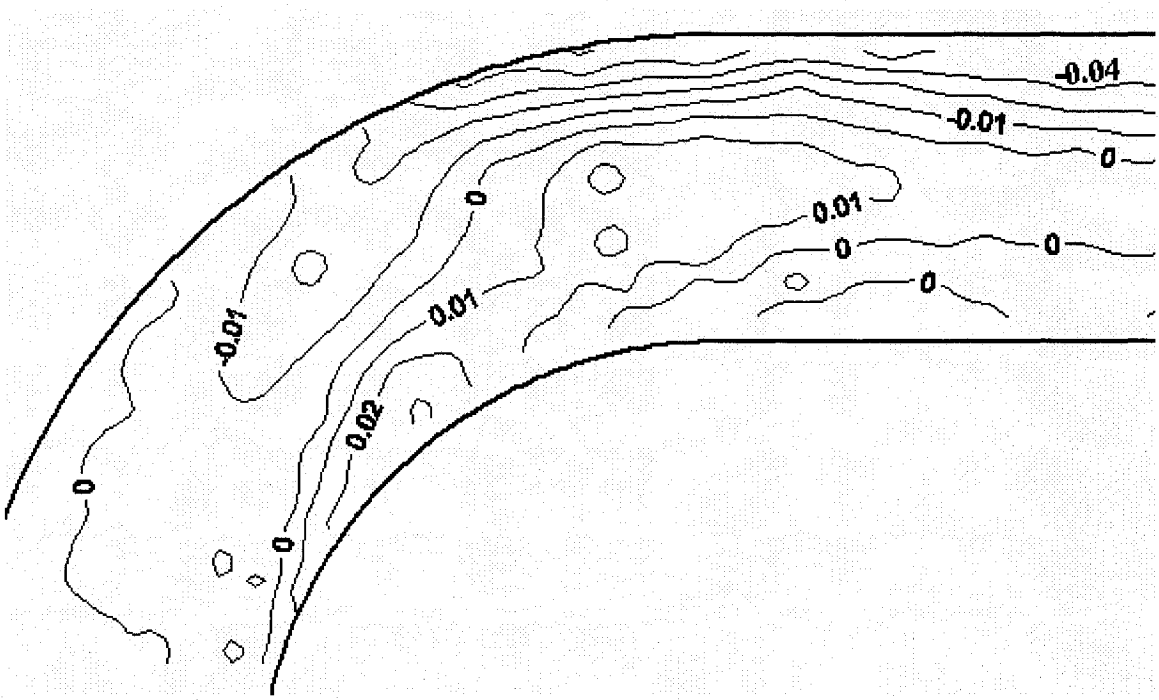

Figure 4.2 Measured bed elevation subtracted from predicted bed elevation for 90° reference channel (m)

It can be seen from Figure B.2 that as the flow continues through the bend the location of maximum horizontal velocity shifts toward the outer bank and there is a decrease in velocity along the inner bank. For a further analysis of the flow field, velocity vectors located along the cross-section located 0.15 m downstream of the bend exit are shown in Figure 4.3. This figure confirms the presence of secondary currents within the channel. As previously discussed, the secondary flow cell is directed vertically down towards the toe of the outside bank and vertically up at the inner bank. The numerical model uses a rigid lid (i.e., water surface is constant in the transverse direction) therefore it is not possible to observe the superelevation of the water surface along the outer bend and the subsequent formation of the outer bank flow cell. However, the simulated flow trends agree with the theory discussed in Section 2.4.1.

As further validation of these trends, the distribution of bed shear stress through the 90^{o} reference channel is presented in Figure B.3. It can be observed that the maximum bed shear stress (1.45 N/m^2) occurs in the same region as the maximum scour and velocity. The lowest bed shear stress (0.08 N/m^2) is located along the inner bank, in the same region as the point bar and the lowest depth-averaged horizontal velocity.

Although it is not possible to compare the flow field and bed shear stress data to measured values, it can be stated that the numerical model has successfully simulated the expected trends of flow, sediment deposition, and bed shear stress through a channel bend. It was observed that both velocity and bed shear stress increased in the outer bank region. Conversely, a decrease of these parameters was observed along the inner bank.

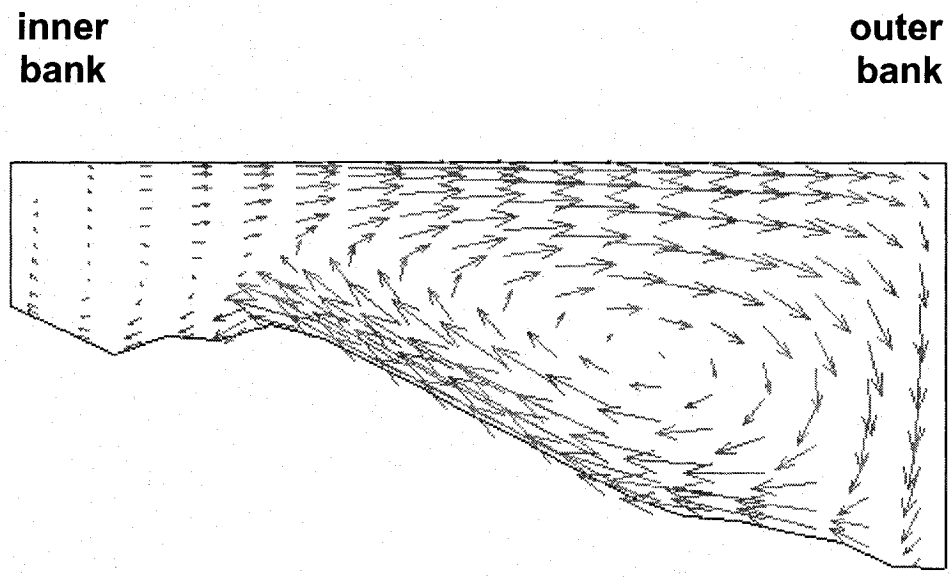

Figure 4.3 90° reference channel cross-section showing secondary currents 0.150 m downstream of bend exit

From Figure 4.3 it was possible to visualize the secondary currents through the channel bend. As anticipated, the secondary flow cell was directed vertically down towards the toe of the outside bank and vertically up along the inner bank. As a result of these trends, scouring was observed in the outer bank region and sediment was deposited along the inner bank.

4.1.2 90° Channel Containing Barbs

Once the simulation of the reference channel was completed, the three-dimensional numerical model was used to simulate the 90° channel containing the barb groups listed in Table 3.5. Therefore, five separate simulations were performed. The predicted bed elevation contour maps, depth-averaged horizontal velocity maps, and bed shear stress

distributions of the 90° channel containing each of the five barb arrangements are presented in Appendix B.

It is suggested that the primary functions of a series of barbs in a channel bend are to: redirect flow away from the outer stream bank; disrupt the velocity gradient and shear stress distribution close to the outer bank; shift thalweg away from the outside bank; protect outer bank from erosion; promote sediment deposition in the outer bank region; and create scour holes at the barb tip to enhance aquatic habitat. The measured data and the simulated data confirm and substantiate these processes for a series of barbs, angled upstream, in a 90° channel bend for various barb spacing and alignment angles.

4.1.2.1 90° Channel Containing Group-B (θ = 20°)

The predicted bed elevation contour map for the 90° channel containing barb Group-B, with a barb alignment angle of 20°, is presented in Figure B.4. The corresponding depth-averaged velocity vector map and shear stress distribution maps are presented in Figures B.5 and B.6, respectively.

The measured bed elevation contour presented in Figure A.1 shows that, with the addition of the barb group, the thalweg has shifted away from the outer bank and the location of the deepest scour hole is located between the second and third barb. The bed elevations computed by the numerical model presented in Figure B.4 show similar trends. It can be observed that the location of the thalweg has shifted away from the outer bank and, comparable to Figure A.1, the location of the deepest scour hole is located between

the second and third barb. In comparison with the measured and simulated 90° reference channels in Figures 3.2 and B.1, respectively, it can be noted that with the movement of the thalweg away from the outer bank, the erosion in the outer bank region has decreased. Furthermore, sediment deposition can be observed in the outer bank region, adjacent to the third barb in the group, from both the measured and simulated data.

The magnitude of minimum and maximum elevation predicted by the numerical model compares favorably with the measured data. The numerical model predicted a minimum elevation of –0.0740 m. The minimum measured elevation was –0.0786 m, located one cross-section upstream from the location of the predicted value. The predicted maximum elevation, located along the inner bank, was +0.0407 m. The maximum measured elevation was +0.0349 m, located at the same point.

In Figure 4.4 the measured bed elevation data are plotted versus the bed elevation data predicted by the numerical model. A linear regression line of the data gives an r^2 of 0.79. The MAD of predicted from measured bed elevations was found to be 0.0084 m. The SDAD was 0.0091 m.

The depth-averaged horizontal velocity vectors are shown in Figure B.5. In comparison to the velocity profile for the 90° reference channel (i.e., Figure B.2); it can be observed that the region of maximum velocity has shifted towards the center of the channel. From Figure B.5, it can be seen that the velocity gradient along the outer bank has been disrupted by the barbs. The lowest velocity vectors are now located in the outer bank

region. A region of low velocity also occurs along the inner bank, in the vicinity of the point bar. The minimum predicted depth-averaged horizontal velocity was 0.121 m/s, and located along the outer bank of the channel bend. The maximum velocity magnitude was predicted to be 0.325 m/s, located at the center of the channel. The averaged velocity measured in the laboratory was 0.283 m/s. The numerical model predicted an averaged depth-averaged horizontal velocity of 0.266 m/s.

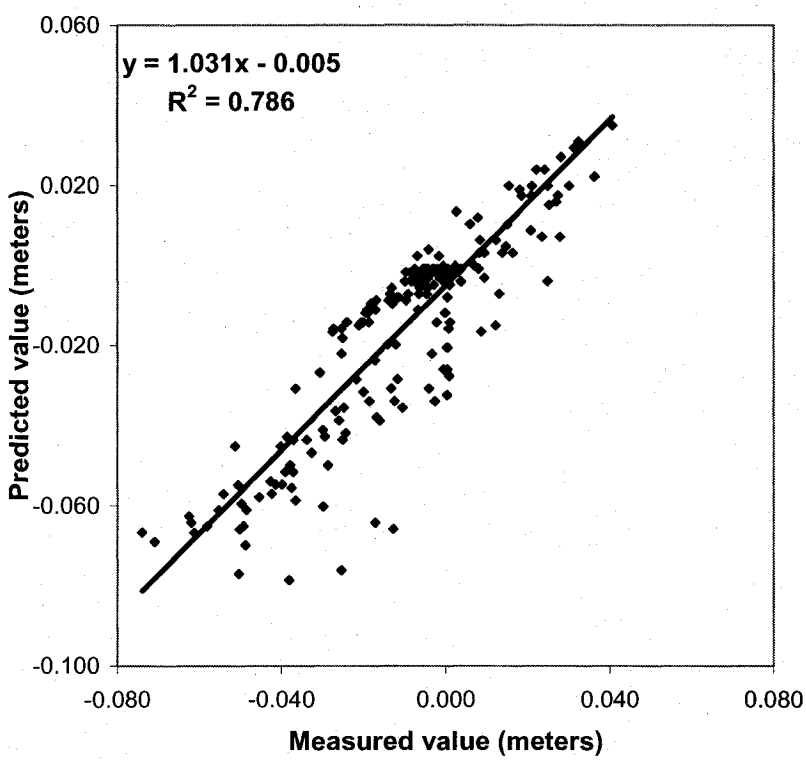

Figure 4.4 Predicted versus measured bed elevation for 90° channel (Group B, θ=20°)

The simulated bed shear stress distribution is presented in Figure B.6. The channel boundary and barbs are defined in red. It can be observed that the distribution of the bed shear stress corresponds to the predicted velocity profile and the sediment deposition

trends. The higher bed shear stresses are located along the center of the channel and at the tip of the third barb. It can be observed from the predicted bed elevation map, Figure B.4, that the minimum bed elevations were located in this region. Furthermore, the maximum depth-averaged horizontal velocities were observed to be located along the center of the channel. The lowest bed shear stresses are located along the outer bank, in the same region as the barbs and the lowest depth-averaged horizontal velocity. There is also a low shear stress region along the inner bank in the region of the point bar.

Although it was not possible to compare the flow field and bed shear stress data to measured values, it can be stated that the numerical model successfully simulated the expected trends of flow, sediment deposition, and bed shear stress through a channel bend containing a series of barbs. It was observed that: the thalweg shifted away from the outer bank towards the tips of the barbs; sediment deposition occurred along the outer bank, adjacent to the third barb in the group; a scour hole was created between the second and third barb in the group; the zone of maximum velocity shifted away from the outer bank towards the center of the channel; and the bed shear stress and velocity were reduced in the outer bank region.

4.1.2.2 90° Channel Containing Group-A (θ = 30°)

The predicted bed elevation contour map for the 90° channel containing barb Group-A, with a 30° alignment angle, is presented in Figure B.7. The depth-averaged velocity vector map and shear stress distribution maps for this channel are shown in Figures B.8 and B.9, respectively.

The trends observed from the bed elevation map are similar to those discussed in Section 4.1.2.1 (i.e., Group A, $\theta = 20^{o}$). The deepest elevation predicted is -0.0617 m, and is located off the tip of the third barb in the group. The maximum measured scour depth for this channel was -0.0722 m, located in the same position. The predicted maximum elevation, located along the inner bank, was +0.0476 m. The maximum measured elevation was +0.0357 m, located 0.150 m upstream of the predicted value.

The measured bed elevation data are plotted versus the bed elevation data predicted by the numerical model in Figure 4.5. A linear regression line of the data gives an r^2 of 0.77. The MAD of predicted from measured bed elevations was found to be 0.0091 m. The SDAD was 0.0083 m.

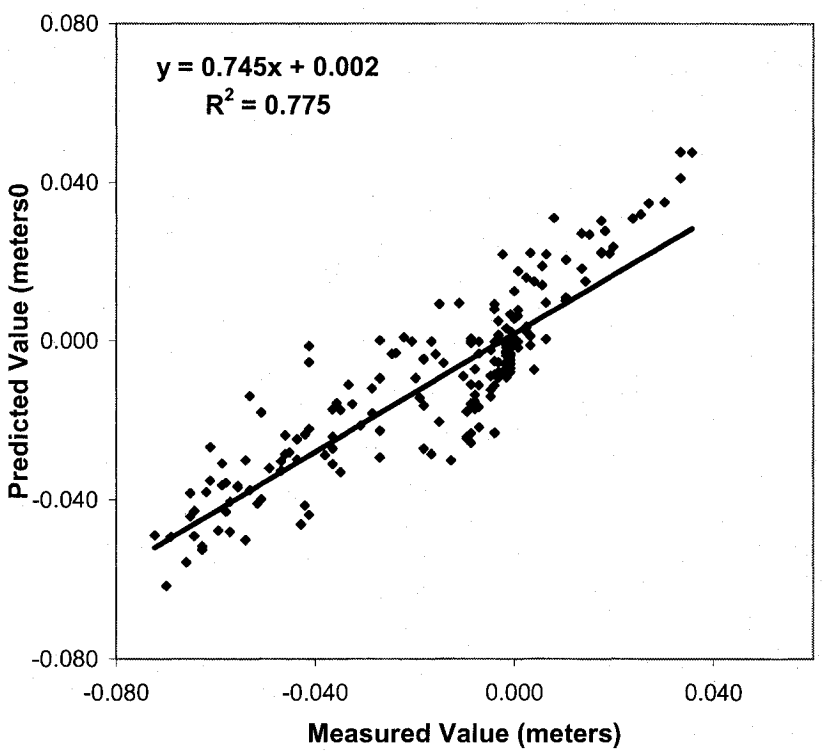

Figure 4.5 Predicted versus measured bed elevation for 90° channel (Group A, $\theta = 30^{o}$)

From the depth-averaged velocity profile presented in Figure B.8 it can be seen that the trends are, once again, similar to those observed with Group B ($\theta = 20^{o}$). The model predicted a minimum depth-averaged horizontal velocity of 0.118 m/s, and a maximum of 0.330 m/s. The average velocity measured in the laboratory was 0.282 m/s. The predicted average was 0.267 m/s.

The bed shear stress profile, presented in Figure B.9, was also comparable to the results from the previous section, with a shear stress ranging from 0.05 to 0.71 N/m^2.

4.1.2.3 90° Channel Containing Group-B ($\theta = 30^{o}$)

As a result of the laboratory experiments the optimum barb arrangement for the 90° channel bend was found to be Group B with a barb alignment angle of 30°. The predicted bed elevation contour map, depth-averaged velocity vector map, and shear stress distribution for the 90° channel containing barb Group-B, with a 30° alignment angle, are presented in Figures B.10, B.11, and B.12, respectively.

Once again, the trends observed from this simulation were in close agreement with those observed with Group-B ($\theta = 20^{o}$), and Group-A ($\theta = 30^{o}$). The location of the deepest simulated scour hole, presented in Figure B.10, is between the second and third barb in the group. The lowest elevation predicted was -0.0619 m, while the lowest measured elevation was -0.0714 m. The differences between the measured and predicted bed elevations (i.e., predicted – measured) are presented in Figure 4.6.

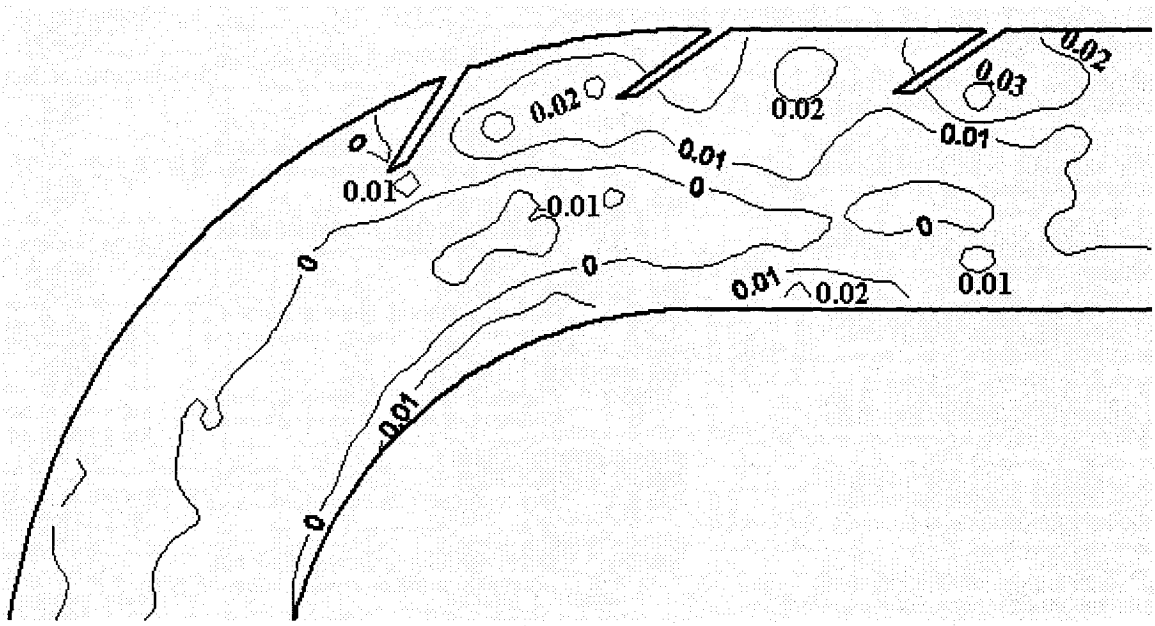

Figure 4.6 Measured bed elevation subtracted from predicted bed elevation for 90° reference channel in meters (Group B, $\theta = 30^{\circ}$)

From this contour map it can be seen that the numerical model is predicting slightly higher bed elevations in the region of the point bar and in the vicinity of the barbs.

The measured bed elevation data are plotted versus the bed elevation data predicted by the numerical model in Figure 4.7. A linear regression line of the data gives an r^2 of 0.82. The MAD of predicted from measured bed elevations was found to be 0.0079 m. The SDAD was 0.0074 m.

The depth-averaged velocity profile, presented in Figure B.11, shows similar trends to those observed with the other barb groups. The model predicted a minimum depth-averaged horizontal velocity of 0.124 m/s, and a maximum of 0.336 m/s.

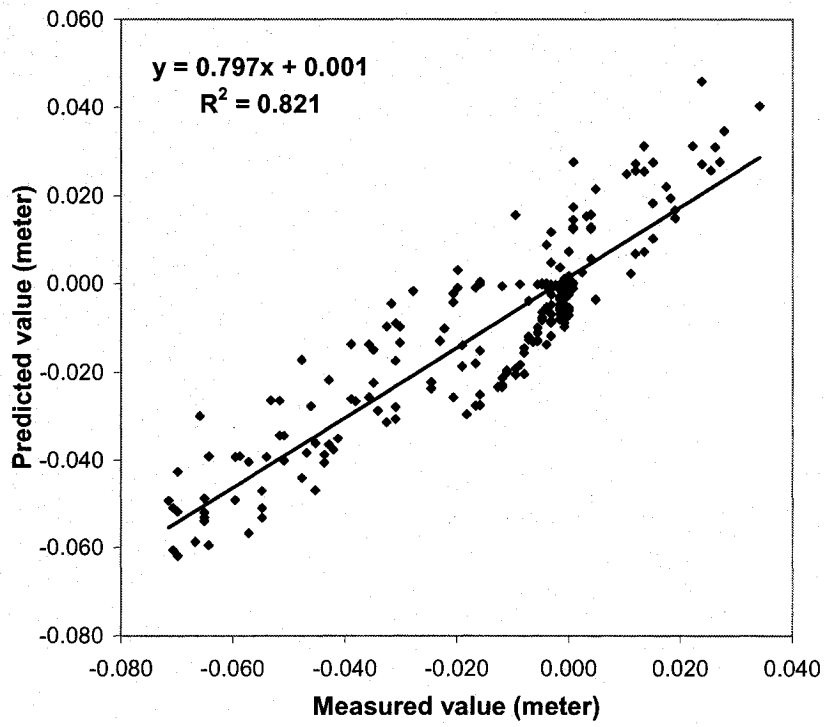

Figure 4.7 Predicted versus measured bed elevation for 90° channel (Group B, θ=30°)

The average velocity measured in the laboratory was 0.283 m/s. The predicted average was 0.265 m/s. For a further analysis of the flow field, velocity vectors located along the cross-section located at the tip of the third barb in the group are shown in Figure 4.8. It can be seen that the secondary flow cell has been disrupted in the near bank region. Similar to the reference channel, the velocity vectors are directed up at the inside bank.

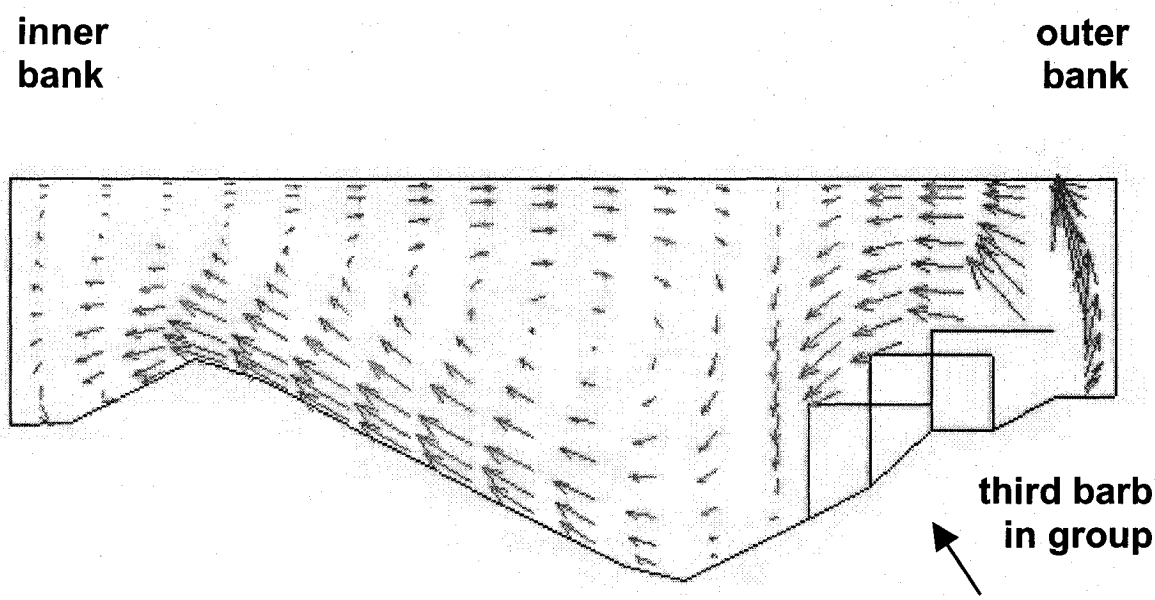

Figure 4.8 90° channel (Group B, θ = 30°) cross-section showing secondary currents at third barb in group

However, with the addition of the barb, the velocity vectors at the outer bank are not attacking the bank toe. Alternatively, the velocity vectors at the outer bank are directed downwards at the tip of the barb. In addition the velocity vectors in the outer bank region are directed away from the bank

The bed shear stress distribution, shown in Figure B.12, shows trends similar to the previous barb groups, with a minimum and maximum shear stress of 0.04 and 0.70 N/m^2, respectively.

4.1.2.4 90° Channel Containing Group-C (θ = 30°)

It can be observed in Table 3.5 that the location of the first barb in Group-C ($\theta = 30^{\circ}$) is located over thirty percent closer to the bend entrance than the barbs in Group-A and Group-B. Using the barb spacing methodology described in Section 2.5.2.2, four barbs are placed in the channel.

From the bed elevation contour map presented in Figure B.13, it is apparent that Group-C is also successful in shifting the thalweg away from the outer bank. The maximum scour hole is observed to be located off the tip of the third barb, on its downstream side. A maximum scour depth of –0.0832 m is predicted. This compares favorably to the maximum measured scour depth of –0.0802 m.

A statistical analysis reveals an r^2 of 0.73. The linear regression line of the predicted versus measured data is presented in Figure 4.9. The MAD of predicted from measured bed elevations was found to be 0.010 m. The SDAD was 0.009 m.

The depth-averaged horizontal velocity profile in Figure B.14 is similar to the other profiles produced by the other barb groups. However, this figure gives the best visualization of the redirection of velocity vectors away from the outside bank. This is especially clear as the vectors pass over the third and fourth barb in the group.

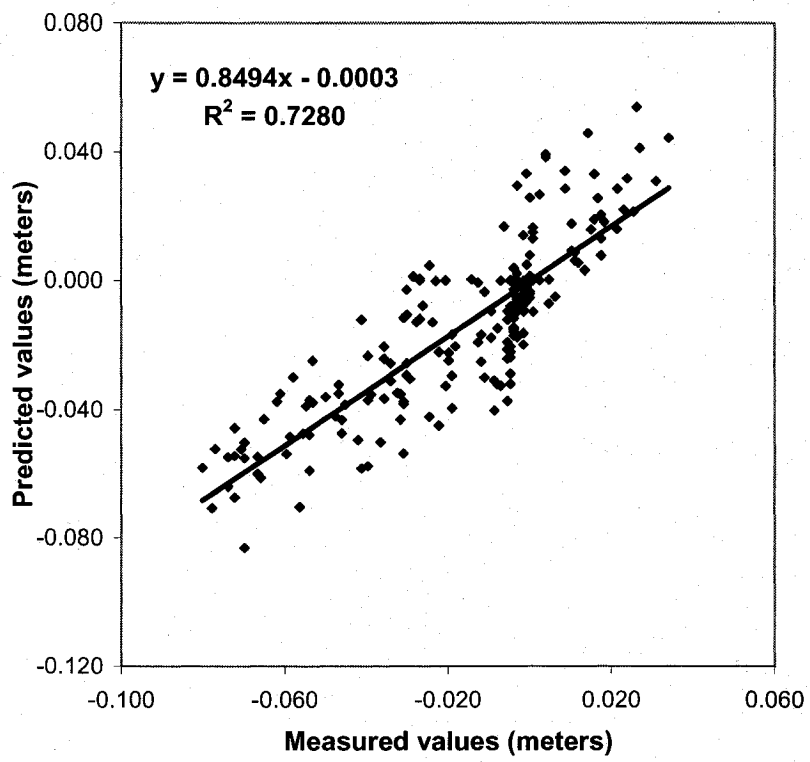

Figure 4.9 Predicted versus measured bed elevation for 90° channel (Group C, θ=30°)

The bed shear stress values from Figure B.15 range from 0.06 to 1.08 N/m^2. Once again, the shear stress distribution corresponds to both the distribution of velocity and the bed elevations.

4.1.2.5 90° Channel Containing Group-B (θ = 40°)

The predicted bed elevation contour map for the 90° channel containing barb Group-B, with a 40° alignment angle, is presented in Figure B.16. The depth-averaged velocity

vector map and shear stress distribution maps for this channel are shown in Figures B.17 and B.18, respectively.

The maximum scour hole observed in Figure B.16 is located between the second and third barb. A maximum scour depth of –0.069 m is predicted at this location. This compares to a maximum scour depth of –0.068 m measured in the laboratory.

The measured bed elevation data are plotted versus the predicted bed elevation data in Figure 4.10. A linear regression line of the data gives an r^2 of 0.75. The MAD of predicted from measured bed elevations was found to be 0.0079 m. The SDAD was 0.0079 m.

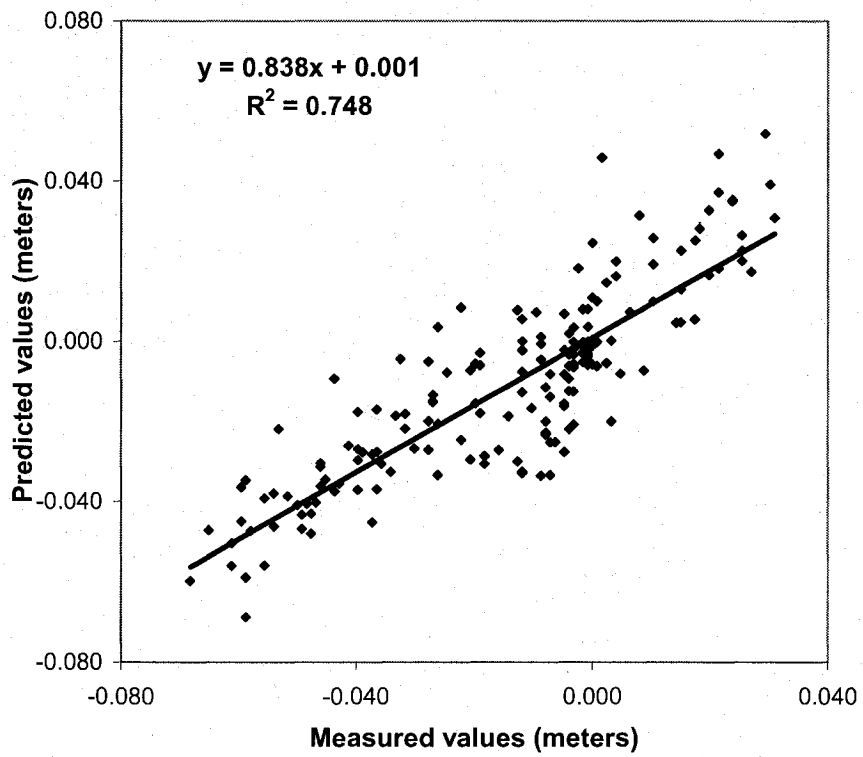

Figure 4.10 Predicted versus measured bed elevation for 90° channel (Group B, θ=40°)

The depth-averaged velocity profile, presented in Figure B.17, shows similar trends to those observed with the other barb groups. The model predicted a minimum depth-averaged horizontal velocity of 0.130 m/s, an average of 0.262 m/s, and a maximum of 0.335 m/s. The bed shear stress distribution, presented in Figure B.18, ranges from 0.04 to 0.67 N/m^2.

Therefore it is observed that the three-dimensional numerical model was used successfully to simulate flow and sediment transport through the hydraulically narrow 90° channel bend, which contained barbs. The predicted results showed: a disruption of the velocity gradient and shear stress distribution close to the outer bank; a movement of the thalweg towards the center of the channel; the creation of scour holes at the tips of the barbs; and an increased bed elevation along the outer bank.

4.2 135° Channel

4.2.1 135° Reference Channel

A similar procedure was used for the 135° channel bend. As a first step, the three-dimensional model was used to simulate the sediment transport and flow through the 135° channel bend without barbs in place. The input parameters listed in Table 3.3 were used for the simulation of the 135° reference channel. The resulting bed elevation contour map, depth-averaged velocity vector map, and bed shear stress distribution maps are presented in Appendix C in Figure C.1, C.2, and C.3, respectively.

The predicted bed elevations, presented in Figure C.1, agree with the patterns of erosion and deposition observed in the 90° reference channel, and discussed in Section 4.1.1.

Similar to the 90° channel bend, it can be observed that sediment is being deposited along the inner bank while erosion is occurring along the outer bank. Both the measured data, presented in Figure 3.3, and predicted data illustrate this trend. It can be observed that the predicted scour hole along the outer bank of the bend is smaller than the measured scour hole, and it is located further downstream. The lowest elevation predicted by the numerical model is –0.106 m, located at the bend exit (i.e., 135° into the bend section). The lowest elevation measured in the laboratory was located 0.30 m upstream of the bend exit, and had a value of –0.127 m.

A statistical analysis, presented in Figure 4.11, of the predicted and measured data gives an r^2 of predicted from measured bed elevations of 0.78, a MAD of predicted from measured bed elevations of 0.0146 m, and a SDAD of 0.0134 m.

The differences between the measured and predicted bed elevations (i.e., predicted-measured) are presented in Figure 4.12. From this contour map it can be seen that the numerical model is predicting slightly higher bed elevations in the region of the point bar, and in the region of the outer bank scour hole. The model is predicting lower bed elevations in the center of the channel and downstream of the bend exit.

As with the 90° channel, detailed measurements of the velocity field were not taken during the laboratory experiments. For the 135° reference channel an average velocity of 0.283 m/s was recorded. The average magnitude of the predicted depth-averaged horizontal velocity vectors was 0.279 m/s.

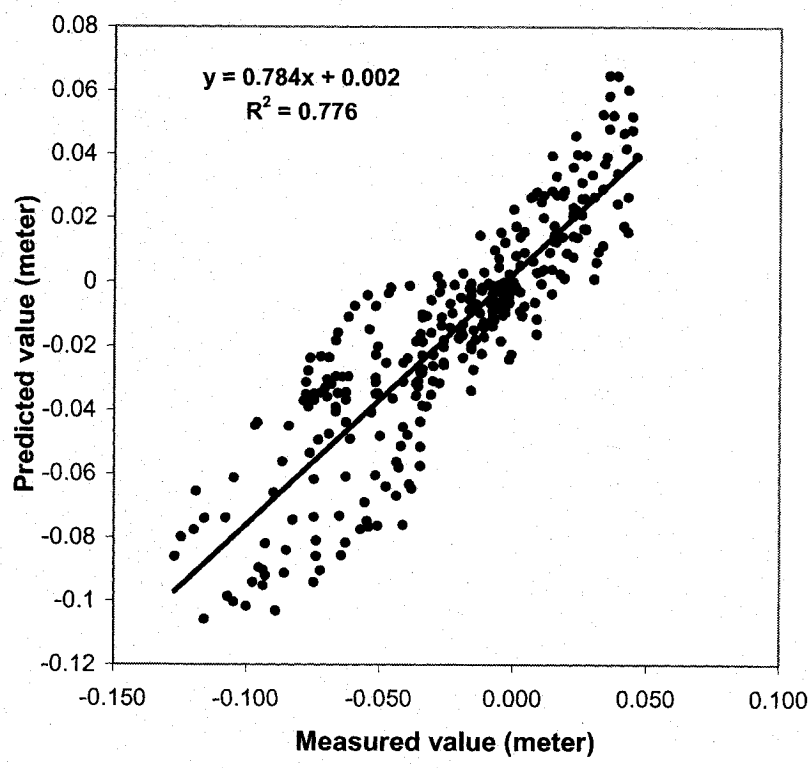

Figure 4.11 Predicted versus measured bed elevation for 135° reference channel

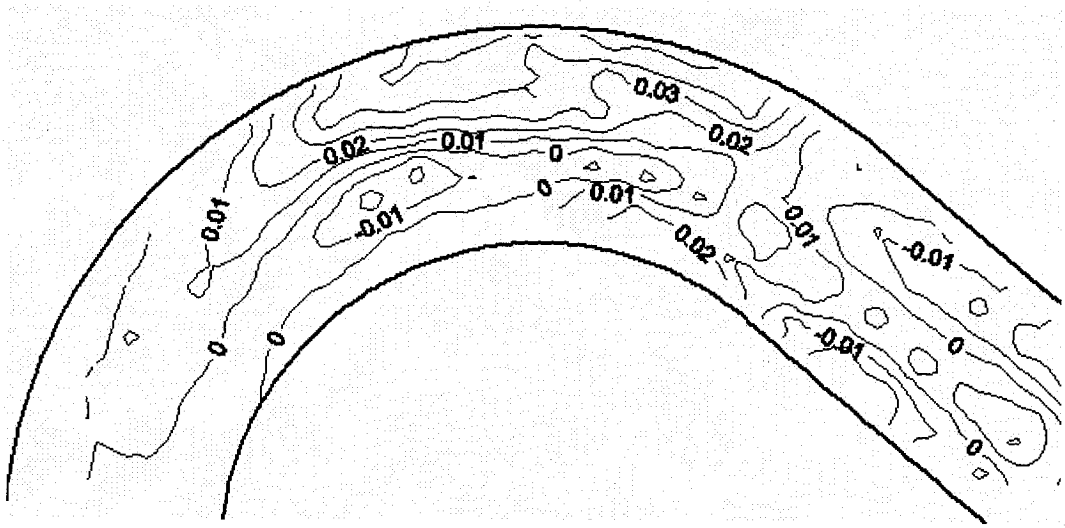

Figure 4.12 Measured bed elevations subtracted from predicted bed elevation for a 135° reference channel (m)

From Figure C.2, it can be seen that the numerical model predicted a maximum magnitude of 0.342 m/s and a minimum value of 0.138 m/s. It is observed that the maximum velocity is located along the center of the channel, 0.360 m after the bend exit.

The velocity vectors, located along the cross-section 0.300 m downstream of the bend exit are shown in Figure 4.13. As with Figure 4.3, this figure confirms the presence of secondary currents in the 135° channel. As previously discussed, the secondary flow cell is directed vertically down towards the toe of the outside bank and vertically up at the inner bank.

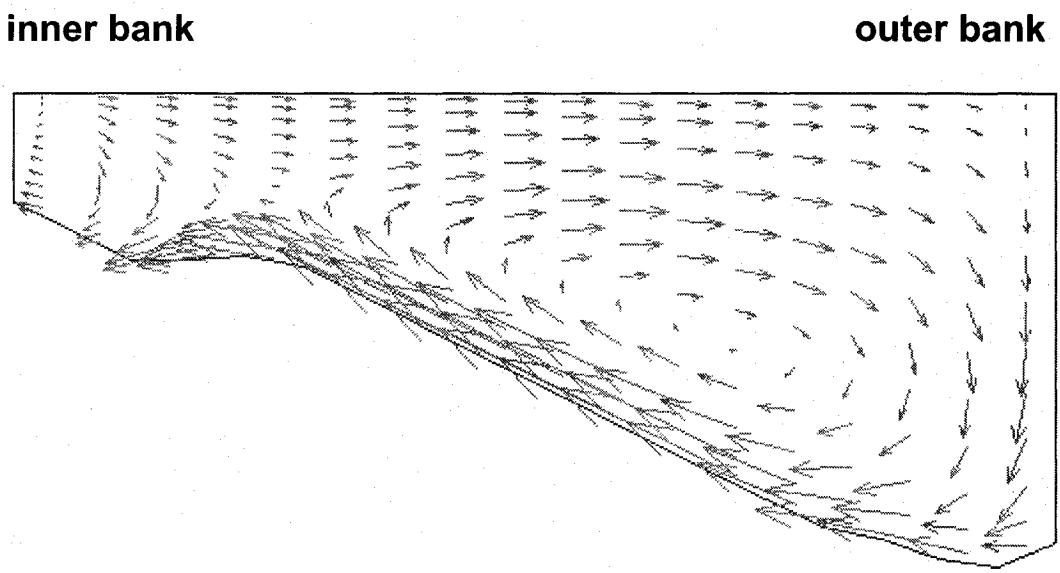

Figure 4.13 135° reference channel cross-section showing secondary currents 0.300 m downstream of bend exit

The shear stress distribution for the 135° reference channel is presented in Figure C.3. The values of bed shear stress range from 0.22 to 1.09 N/m^2. This shear stress distribution shows that the location of maximum shear stress corresponds to the location of maximum

scour and maximum velocity. Additionally, the minimum shear stress occurs in the same region as the point bar and the lowest depth-averaged horizontal velocity.

Although it is not possible to compare the flow field and bed shear stress data to measured values, it can be stated that the numerical model has successfully simulated the expected trends of flow, sediment deposition, and bed shear stress through the 135° channel bend. It was observed that both velocity and bed shear stress increased in the outer bank region. Conversely, a decrease of these parameters was observed along the inner bank. From Figure 4.13 it was possible to visualize the secondary currents through the channel bend. As anticipated, the secondary flow cell was directed vertically down towards the toe of the outside bank and vertically up along the inner bank. As a result of these trends, scouring was observed in the outer bank region and sediment was deposited along the inner bank.

4.2.2 135° Channel Containing Barbs

As a final phase of the numerical modeling, the sediment transport and flow were simulated through the 135° channel containing the barb groups listed in Table 3.7. It can be seen that the barb groups used for the 135° channel include five barbs. The predicted bed elevation contour maps, depth-averaged horizontal velocity maps, and bed shear stress distributions are presented in Appendix C.

4.2.2.1 135° Channel Containing Group-B ($\theta = 20°$)

The predicted bed elevation contour map for the 135° channel containing barb Group-B, with a barb alignment angle of 20°, is presented in Figure C.4. The corresponding depth-averaged velocity vector map and shear stress distribution are presented in Figures C.5 and C.6, respectively.

The measured bed elevation contour map, presented in Figure A.6, shows that with the addition of the barb group, the thalweg has shifted away from the outer bank. The location of the deepest measured scour holes are at the tip of the third barb in the group. The simulated bed elevation map, presented in Figure C.4, also shows that the thalweg has shifted away from the outer bank. However, the predicted location of the maximum scour hole is between the fourth and fifth barb in the group.

The measured bed elevation data is plotted versus the predicted bed elevation data in Figure 4.14. A linear regression line of the data gives an r^2 of 0.79. The MAD of predicted from measured bed elevations was found to be 0.0118 m. The SDAD was 0.0112 m.

The depth-averaged horizontal velocity vectors are presented in Figure C.5. It can be observed that, with the addition of barbs, the region of maximum velocity has shifted away from the outer bank. It is evident from this figure that the velocity gradient along the outer bank has been disrupted and that the velocity vectors are being redirected as they pass over the barbs.

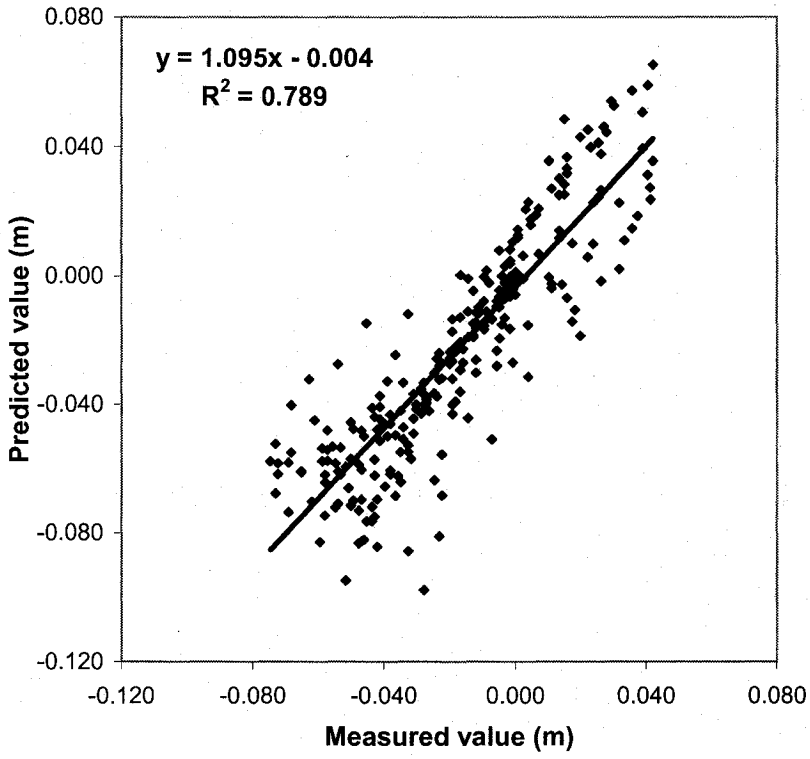

Figure 4.14 Predicted versus measured bed elevation for 135° channel (Group B, $\theta = 20°$)

The predicted bed shear stress distribution is presented in Figure C.6. It can be observed that the distribution of bed shear stress corresponds to the horizontal velocity profile and the sediment deposition. The higher bed shear stresses are located along the center of the channel and at the tips of the barbs, whereas the lower stresses are located along the inner bank and within the barb field.

4.2.2.2 135° Channel Containing Group-B ($\theta = 30°$)

As a result of the laboratory experiments the optimum barb arrangement for the 90° and the 135° channel bend was found to be Group B with a barb alignment angle of 30°. The predicted bed elevation contour map, depth-averaged velocity vector map, and shear

stress distribution for the 90° channel containing barb Group-B, with a 30° alignment angle, are presented in Figures C.7, C.8, and C.9, respectively.

The trends observed from this simulation were in close agreement with those observed with Group-B ($\theta = 20°$). The location of the deepest simulated scour hole, presented in Figure C.7, is between the fourth and fifth barb in the group. However, the deepest measured scour hole, shown in Figure A.7, is located between the second and third barb in the group. The difference between the measured and predicted bed elevations (i.e., predicted – measured) is presented in Figure 4.15. It can be observed from this figure that the numerical model is predicting higher bed elevations along the outer bank and in the barb field, and predicting lower bed elevations along the inner bank of the bend.

The measured bed elevation data is plotted versus the predicted bed elevation data in Figure 4.16. A linear regression line of the data gives an r^2 of 0.79. The MAD of predicted from measured bed elevations was found to be 0.0121 m. The SDAD was 0.0123 m.

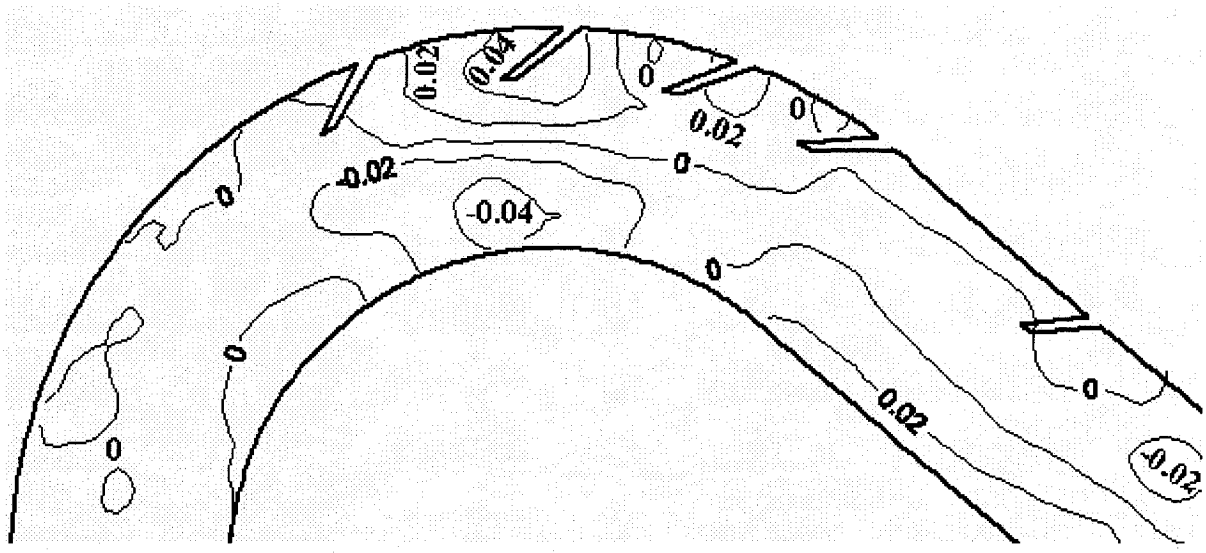

Figure 4.15 Measured bed elevation subtracted from predicted bed elevation for 135° channel in meters (Group B, $\theta = 30^{o}$)

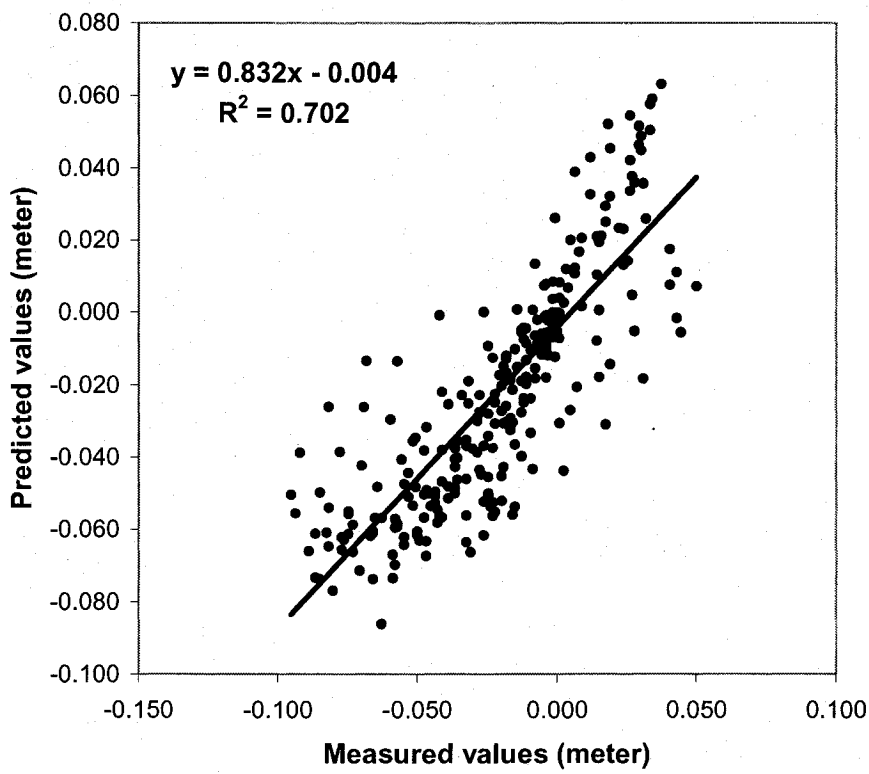

Figure 4.16 Predicted versus measured bed elevation for 135° channel (Group B, $\theta = 30^{o}$)

The depth-averaged horizontal velocity vector map and the bed shear stress distribution map are presented in Figures C.8 and C.9, respectively. Once again, it can be observed that the distribution of bed shear stress corresponds with to the horizontal velocity profile and the sediment deposition. The higher bed shear stresses are located along the center of the channel and at the tips of the barbs, whereas the lower stresses are located along the inner bank and within the barb field.

4.2.2.3 135° Channel Containing Group-B (θ = 40°)

The predicted bed elevation contour map for the 135° channel containing barb Group-B, with a 40° alignment angle, is presented in Figure C.10. The depth-averaged velocity vector map and shear stress distribution maps for this channel are shown in Figures C.11 and C.12, respectively. The measured bed elevation data are plotted versus the predicted bed elevation data in Figure 4.17.

Similar to the two previous barb groups (i.e., $\theta = 20^{\circ}$ and 30°), the maximum scour hole observed in Figure C.10 is located between the fourth and fifth barb. A linear regression line of the data gives an r^2 of 0.66. The MAD of predicted from measured bed elevations was found to be 0.0143 m. The SDAD was 0.0126 m.

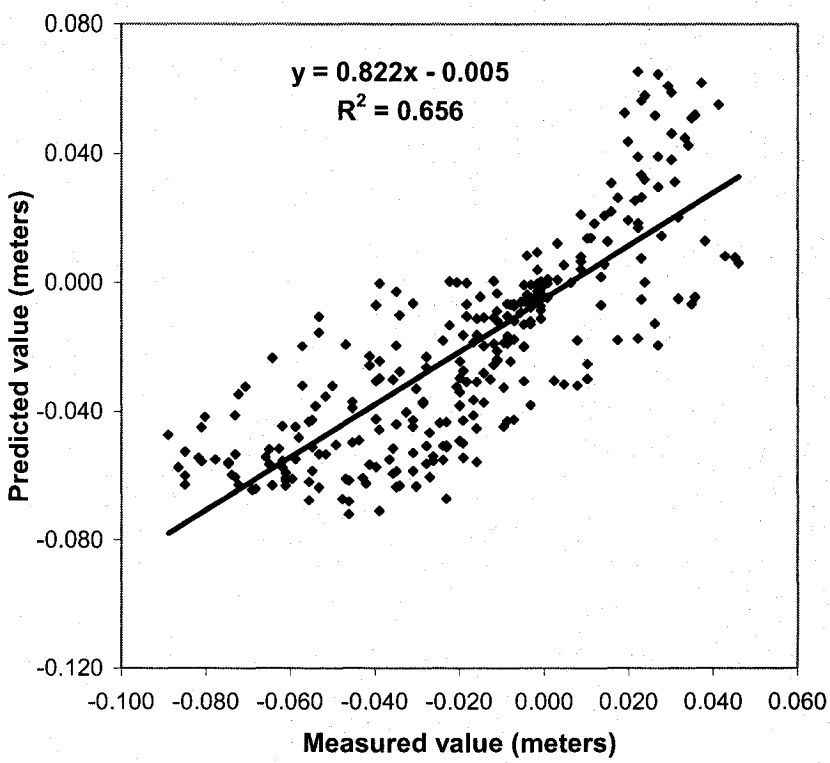

Figure 4.17 Predicted versus measured bed elevation for 135° channel (Group B, $\theta = 40°$)

Once again the depth-averaged horizontal velocity vector map and the bed shear stress distribution map, presented in Figures C.8 and C.9, show trends similar to the other barb groups for the 135° channel. From Figure C.8 it can be seen that the maximum velocity has shifted towards the center of the channel, and low velocity zones are located within the barb group and along the inner bank. The bed shear stress distribution shows a corresponding trend. The values of shear stress range from 0.04 N/m^2, along the inner bank, to 0.66 N/m^2. The maximum shear stresses are located along the center of the channel and at the barb tips, similar to the locations of greatest scour.

4.3 Percent Scour Reduction Comparison

Comparison of the laboratory results were performed based on the percent reduction in local scouring in the outer bank region. The percent reduction was calculated using Equation 3.1. As discussed in Section 3.1.2, the scour depths were measured at 0.0254 m from the outside wall of the channel within the regions of maximum scour. A similar analysis was performed with the predicted data. This analysis was performed to validate the numerical models capability to simulate the effects of different barb groups and barb alignment angles.

The measured and predicted percent scour for the 90° channel are plotted versus barb alignment angle in Figure 4.18. The numerical model predicts a higher percent scour reduction. Nevertheless, it is successful in simulating the effect that barb alignment angle has on the percent scour reduction. The measured and predicted percent scour for the 135° channel are plotted versus barb alignment angle in Figure 4.19. For the 135° channel the numerical model under-predicts the percent scour reduction. However, it also adequately simulates the effect of barb alignment angle on the percent scour reduction. Figure 4.20 illustrates the effect of Group-type on the percent reduction in scour for the 90° channel. The numerical over-predicts the percent scour reduction. However, the effect of Group-type on the percent reduction in scour is successfully simulated. It is noted that the Shields critical shear stress and Manning number differed for the simulation of the reference channel and the channel containing barbs for both the 90° and 135° channel. This inconsistency may contribute to the discrepancies observed between predicted and measured percent scour reduction.

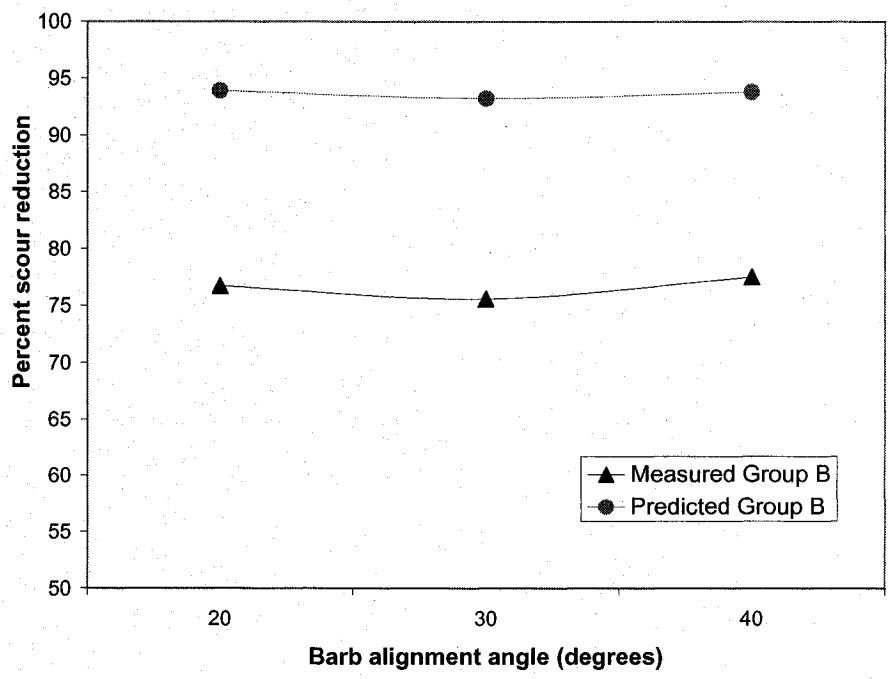

Figure 4.18 Percent scour reduction versus barb alignment angle for 90° channel

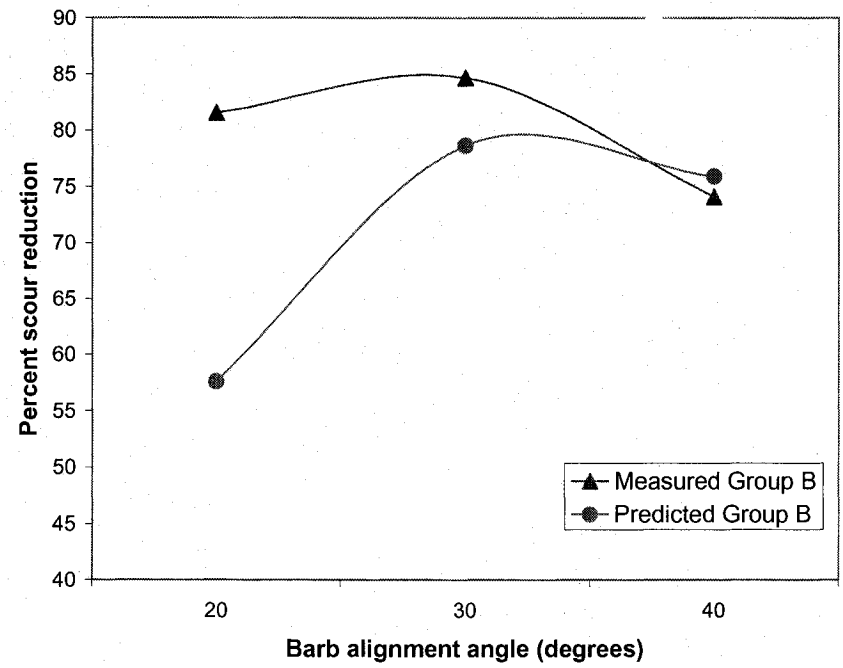

Figure 4.19 Percent scour reduction versus barb alignment angle for 135° channel

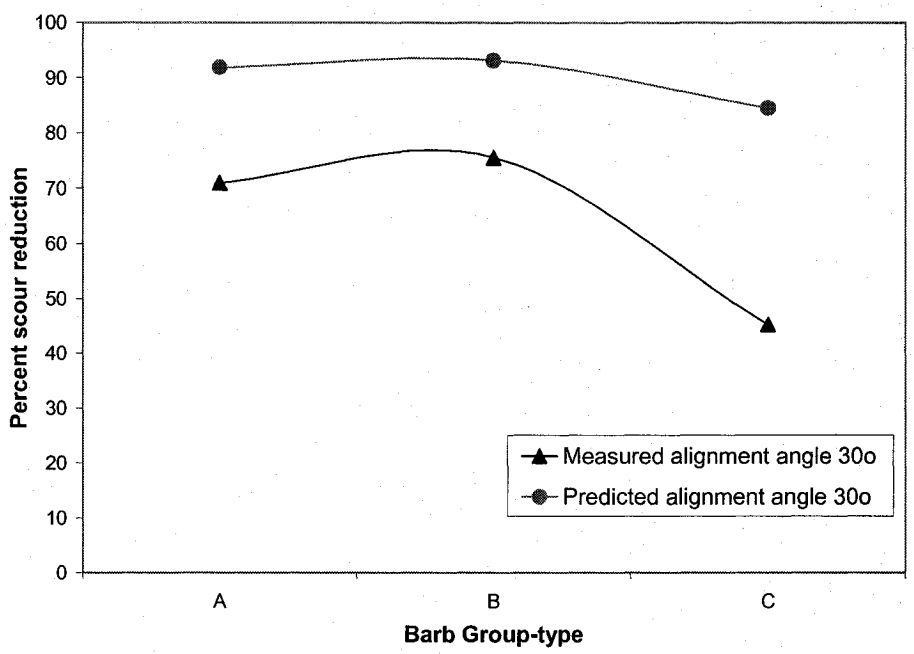

Figure 4.20 Percent scour reduction versus barb group-type for 90° channel

Nonetheless, the numerical model effectively simulated the effect of barb alignment angle and Group-type on the percent scour reduction in both the 90 and 135° channels. Comparable to the laboratory results, the numerical model results suggested that the 30° barb alignment angle and the Group-B barb arrangement resulted in the greatest amount of percent scour reduction in the outer bank region.

5.0 Discussion

Overall, the three-dimensional numerical model, SSIIM, was successful in simulating the patterns of sediment transport due to a series of barbs in both a 90 and 135° channel bends. Analyses of the depth-averaged velocity vectors and bed shear stress showed that the model predicted the expected trends. A statistical analysis, which compared the predicted bed elevations to the experimental data, validated the application of the model to moveable-bed bend sections of a hydraulically narrow channel containing barbs. A summary of the r^2, regression slope, MAD, and SDAD between predicted and measured bed elevations for the 90° channel simulations are presented in Table 5.1. Table 5.2 presents these values for the 135° channel.

Table 5.1 Summary of statistical analysis for 90° channel

Alignment angle, θ	Group-type	r^2	MAD (m)	SDAD (m)	Regression Slope
20	B	0.8	0.008	0.009	1.0
30	A	0.8	0.009	0.008	0.8
	B	0.8	0.008	0.007	0.8
	C	0.7	0.010	0.009	0.9
40	B	0.8	0.008	0.008	0.8

Table 5.2 Summary of statistical analysis for 135° channel

Alignment angle, θ	Group-type	r^2	MAD (m)	SDAD (m)	Regression Slope
20	B	0.8	0.012	0.011	1.1
30	B	0.8	0.012	0.012	0.8
40	B	0.7	0.014	0.013	0.8

It can be seen from Table 5.1 that, in general, the predicted bed elevations for the 90° channel are in good agreement with the experimental data. The MAD for the 90° channel

simulations were between 23 and 30% of the maximum measured scour. Therefore, the model accuracy for the 90° channel simulations could be considered to be within 23 to 30%. The r^2 values and the regression slopes are close to 1, indicating that the model has successfully predicted the patterns of sediment erosion and deposition through the 90 and 135° channel bends. It is observed that the predicted bed elevations for Group-B (θ=20°) agree the best with the experimental bed elevations. The statistics listed in Table 5.2 indicate that the numerical model was also able to predict favorable bed elevations for the 135° channel. However, the bed elevations generated with a 40° alignment angle have the lowest r^2 value. It can also be noted that the MAD and SDAD are higher for the 135° channel bend, indicating lower accuracy. The MAD for the 135° channel ranged from 24 to 31% of the maximum predicted scour. Therefore, the model accuracy for the 135° channel simulations could be considered to be within 24 to 31%.

The difference between the measured and predicted bed elevations for the 90° channel without barbs was presented in Figure 4.2. This figure suggested that the numerical model was over-estimating erosion in the outer bank region and, to a lesser degree, over-estimating deposition in the near-bank region. In addition, the regression slope for the predicted versus measured bed elevations for the 90° reference channel was 1.2. A slope greater than 1.0 indicates that the numerical model is overestimating the scour and deposition.

The bed elevation difference map for the 90° channel containing Group-B (θ = 30°), presented in Figure 4.6, indicated that the numerical model was predicting slightly higher

bed elevations in both the region of the point bar and in the vicinity of the barbs. However, the regression slope for the predicted versus measured bed elevations was 0.80. A regression slope less than 1.0 suggests that the numerical model is underestimating the scour and deposition. Upon closer examination of the regression analysis in Figure 4.7, it is observed that the linear regression trend line does not fit the data properly. It is evident that the regression line has a smaller slope than the data. This is due to limitations of the regression analysis. Linear regression assumes all error is in the y-variable.

There are several possible reasons for the discrepancies between the predicted and measured bed elevations. The model had several limitations that affected the accuracy of the results. The numerical model used a rigid lid, which did not allow for the water surface to vary in the transverse direction. Due to this, superelevation of the water surface did not occur along the outer bank through the channel bend. This is an important flow feature, especially for the development of the secondary currents through a channel bend. In addition to this, a hydraulically narrow channel was simulated. This could also affect the numerical model's ability to correctly simulate secondary currents and turbulence through the channel. These are complex flow fields and the three-dimensional Reynolds-averaged Navier-Stokes equations can not fully replicate secondary currents, particularly in narrow channels, due to turbulence closure.

The geometry of the barbs was also limited by the model. The width of the barbs was restricted by the grid size and, as a result, the barbs in the numerical model were wider than those used in the laboratory experiments. Furthermore, the sides of the barbs were

not smooth, due to the grid. This also prevented the barbs from sloping smoothly away from the outer bank. Instead, their elevation decreased in steps. In the case of the 135° channel, it was not possible to account for the slope. This could account for the higher MAD and SDAD values for the 135° channel.

Visual observation of the bed elevation contour maps showed that the locations of the predicted maximum and minimum bed elevations were slightly different than the locations of the measured maximum and minimum bed elevations. This spatial inconsistency would have contributed to discrepancies between the predicted and measured bed elevations.

It order to compensate for the inconsistencies between the geometries of the laboratory and numerically modeled barbs, it was necessary to adjust other input parameters. Specifically, these parameters were the Shields parameter and the Mannings number. Therefore, it can be seen (Tables 3.3, 3.6, and 3.8) that the input parameters differ between the reference channels and the channels containing barbs. However, it is noted that the parameters remain constant for all barb arrangements within the 90° channel. Similarly, the parameters remain constant for all barb arrangements within the 135° channel. This was necessary in order to correctly compare the different barb group-types and alignment angles within the 90 and the 135° channels, respectively. It was noted that the bed entrainability in the 135° channel was lower than in the 90° channel. In order to achieve predicted bed elevations comparable to the measured bed elevations it was necessary to use a lower Shields parameter. This could be due to differences in the barb

geometries between the 90 and 135° channels (e.g., the barbs in the 135° channel did not slope away from the bank). However, this inconsistency was also observed between the 90 and 135° reference channels. It is also possible that the shear stress predicted by the numerical model was more exaggerated in the tight 90° channel. Therefore, the Shields parameter was set higher in the 90° channel to reduce the bed entrainability.

In Section 4.3 a comparison was performed to determine the effect of Group-type and barb alignment angle on the percent reduction in scour. This analysis was performed to validate the numerical model's capability to simulate the effects of different barb groups and barb alignment angles. It was found that the numerical model successfully simulated the effect of barb alignment angle and Group-type on the percent scour reduction in both the 90 and 135° channels. However, for the 90° channel the predicted percent scour reduction values were consistently higher than the measured values. On the other hand the predicted percent scour reduction values for the 135° channel were lower than the measured values. It is suggested that these discrepancies are due to the difference in the input parameters (i.e., Shields parameter and Manning number) used for the reference channel and the channels containing barbs. Nonetheless, the effect of Group-type and barb alignment angle on the percent scour reduction was comparable to the laboratory results. The numerical model results suggested that the 30° barb alignment angle and the Group-B barb arrangement resulted in the greatest amount of percent scour reduction in the outer bank region.

It is also feasible that the experimental data contributed to the differences between the predicted and measured data. Two important input parameters were discharge and water

depth. The values that were recorded in the laboratory were used for the numerical modeling. However, the accuracy of the measured values will be limited by the precision of the measurement instruments, and human error. The accuracy of the measured bed elevations, used for calibration and comparison, are also limited by the precision of the measurement instruments, and human error. In addition to this, there was a discrepancy in the amount of data predicted by the numerical model, and the amount of measured data available for comparison. The numerical model produced significantly more data points than were collected in the laboratory (i.e., 26 568 predicted data points versus 252 measure data points for the 90° channel). Due to time and physical restraints, this is expected. However, more measured bed elevation points would have provided a more representative profile of the bed, and possibly decreased differences between the measured and predicted data. Another possible source of error due to time constraints was the decision to run the model barb tests for 5 h instead of running it until the equilibrium condition was reached. As a result, it is possible that full equilibrium may not have been reached when the bed elevations were measured.

Detailed measurements of the velocity field were not taken during the laboratory experiments. Nevertheless, the predicted depth-averaged horizontal velocities were analyzed for each model simulation to observe trends in the data. It was observed that, with the addition of a barb group, the region of maximum velocity shifted away from the outer bank towards the center of the channel. The velocity gradient along the outer bank was disrupted, and this became a low-velocity region. In several of the figures, such as Figure B.14, it is possible to see the direction of the velocity vectors being redirected as

the flow passes over a barb. Analysis of the velocity vectors in profile view (e.g., Figures 4.3 and 4.8) confirmed the presence of secondary currents within the channel. It was noted that, due to the rigid lid, superelevation of the water surface did not occur and, thus, the formation of the outer bank cell was not observed. However, the secondary flow cell was successfully simulated. In the reference channel the velocity vectors were directed vertically down at the outer bank, and vertically up at the inner bank. In the channel containing barbs the velocity vectors were directed vertically down at the tip of the barb.

As further validation that the appropriate trends were being simulated, the bed shear stress distribution was examined. It was noted that the maximum bed shear stresses occurred in the same regions as the maximum scour and velocity. In general, the lowest bed shear stress was located within the barb field and along the inner bank. The highest stresses occurred along the center of the channel and at the tips of the barbs.

6.0 Conclusions and Recommendations

It is concluded that the three-dimensional numerical model, SSIIM, was successful in simulating the turbulent flow field and associated scour and deposition due to a series of barbs in both a 90 and 135° channel bend. Statistical analysis of predicted bed elevation data showed good agreement with the measured data. The r^2 values and the regression slopes for both the 90 and 135° channels were close to 1, indicating that the model successfully predicted the patterns of sediment erosion and deposition through the 90 and 135° channel bends. Statistical analysis of the sediment transport results for the 90° channel bend found an average regression coefficient of determination of predicted from measured bed elevations of 0.8 for the channels containing the various barb arrangements. An average regression coefficient of determination of 0.8 was observed for the 135° channel. Any inaccuracies in the results are attributed to the following: limitations of the Reynolds-averaged Navier Stokes equations; geometrical differences between the laboratory and simulated barbs; spatial inconsistencies between simulated and predicted bed elevations; and the limited amount of measured bed elevations from the laboratory study.

The effects of various barb groups and barb alignment angles were analyzed. The effectiveness of the barb arrangements was judged by the percent reduction in scour. From this analysis it was observed that the data from the numerical model predicted the same trends that were observed from the laboratory data. It was found that Group-B, with an alignment angle of 30° provided the best protection against scouring in the outer bank region.

Although it was not possible to compare to measured data, it was found that the predicted depth-averaged velocity vector data followed the expected trends. With the addition of a barb group, the region of maximum velocity shifted away from the outer bank towards the center of the channel. The velocity gradient along the outer bank was disrupted, and this became a low-velocity region. In addition, the velocity vector passing over the barbs were redirected away from the outer bank. It was concluded that the numerical model successfully simulated the relation of the flow field to associated scour and deposition in a complex flow field. It was observed that maximum bed shear stresses occurred in the same regions as the maximum scour and velocity. And conversely, the minimum bed shear stress occurred in the regions of minimum scour and velocity. Nevertheless, it is recommended that flow field measurements be performed in the laboratory. Such a data set is necessary to validate that the simulated flow field is accurate.

It is suggested that further studies would be beneficial to the current design guidelines. Based on the favorable results presented in this thesis, it is recommended that SSIIM be used to expand the data set for the 90^{o} channel. This would include analyzing the effect of a larger variety of barb groups and alignment angles on the percent reduction in scour. Therefore, the resulting optimum barb arrangement would be based on a much larger data set. However, due to the limitations of SSIIM, it is suggested that only groups containing a maximum of three barbs be simulated.

It is also suggested that SSIIM be used to simulate the sediment transport and velocity field through a channel containing barbs that is more representative of a natural channel.

Therefore, the numerical model should simulate a wide channel, with live-bed conditions, and a trapezoidal cross-section. Furthermore, a larger range of channel bend angles should be assessed. An analysis of different flow depths would contribute to the understanding of the performance of barbs during low flow and high flow conditions. Laboratory tests should be run in combination with numerical testing to provide calibration data.

While it was found that SSIIM was successful in simulating the flow field and associated bed transport, it is recommended that numerical simulations be tested with a three-dimensional model that can properly replicate the barb geometry. Further testing on the effect of barb height, width, and slope would be possible with a numerical model such as this. Furthermore, it is suggested that a three-dimensional numerical model that computes the free water surface be used for these simulations.

In conclusion, the following objectives were achieved in this thesis:

- The application of a three-dimensional-numerical model, SSIIM, to moveable-bed bend sections of a hydraulically narrow rectangular channel containing barbs was validated;
- The effects of different arrangements of barb groups in the bend section were successfully simulated; and
- The data were analyzed to determine the relation of the flow field to associated scour and deposition in a complex fluvial environment.

These novel data, which encompass both the sediment transport and the flow field, contribute to the understanding and analyses of the bank protection capabilities of barbs.

7.0 References

ASCE Task Committee on Hydraulics, Bank Mechanics, and Modeling of River Width Adjustment. (1998). "River width adjustment I: Processes and mechanisms". *J. Hydraulic Eng.*, 124(9), 881-902.

Bates, D.B., Lane, S.N., and Ferguson, R.I. (2005). *Computational Fluid Dynamics*, John Wiley and Sons, Ltd, Chichester, West Sussex, England.

Bernard, P.S. (2002). *Turbulent Flow,* John Wiley and Sons, Inc., Hoboken, New Jersey.

Boussinesq, J. (1877). "Theorie de l'écoulement tourbillant". *Mem. Pres. Acad. Sci.* XXIII, 46, Paris.

Daugherty, R. L., Franzini, J. B., and Finnemore, E. J. (1985). *Fluid Mechanics with Engineering Applications, Eighth Edition*, McGraw-Hill Book Company, New York.

Derrick, D. L. (1997). "Harland Creek Bank Stabilization Demonstration Project". *Land and Water*, 41(5), 22-25.

Dietrich, W. E. (1987). "Mechanics of flow and sediment transport in river bends." River channels: environment and process, K. S. Richards, ed., Blackwell, Oxford, 179-227.

Gomez, B. and Church, M. (1989). "An assessment of bed load sediment transport formulae for gravel bed rivers". *WRR*, 25(6), 1161-1186.

Habersack, H.M. and Laronne, J.B. (2002). "Evaluation and improvement of bed load discharge formulas based on Helley-Smith sampling in an alpine gravel bed river". *J. Hydraulic Eng.*, 128(5), 484-499.

Jia, Y., Scott, S., Xu, Y., Huang, S., and Wang, S.S.Y. (2005). "Three-dimensional numerical simulation and analysis of flows around a submerged weir in a channel bendway". *J. Hydraulic Eng.*, 131(8), 682-693.

Jones, W.P. and Launder, B.E. (1972). "The prediction of laminarization with a two-equation model of turbulence". *Int. J. Heat Mass Transfer*, 15, 301-314.

Kay, M. (1998). *Practical Hydraulics*, E&FN SPON, London.

Knighton, D. (1998). *Fluvial Forms and Processes*, Oxford University Press, Inc., New York.

Kovacs, A. and Parker, G. (1994). "A new vectorial bedload formulation and its application in the time evolution of straight rivers". *J. Fluid Mech.*, 267, 153-183.

Kuhnle, R.A., Alonso, C.V., and Shields, F.D.Jr. (1999). "Geometry of scour holes associated with 90° spur dikes". *J. Hydraulic Eng.,* 125(9), 972-978.

Kuhnle, R.A., Alonso, C.V., and Shields, F.D.Jr. (2002). "Local scour associated with angled spur dikes". *J. Hydraulic Eng.,* 128(12), 1087-1093.

Launder, B.E. and Spalding, D.B. (1973). "The numerical computation of turbulent flow". *Computer Methods in Applied Mechanics and Engineering*, 3, 269-289.

Markham, A.J. and Thorne, C.R. (1992) "Geomorphology of gravel bed river bends", in Billi, Hey, Thorne and Tacconi (eds), *Dynamics of gravel bed rivers,* Wiley, 433-456.

Matsuura, T. (2004). *Stream-bank Protection in Narrow Channel Bends Using 'Barbs' – A Laboratory Study*, M.A.Sc. Thesis, Department of Civil Engineering, University of Ottawa.

Matsuura, T. and Townsend, R. (2004). "Stream-barb installations for narrow channel bends - a laboratory study". *Canadian Journal of Civil Engineering.* 31(3), 478-486.

Melaaen, M.C. (1992). "Calculation of fluid flows with staggered and nonstaggered curvilinear nonorthogonal grids – the theory", *Numerical Heat Transfer*, Part B, 21, 1-19.

Nagata, N., Hosoda, T., Nakato, T., and Muramoto, Y. (2005). "Three-dimensional numerical model for flow and bed deformation around river hydraulic structures", *J. Hydraulic Eng.,* 131(12), 1074-1087.

Nezu, I., Tominaga, A., and Nakagawa, H. (1993). "Field measurements of secondary currents in straight rivers." *J. Hydraulic Eng.,* 119(5), 598-614.

Olsen, N.R.B. (1991). *A numerical model for simulation of sediment movements in water intakes,* Dr. Ing. Dissertation, The Norwegian Institute of Technology, Trondheim.

Olsen, N.R.B. (2004). *A Three-Dimensional Numerical Model for Simulation of Sediment Movements in Water Intakes with Multiblock Option: User's Manual.* Department of Hydraulic and Environmental Engineering, Norwegian University of Science and Technology, Trondheim, Norway.

Oreskes, N. and Belitz,K., 2001. "*Philosophical issues in model assessment*". In Model Validation: Perspectives in Hydrological Science, Anderson, M.G. and Bates, P.D. (eds), chichester: John Wiley and Sons, 23-41.

Ouillon, S. and Dartus, D. (1997). Three-dimensional computation of flow around groyne. *J. Hydraulic Eng.,* 123(11), 962-970.

Patankar, S.V. (1980). *Numerical Heat Transfer and Fluid Flow*, McGraw-Hill, New York.

Petersen, M.S. (1986). *River Engineering, Prentice-Hall*, Englewood Cliffs, New Jersey.

Przedwojski, B. (1995). "Bed topography and local scour in rivers with banks protected by groynes". *J. Hydraulic Research*, 33(2), 257-273.

Przedworjski, B and Blazejewski, R. (1995). *River Training Techniques*, A.A. Balkema, Rotterdam Netherlands.

Raudkivi, A.J. (1998). *Loose Boundary Hydraulics*, A.A. Balkema, Rotterdam Netherlands, Brookfield VT.

Reynolds, O. (1895). "On the dynamical theory of incompressible viscous fluids and the determination of the criterion". *Philosophical Transactions of the Royal Society of London A*, 186, 123-164.

Rodi, W. (2000). *Turbulence Models and Their Application in Hydraulics*, Third Edition, A.A. Balkema, Rotterdam Netherlands, Brookfield VT.

Schlichting, H. (1979). *Boundary Layer Theory*, McGraw-Hill, New York.

Shields, A. (1936). "Anwendung der Ähnlichkeitsmechanik und der Turbulenzforschung auf die Geschiebebewegung". *Mitteilungen der Preußischen Versuchsanstalt für Wasserbau und Schiffbau,* 26:26. (German).

Shields, F. D., Knight, S. S., and Cooper, C. M. (1998). "Addition of spurs to stone toe protection for warmwater fish habitat rehabilitation," *J. American Water Res. Ass.*, 34, 1427-1436.

Simons, D.B. and Sentürk, F. (1992). *Sediment Transport Technology*, Water Resources Publications, Littleton, CO.

Sukhodolov, A., Uijttewaal, S.J., and Engelhard, C. (2002). "On the correspondence between morphological and hydrodynamic patterns of groyne fields". *Earth Surface Processes and Landforms.* 27, 289-305.

Sukhodolov, A., Engelhardt, C., Kruger, and A., Bungartz, H. (2004). "Case study: turbulent flow and sediment distributions in a groyne field". *J. Hydraulic Eng.,* 130(1), 1-9.

Tingsanchali, T. and Maherswaran, S. (1990). "2-D depth averaged flow computation near groyne". *J. Hydraulic Eng.,* 116(1), 71-86.

Uijttewaal, S.J., Lehmann, D., and van Mazijk, A. (2001). "Exchange processes between a river and its groyne fields: model experiments". *J. of Hydraulic Research.* 127(11), 928-936.

USDA. (1996). *Engineering Field Handbook, Chapter 16*. U.S. Department of Agriculture, Natural Resources Conservation Service.

USDA. (1999). *Technical Note 23: Design of Stream Barbs*. U.S. Department of Agriculture, Natural Resources Conservation Service, Portland, Oregon.

USDA. (2001). *Techical Note 12: Design of Stream Barbs*. U.S. Department of Agriculture, Natural Resources Conservation Service, Boise, Idaho.

USDA. (2005). *Technical Note 23: Design of Stream Barbs*. U.S. Department of Agriculture, Natural Resources Conservation Service, Portland, Oregon.

USACOE. (1998) *Fact Sheet: Bendway Weir History, Theory, and Design*. U.S. Army Corps of Engineers, Waterways Experiment Station. Vicksburg, MS.

van Rijn, L.C.(1948). "Sediment transport, Part I: bed load transport". *J.Hydraulic Eng.*, 110 (10),1431-1456.

van Rijn, L.C. (1984). "Sediment transport. Part II: suspended load transport." *J. Hydraulic Eng.*, 110(11), 1613-1641.

APPENDIX A
Measured Bed Elevation Contour Maps for 90° and 135° Channels

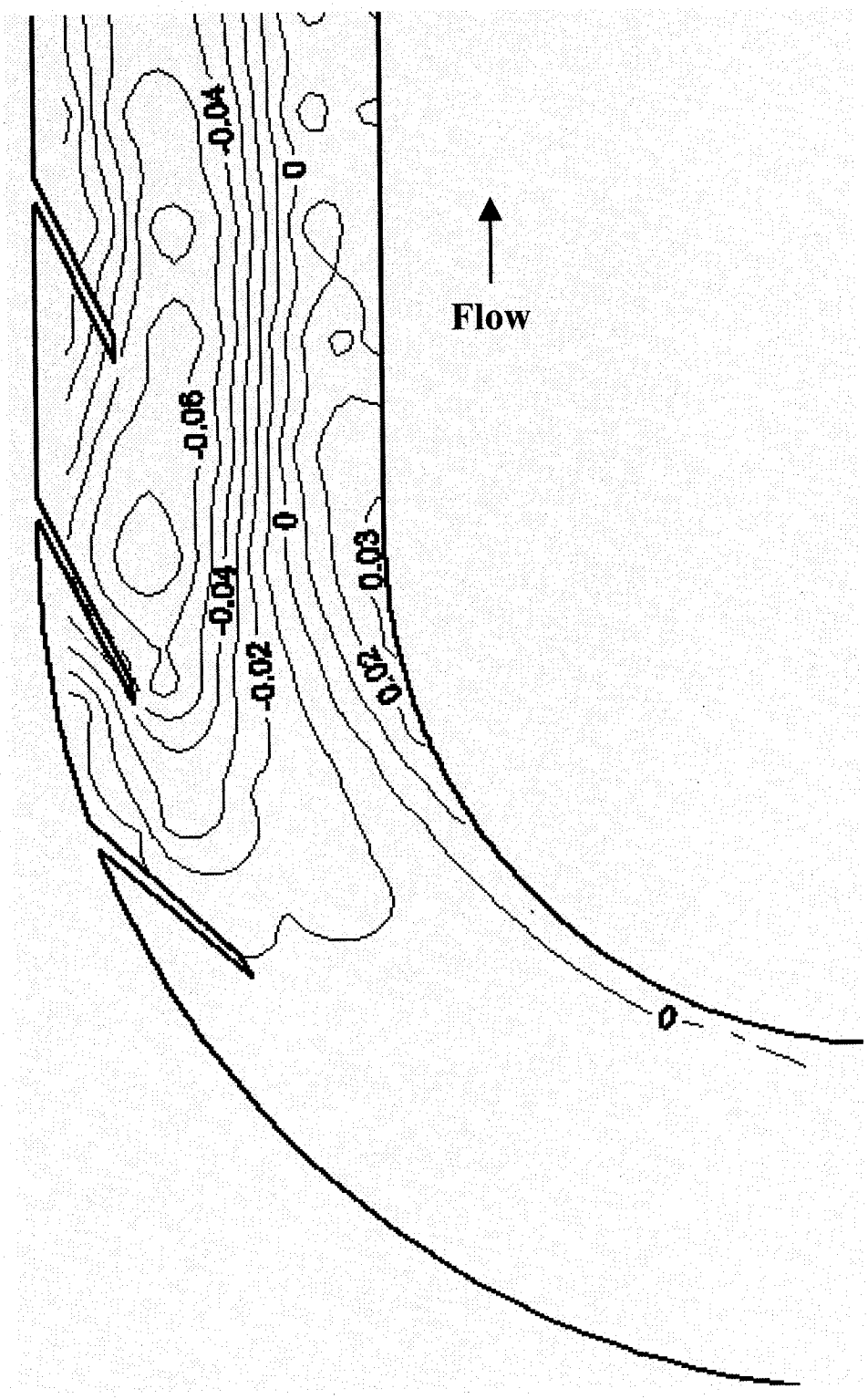

Figure A.1 Measured bed elevation contour map: 90° channel, Group B, $\theta = 20^{\circ}$ (m)

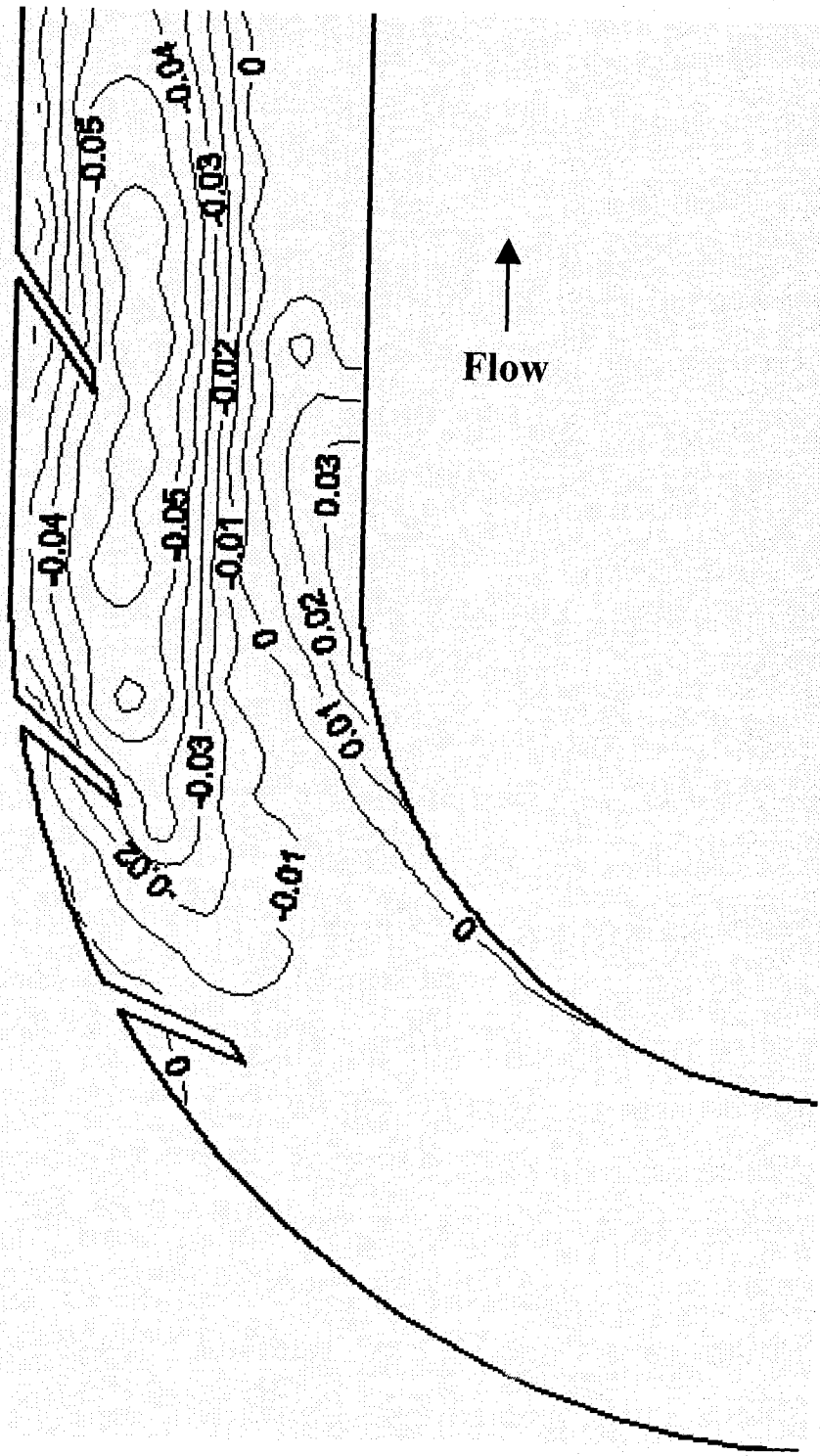

Figure A.2 Measured bed elevation contour map: 90° channel, Group A, $\theta = 30°$ (m)

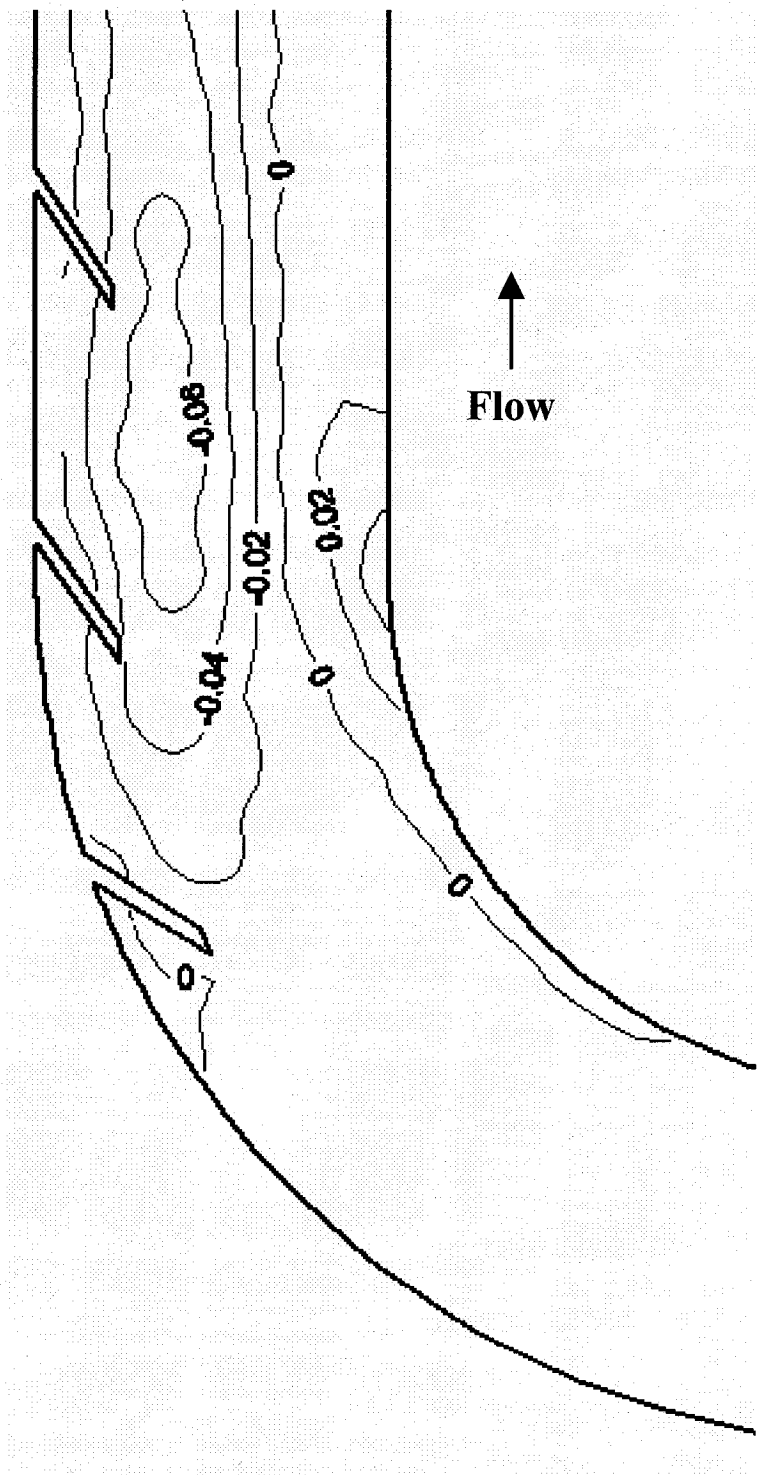

Figure A.3 Measured bed elevation contour map: 90° channel, Group B, $\theta = 30^{o}$ (m)

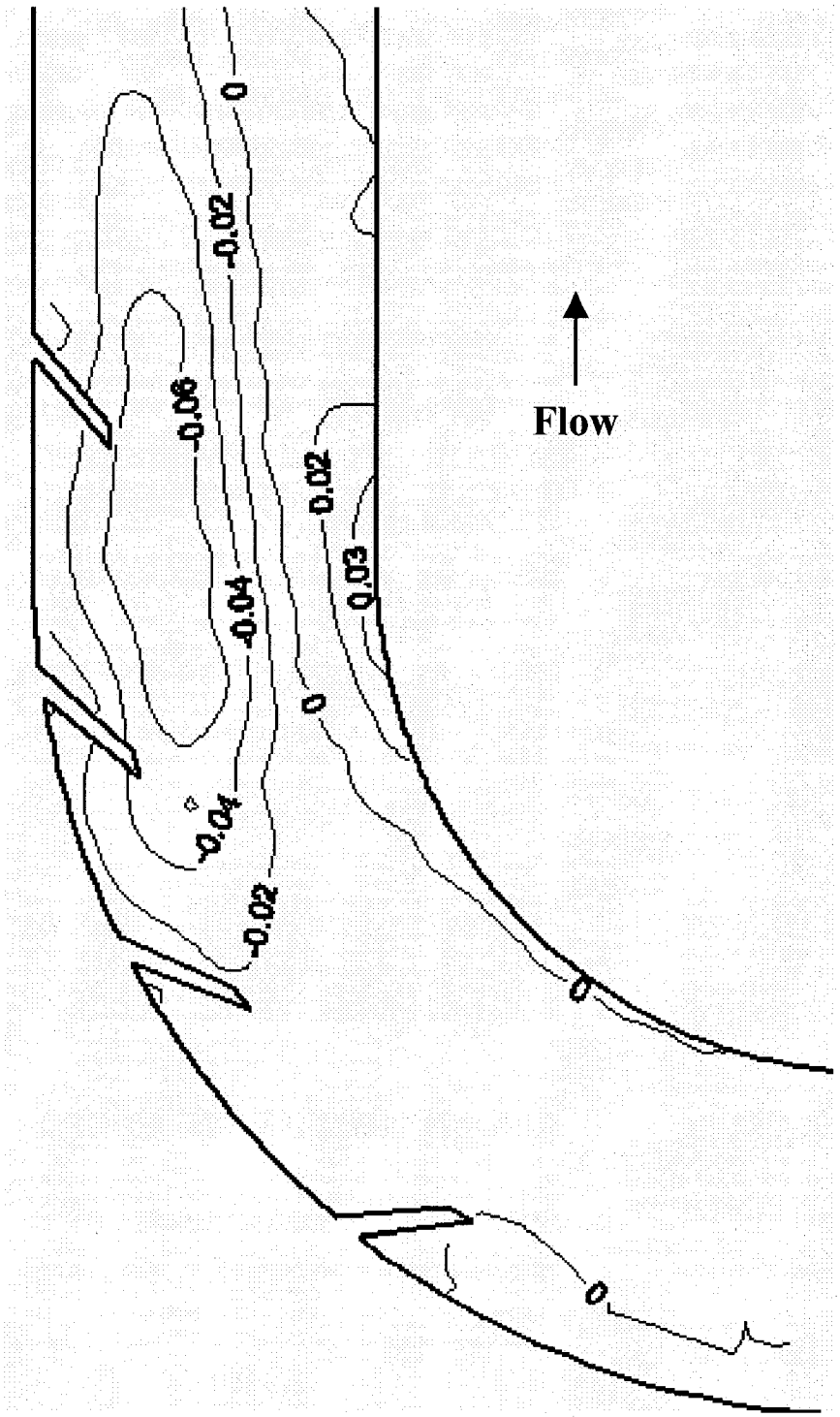

Figure A.4 Measured bed elevation contour map: 90° channel, Group C, $\theta = 30°$ (m)

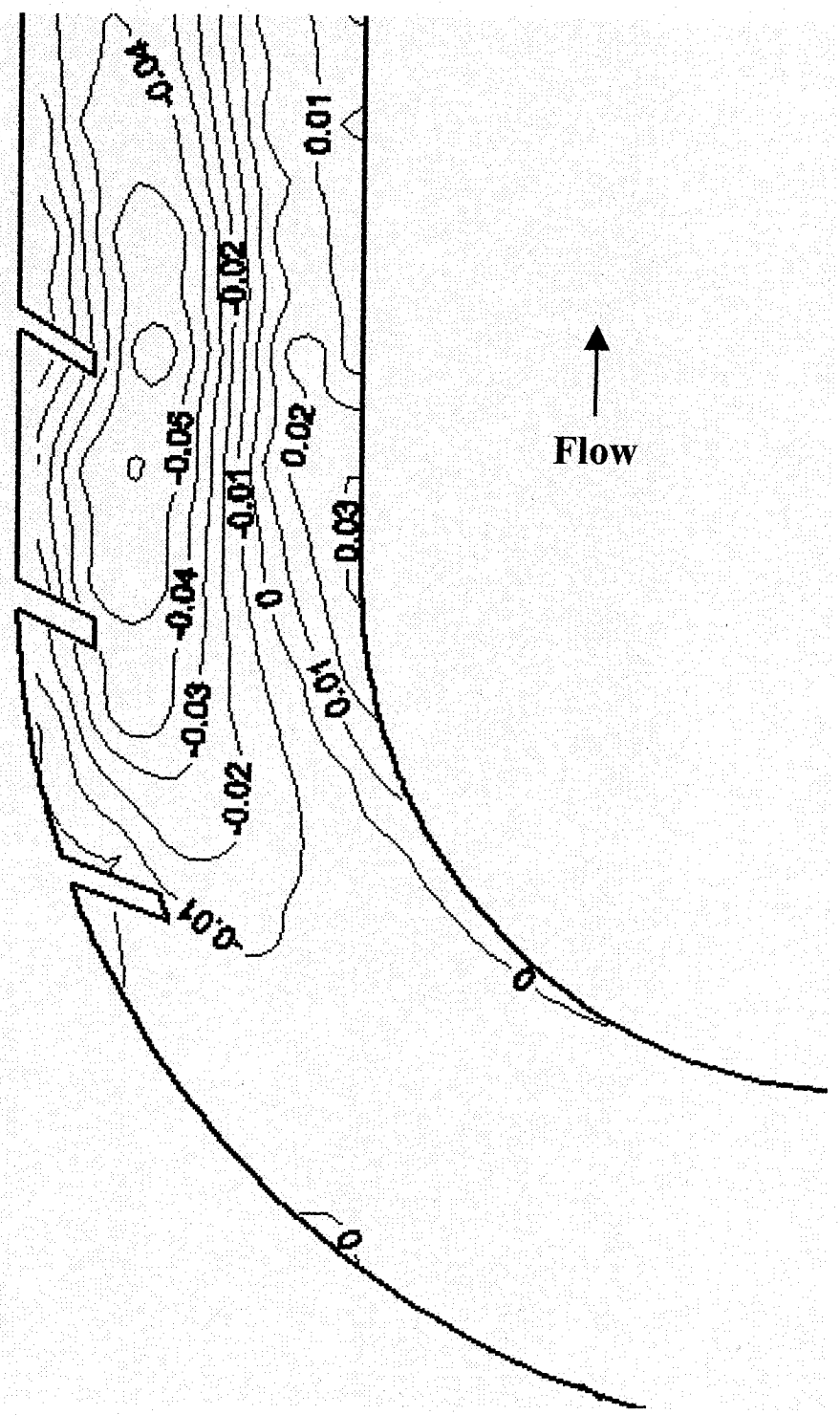

Figure A.5 Measured bed elevation contour map: 90° channel, Group B, $\theta = 40°$ (m)

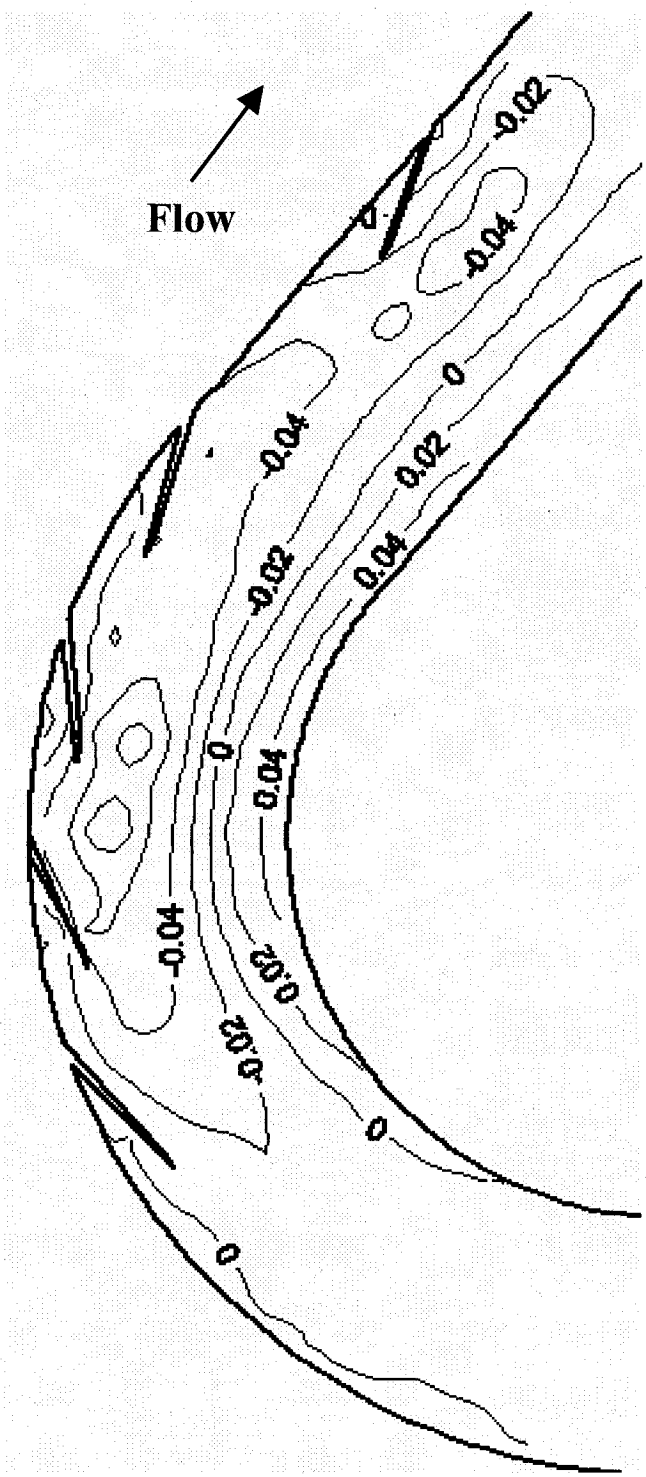

Figure A.6 Measured bed elevation contour map: 135° channel, Group B, $\theta = 20^{o}$ (m)

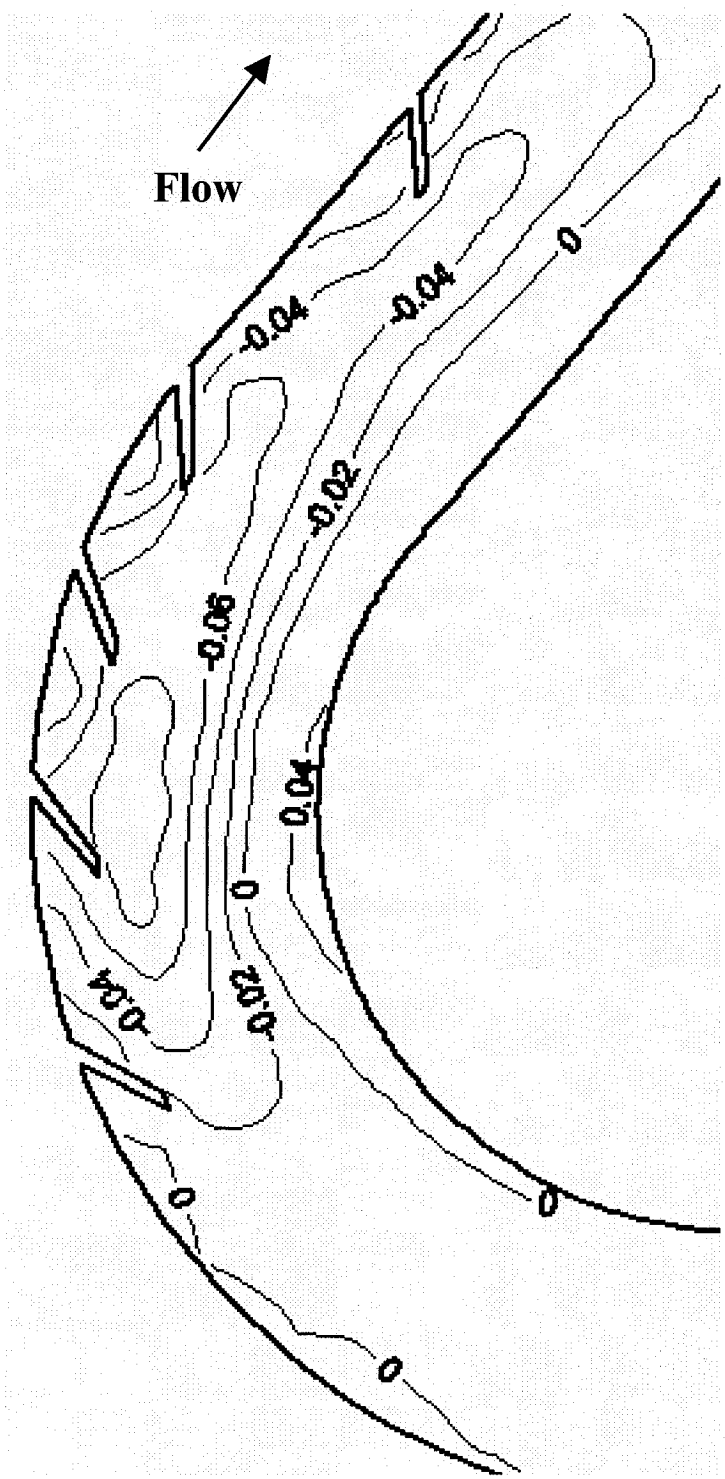

Figure A.7 Measured bed elevation contour map: 135° channel, Group B, θ = 30° (m)

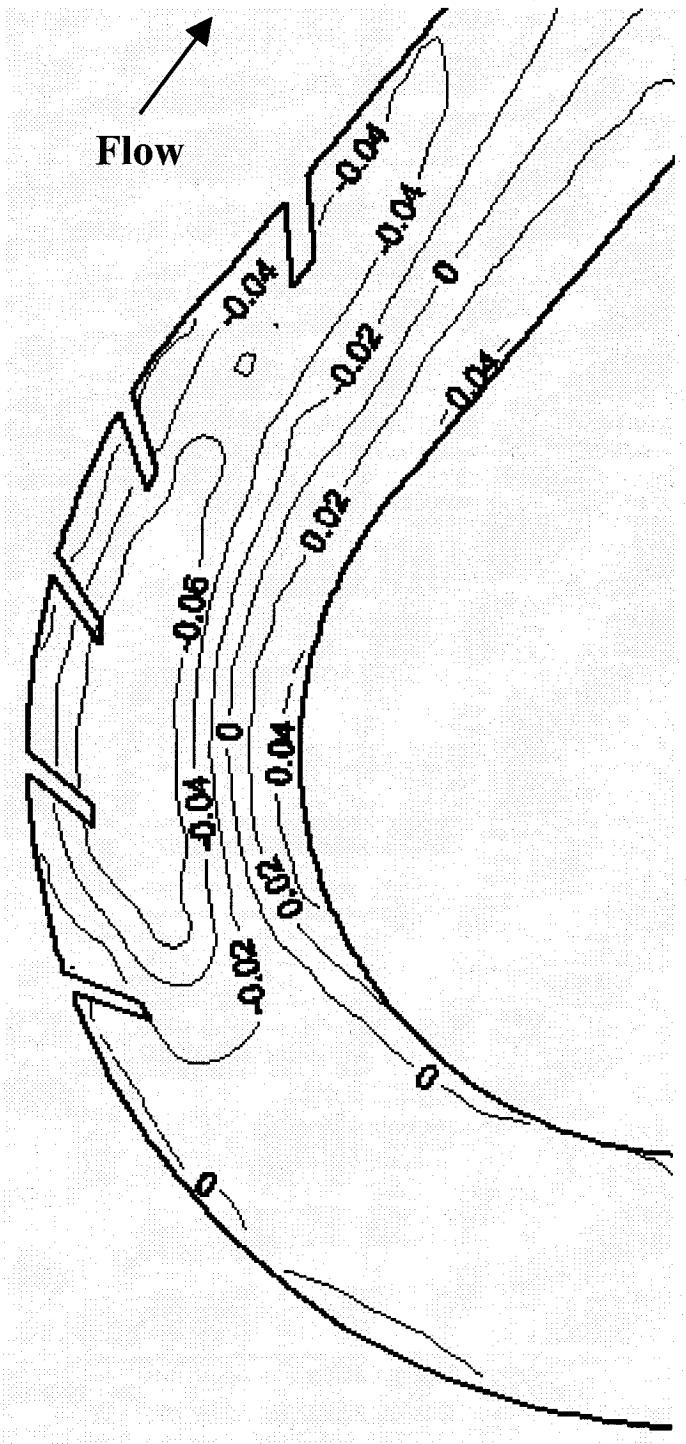

Figure A.8 Measured bed elevation contour map: 135° channel, Group B, $\theta = 40^{o}$ (m)

APPENDIX B
Three-Dimensional Numerical Model Results for 90° Channel

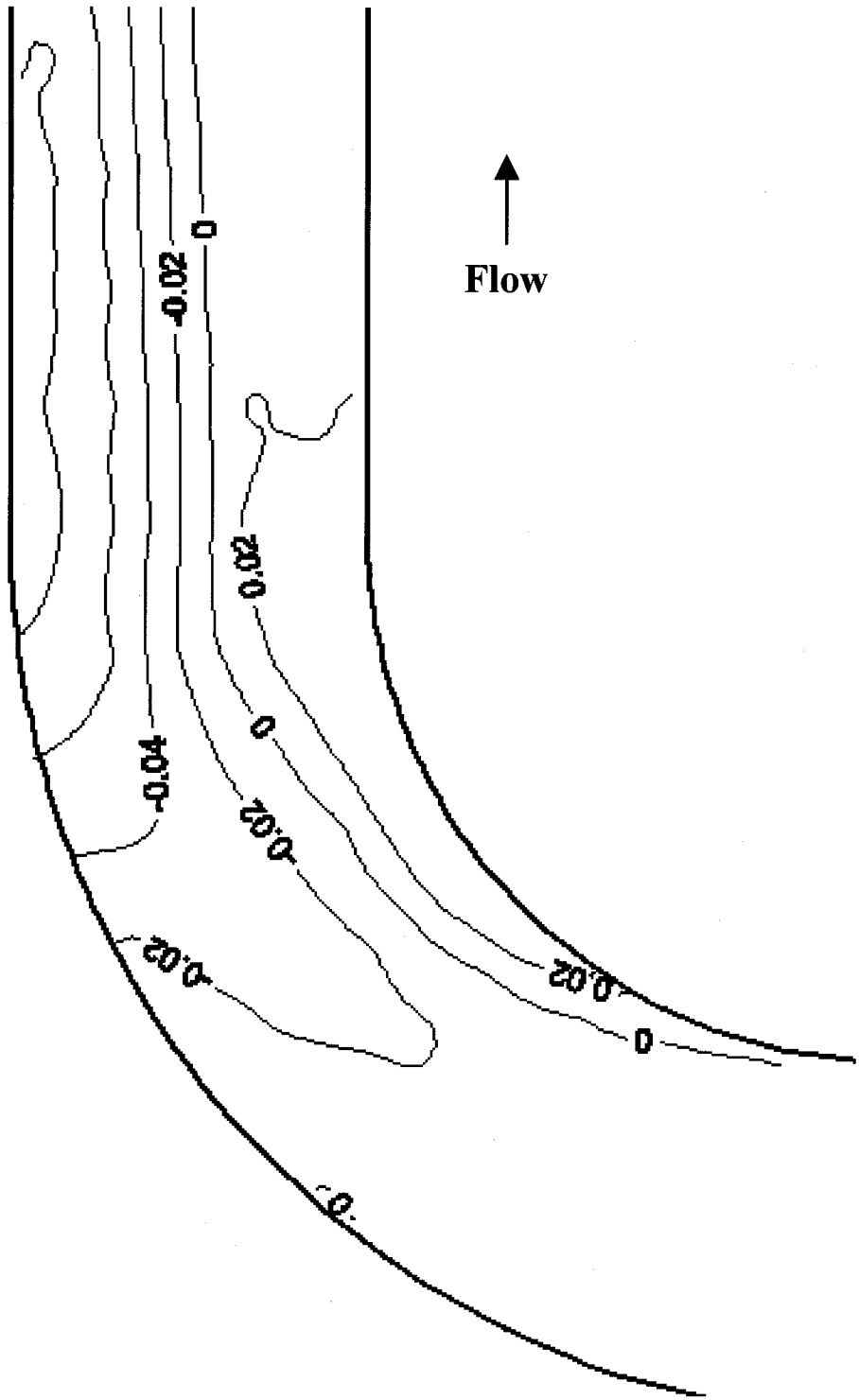

Figure B.1 Predicted reference bed elevation contour map for 90° bend (m)

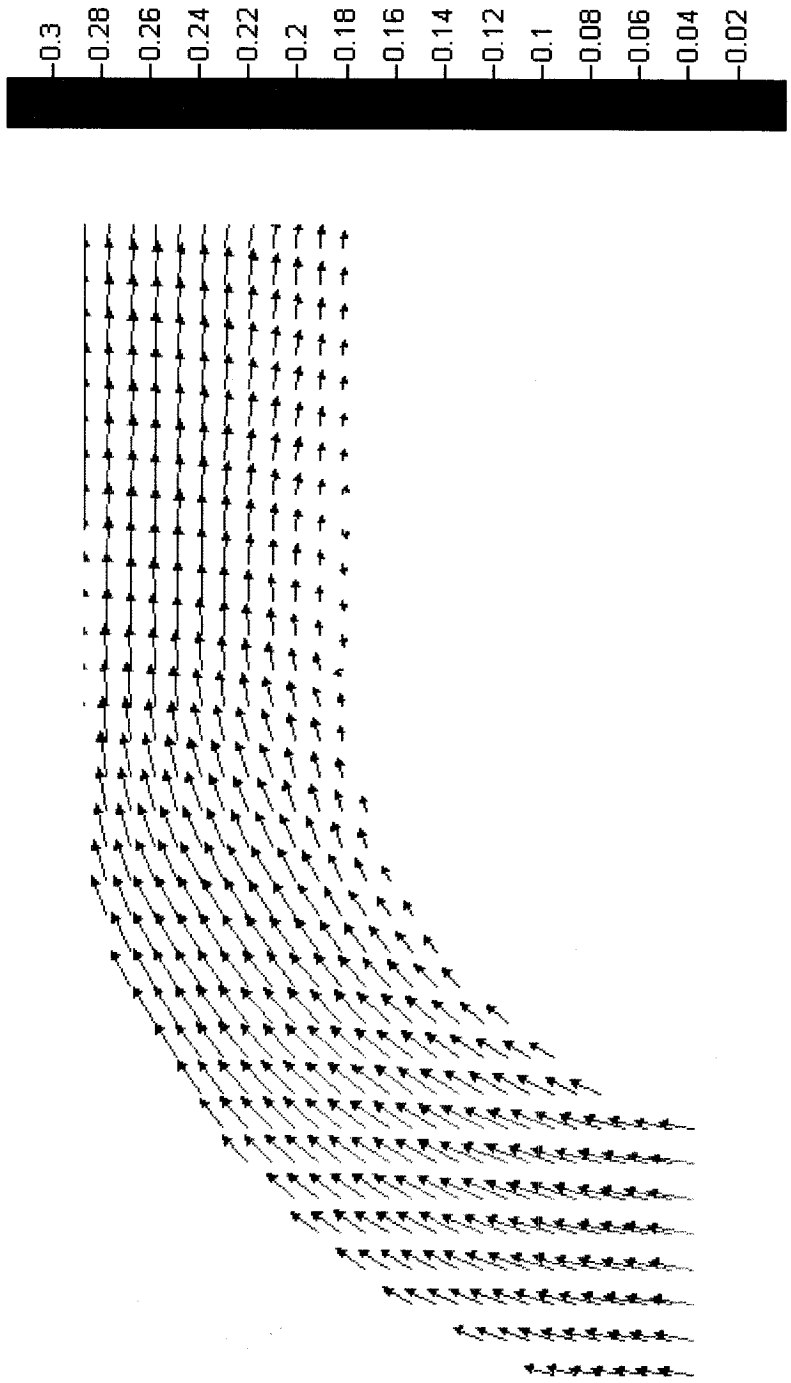

Figure B.2 Predicted depth-averaged horizontal velocity vectors for 90° reference bend (m/s)

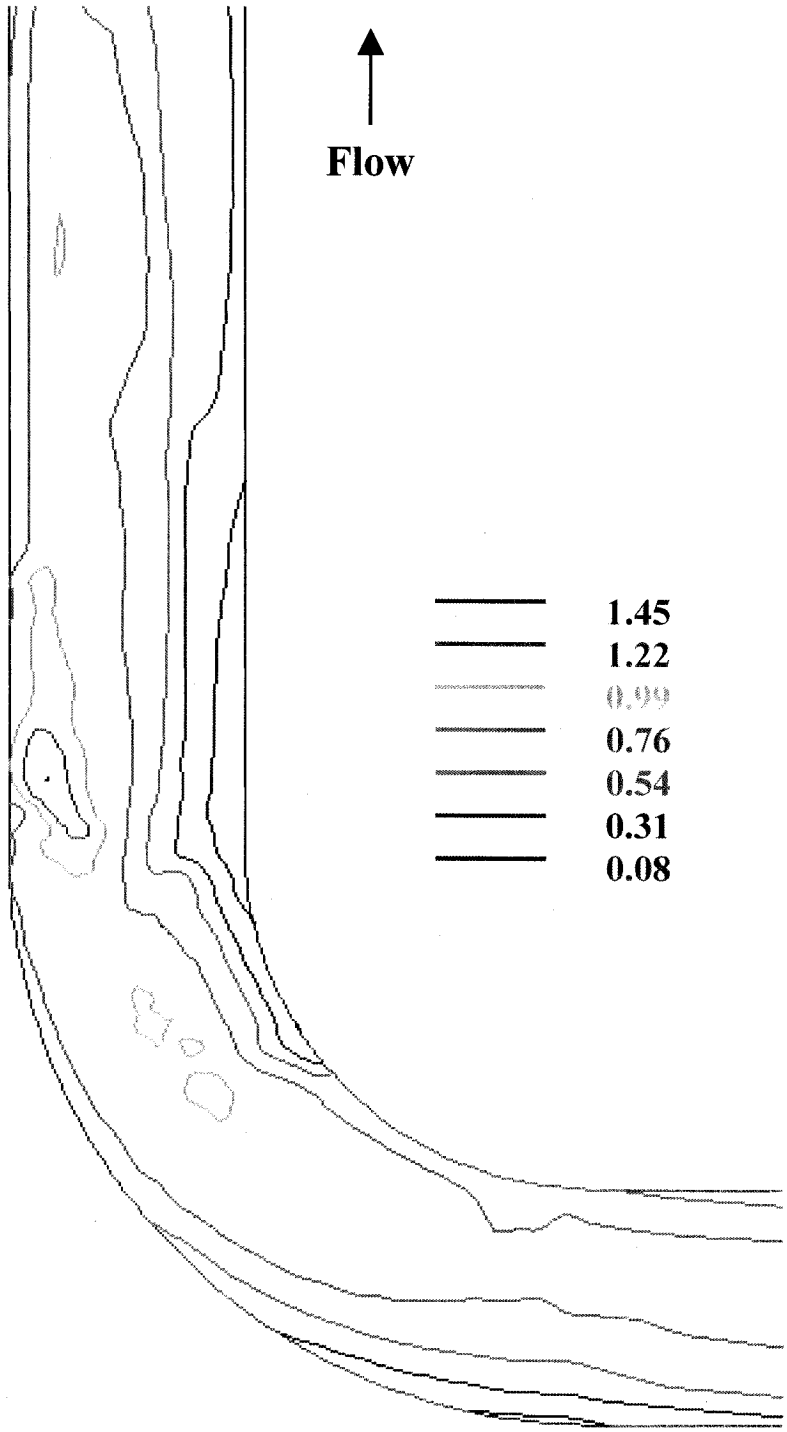

Figure B.3 Predicted bed shear stress distribution for the 90° reference bend (N/m^2)

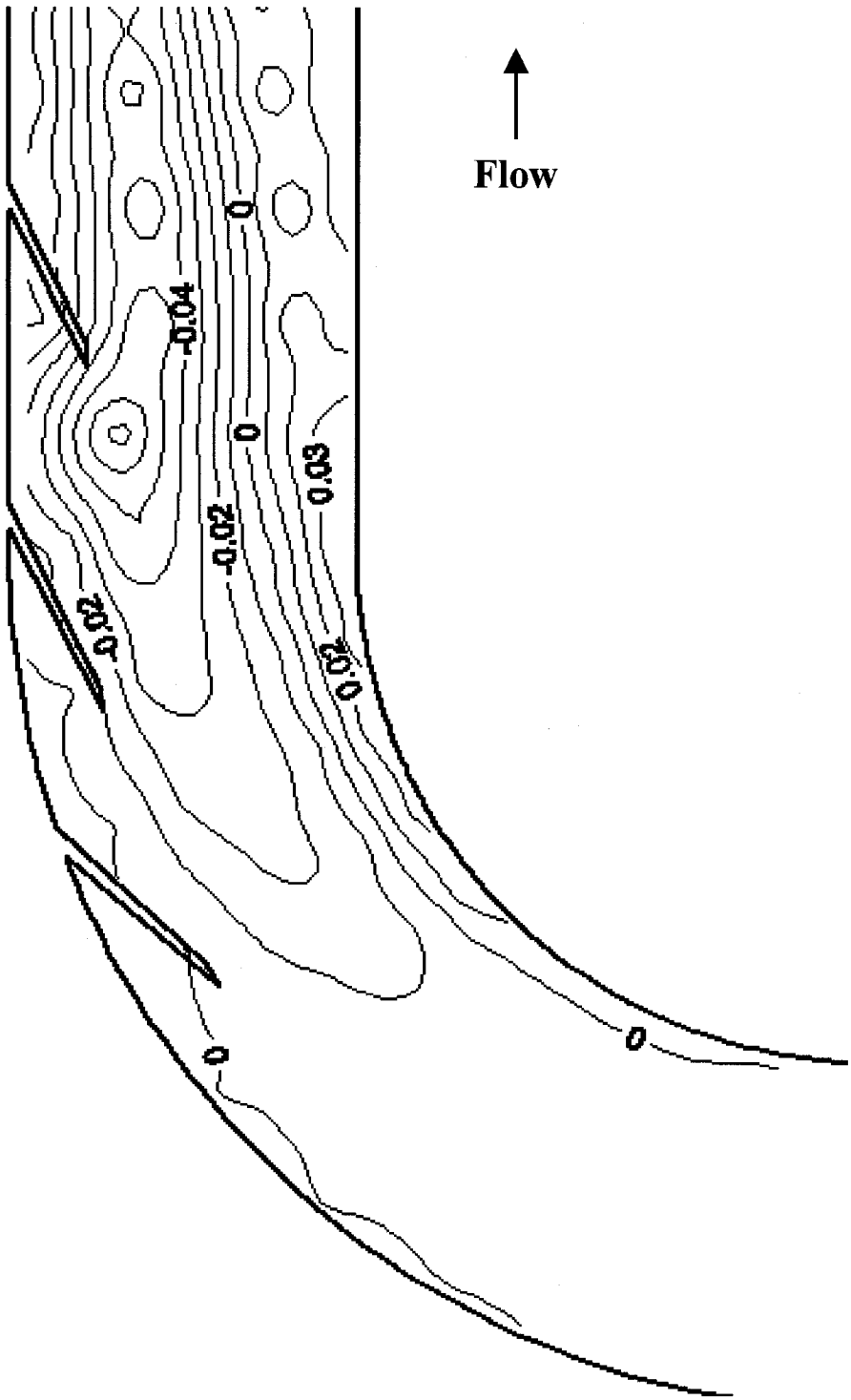

Figure B.4 Predicted bed elevation contour map: 90° channel, Group B, θ=20° (m)

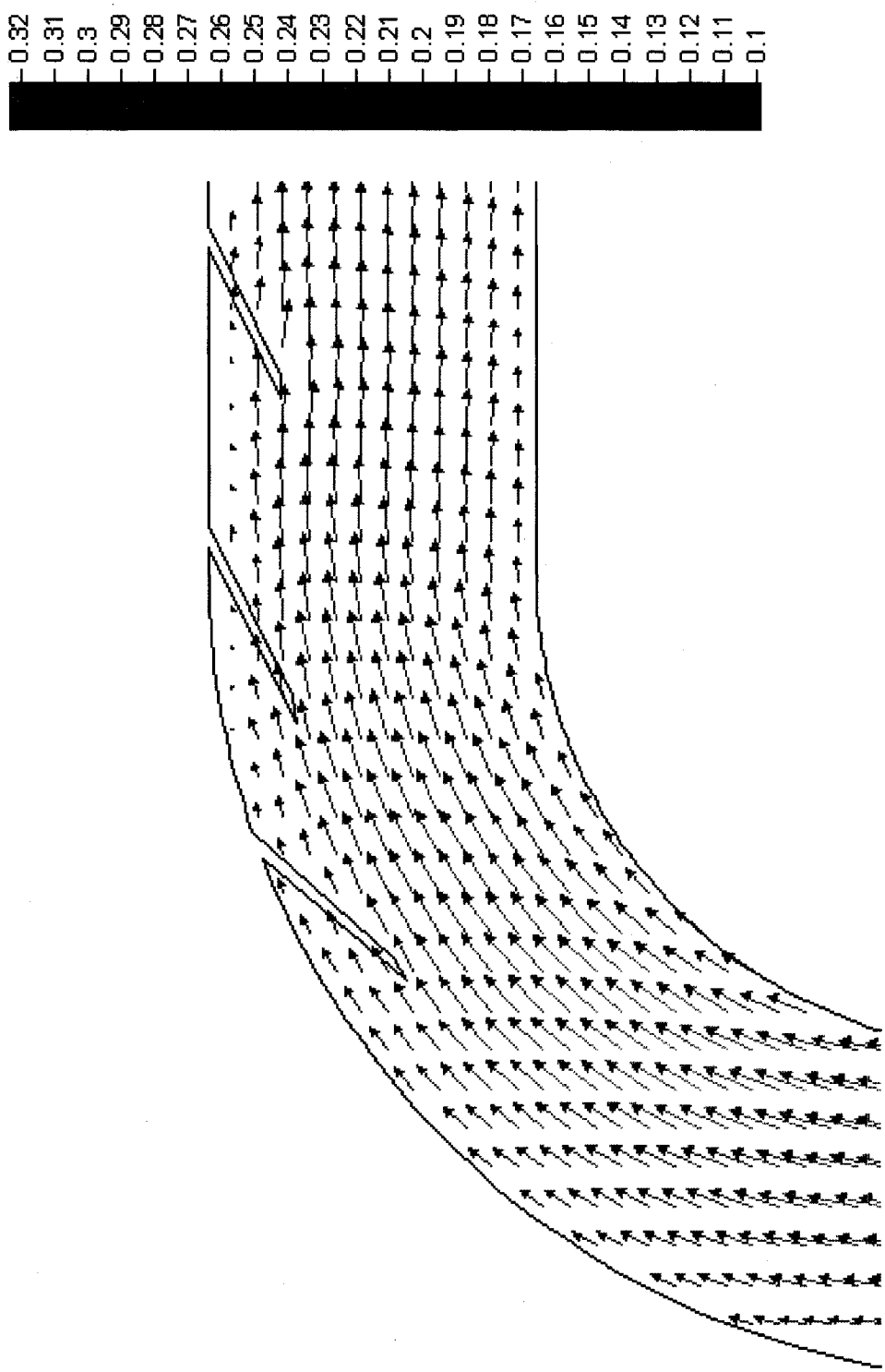

Figure B.5 Predicted depth-averaged horizontal velocity vectors: 90° bend, Group B, $\theta = 20^{\circ}$ (m/s)

Figure B.6 Predicted bed shear stress distribution: 90° bend, Group B, $\theta = 20^{o}$ (N/m^2). Channel wall and blocked out regions (barbs) in red.

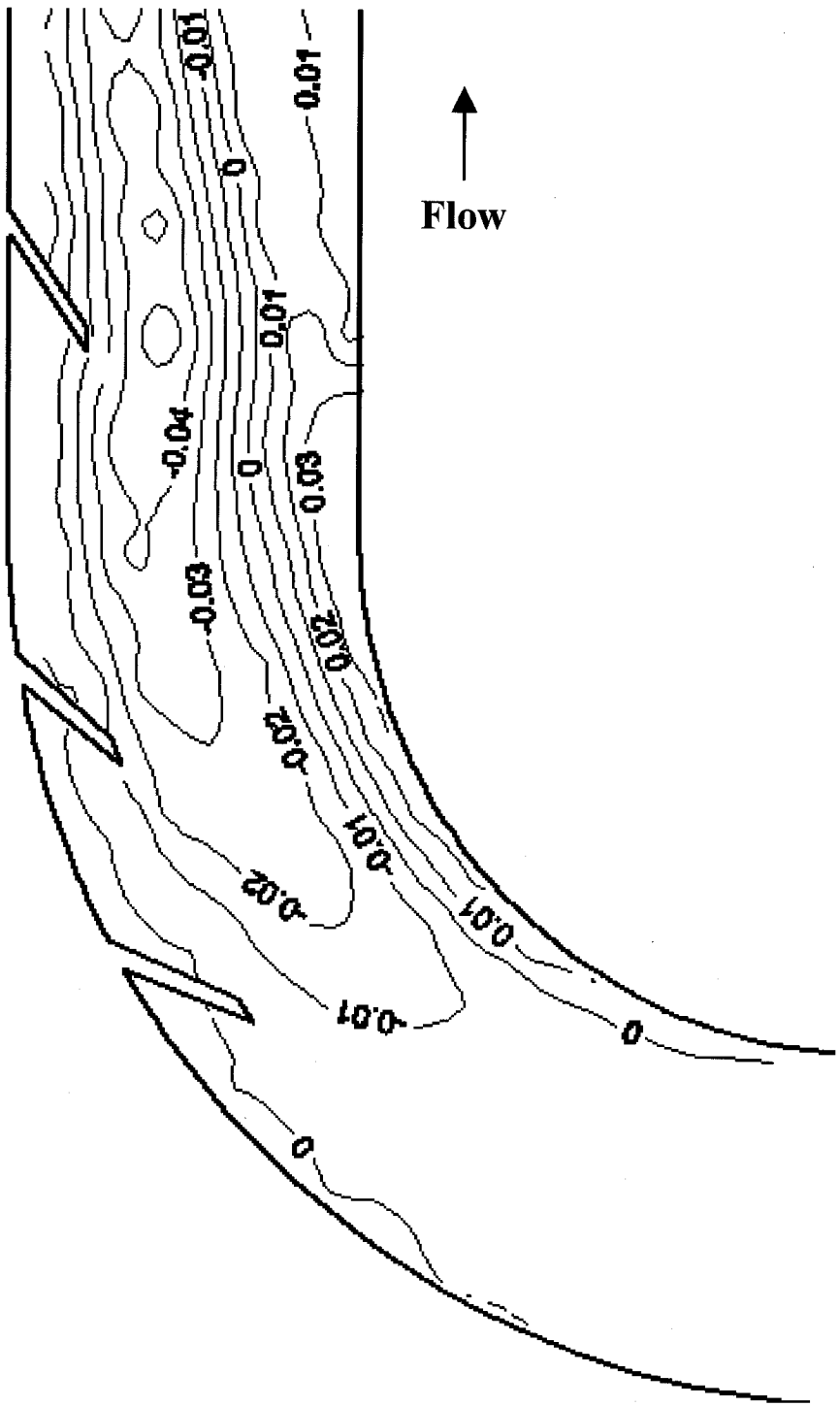

Figure B.7 Predicted bed elevation contour map: 90° channel, Group A, θ=30° (m)

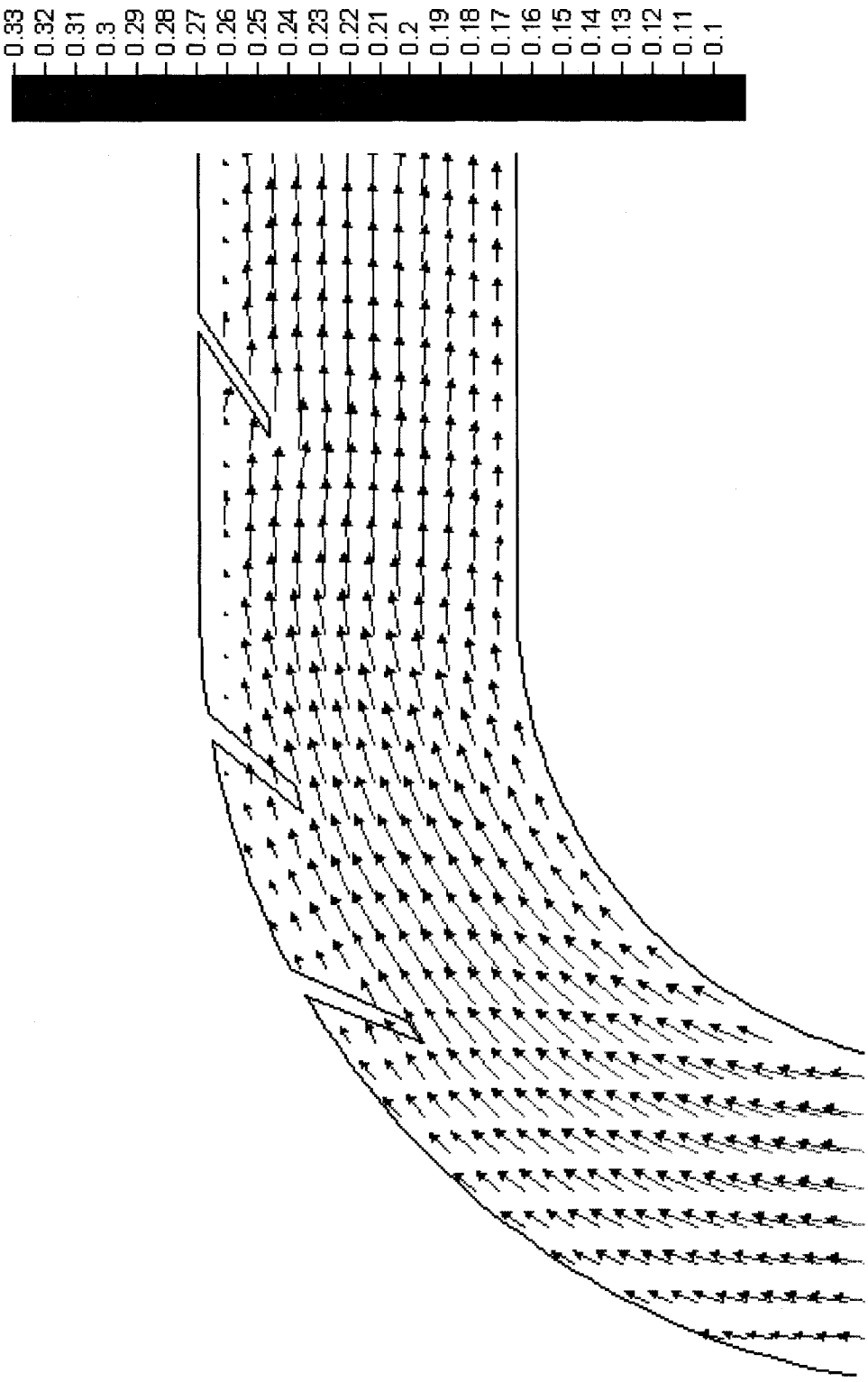

Figure B.8 Predicted depth-averaged horizontal velocity vectors: 90° bend, Group A, $\theta = 30^{o}$ (m/s)

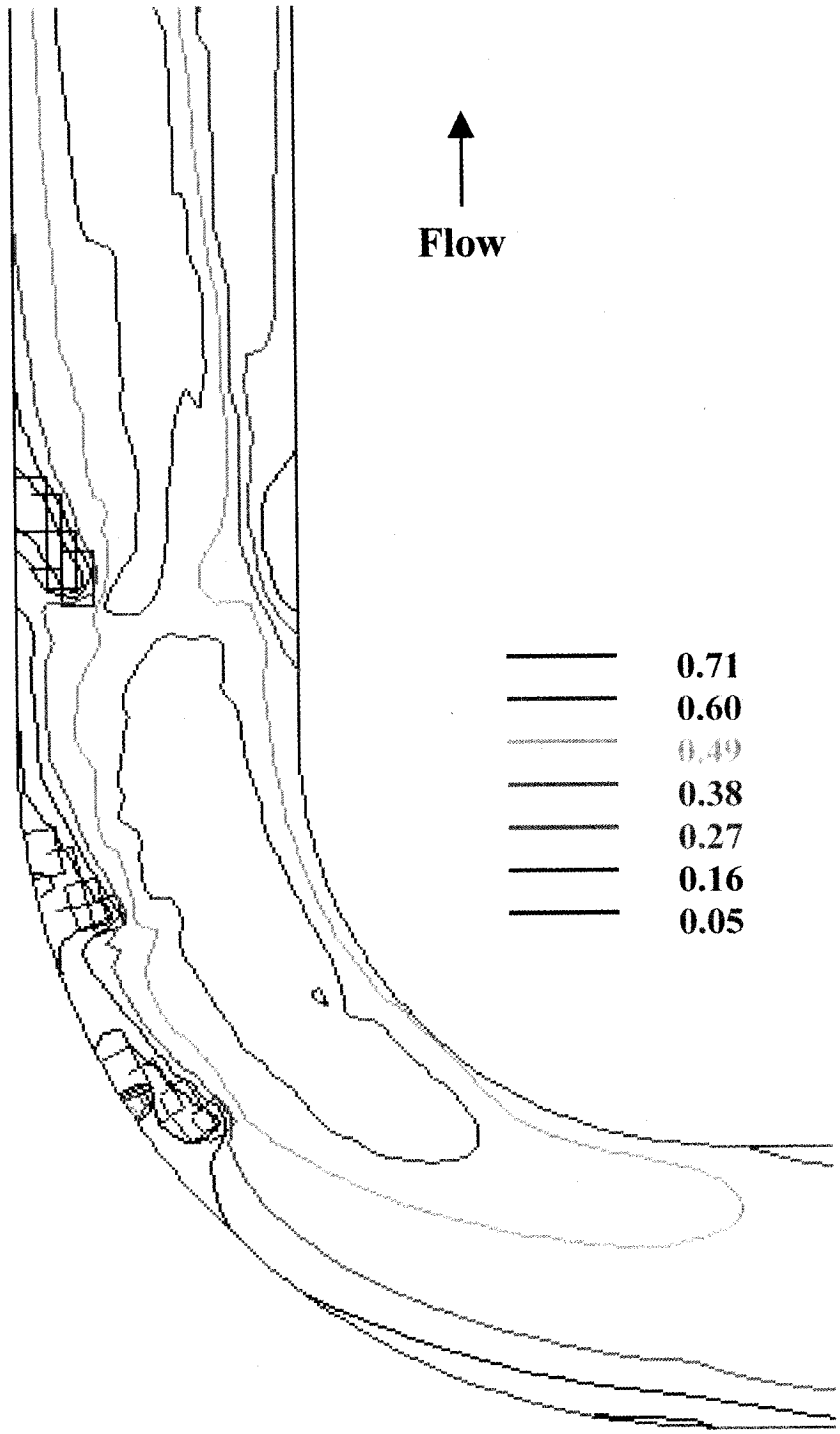

Figure B.9 Predicted bed shear stress distribution: 90° bend, Group A, $\theta = 30^{\circ}$ (in N/m^2). Channel wall and blocked out regions (barbs) in red.

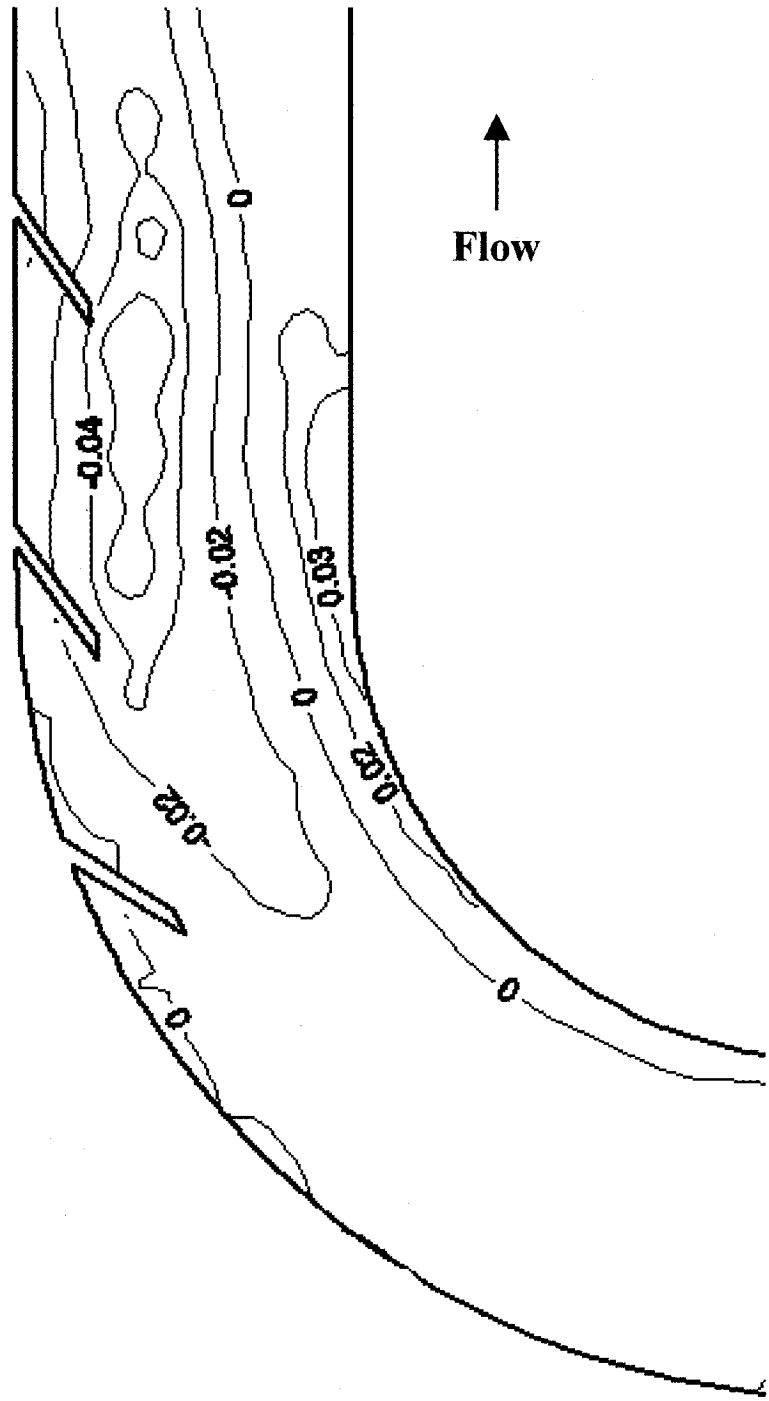

Figure B.10 Predicted bed elevation contour map: 90° channel, Group B, θ=30° (m)

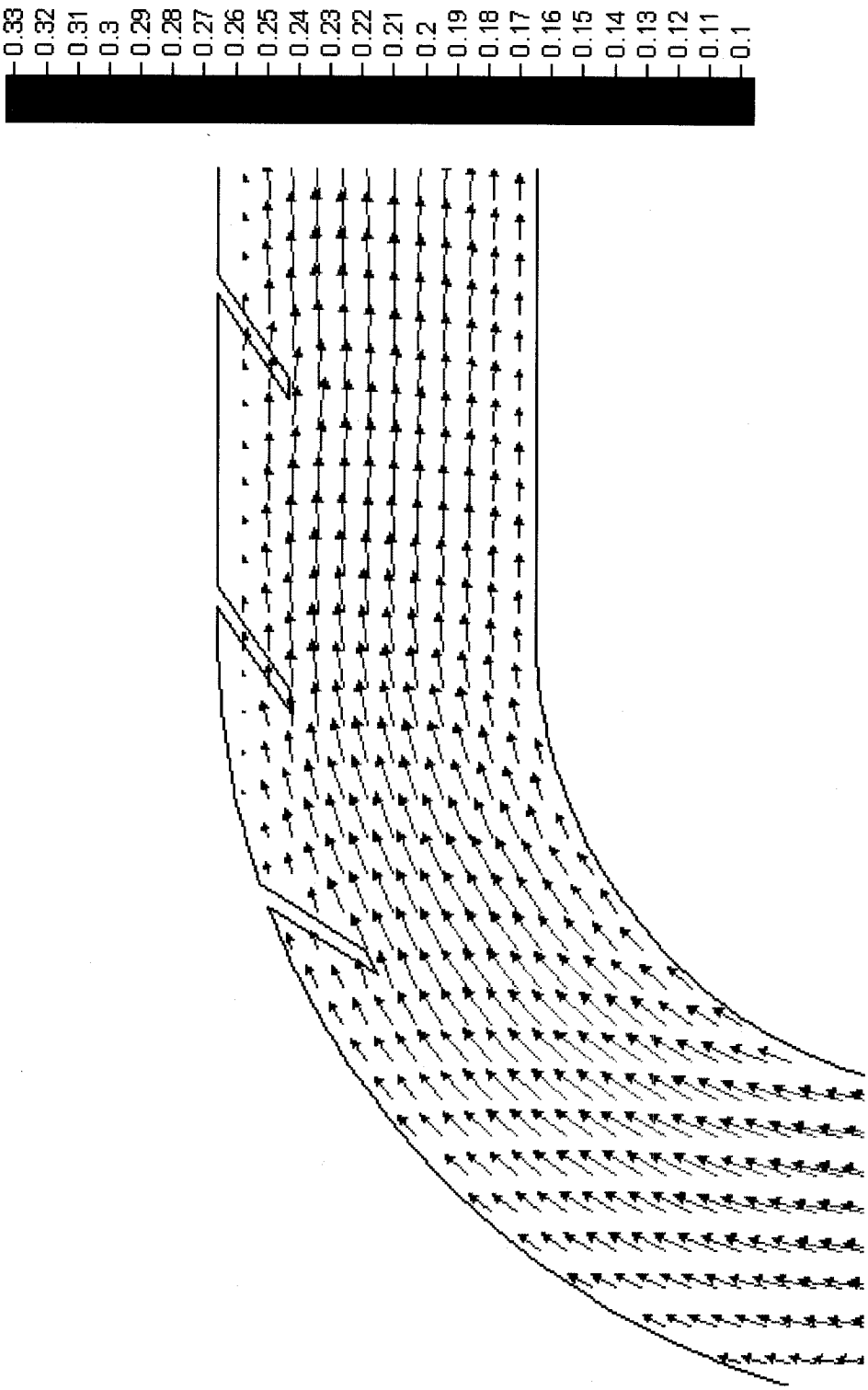

Figure B.11 Predicted depth-averaged horizontal velocity vectors: 90° bend, Group B, $\theta = 30^{o}$ (m/s)

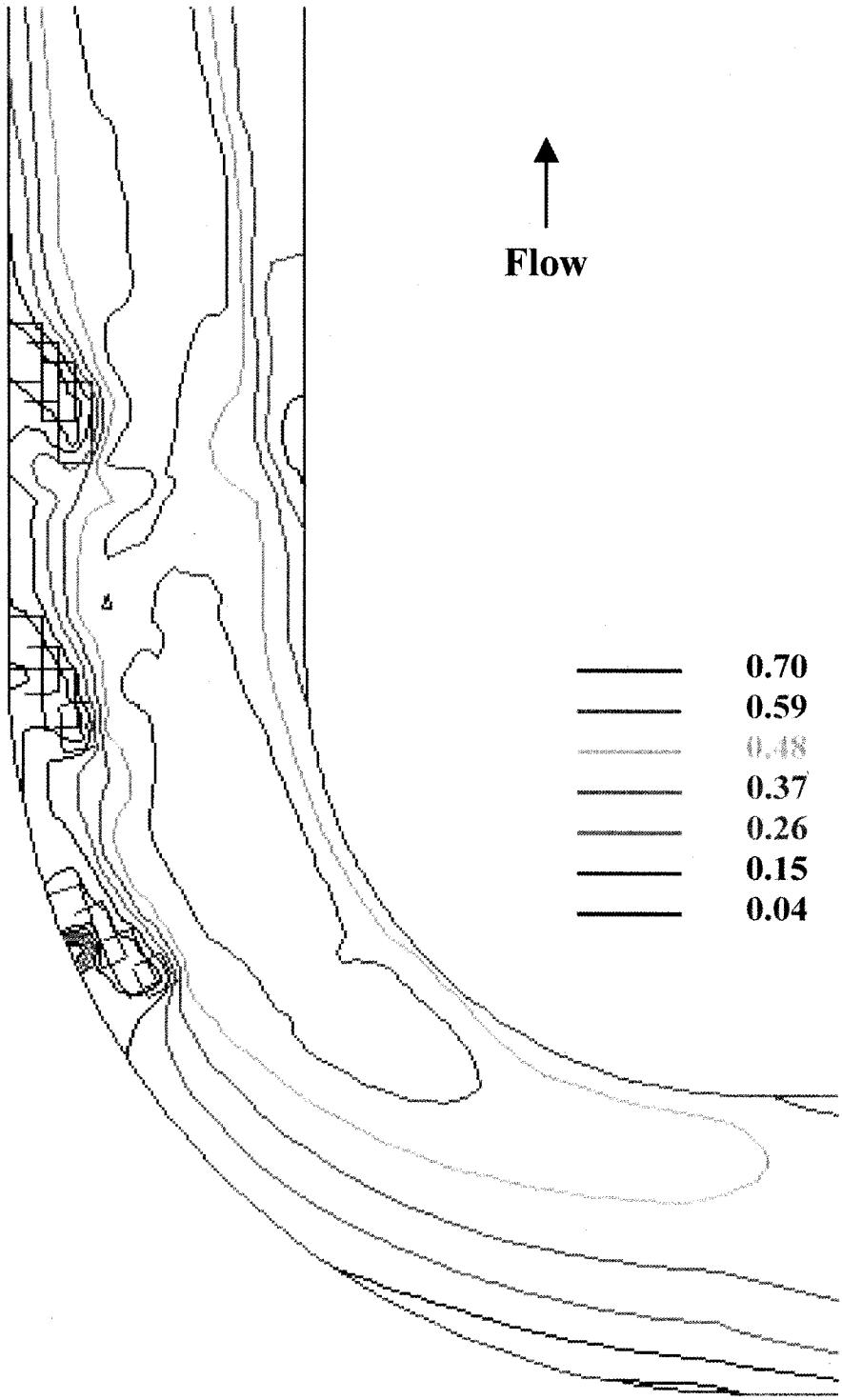

Figure B.12 Predicted bed shear stress distribution: 90° bend, Group B, $\theta = 30^{o}$ (in N/m^2). Channel wall and blocked out regions (barbs) in red.

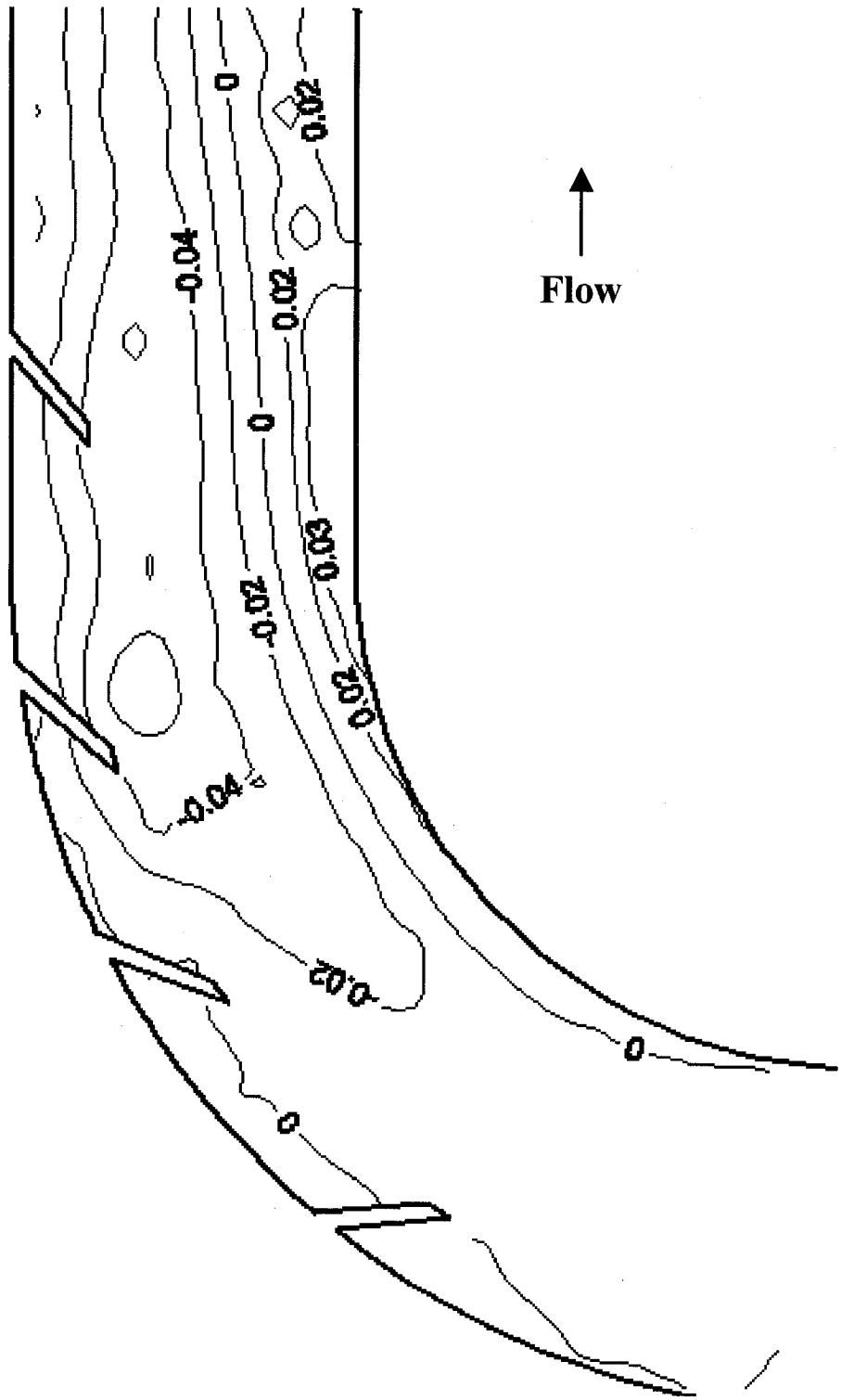

Figure B.13 Predicted bed elevation contour map: 90° channel, Group C, θ=30° (m)

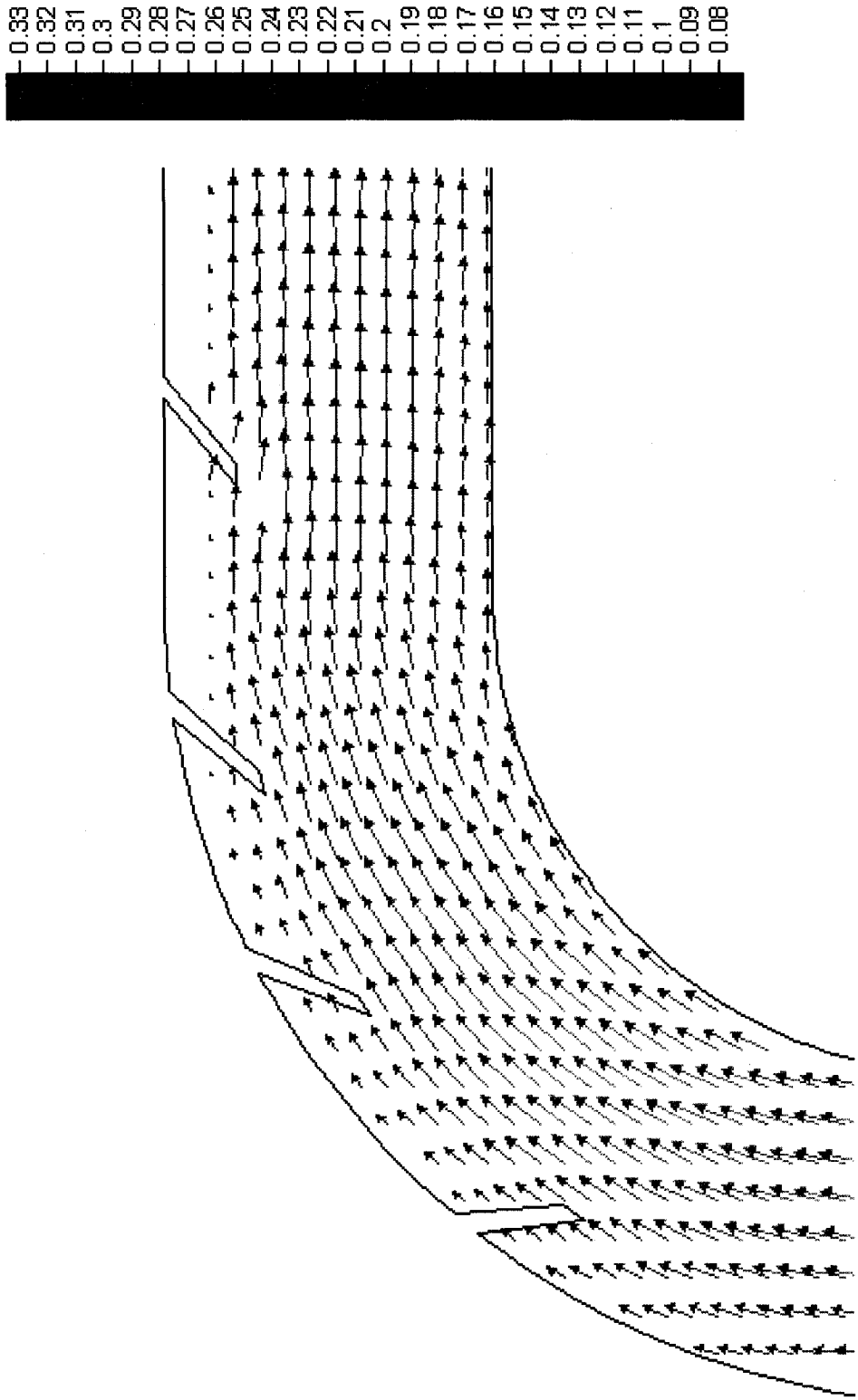

Figure B.14 Predicted depth-averaged horizontal velocity vectors: 90° bend, Group C, $\theta = 30^{o}$ (m/s)

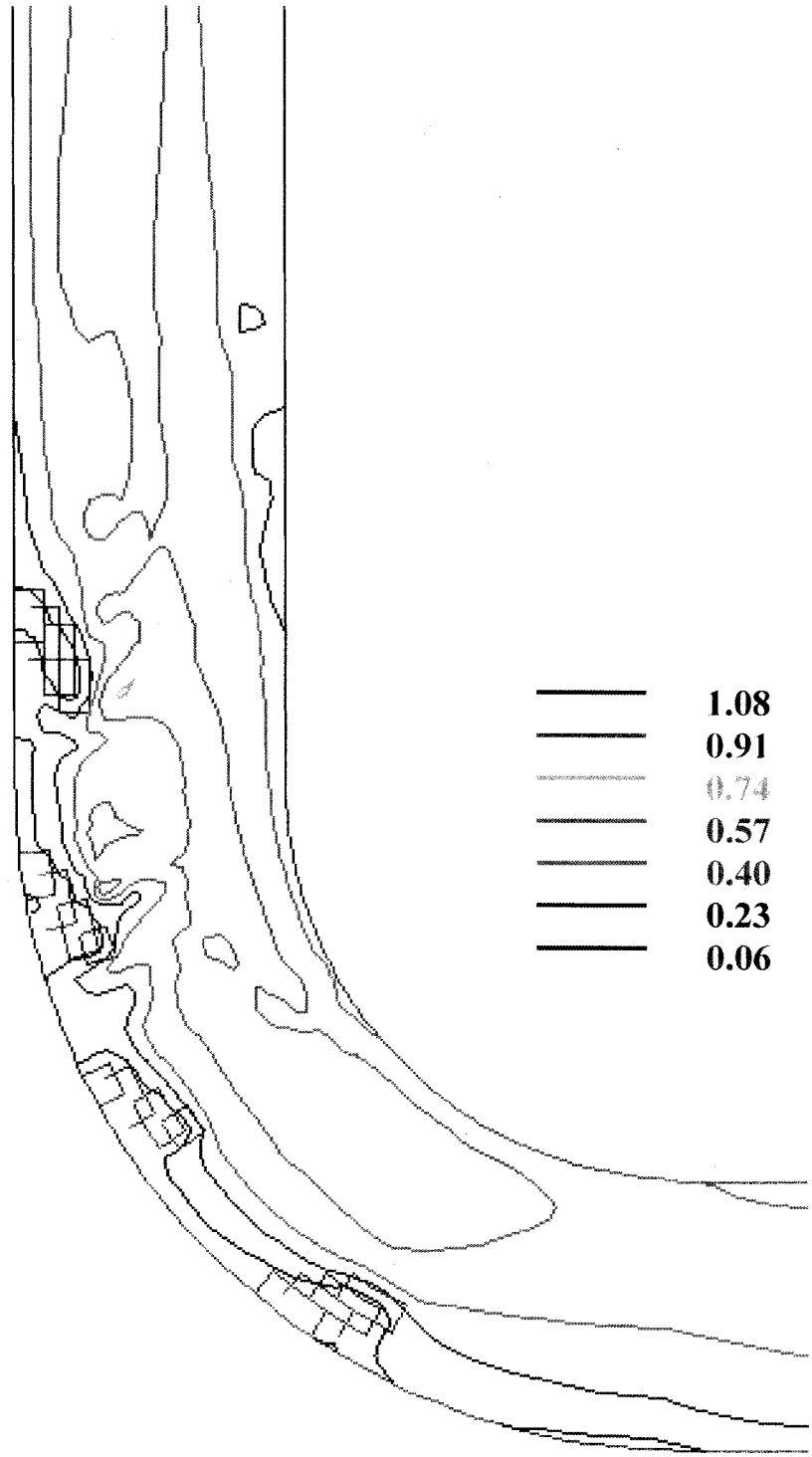

Figure B.15 Predicted bed shear stress distribution: 90° bend, Group C, θ = 30° (in N/m^2). Channel wall and blocked out regions (barbs) in red.

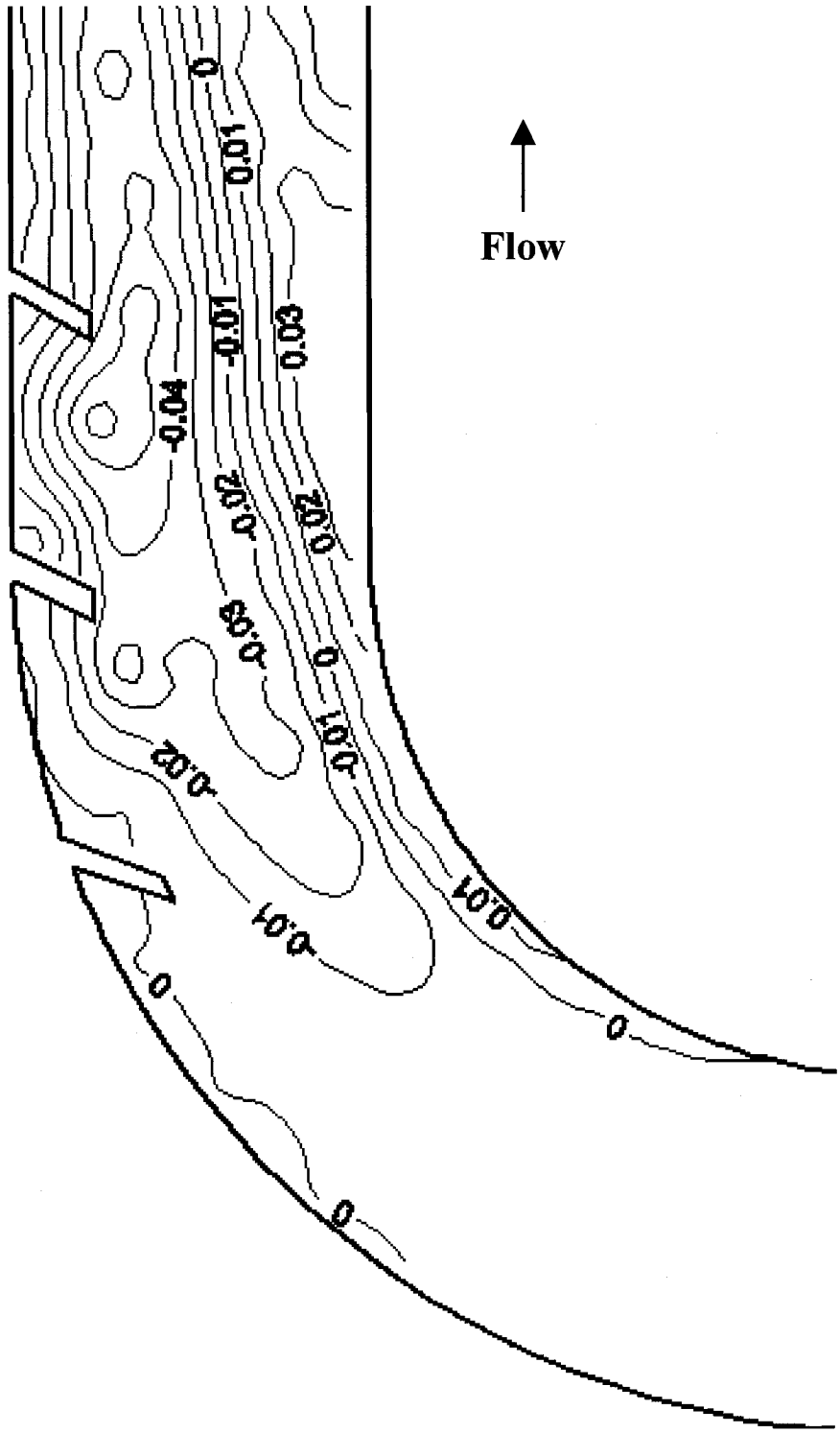

Figure B.16 Predicted bed elevation contour map: 90° channel, Group B, θ=40° (m)

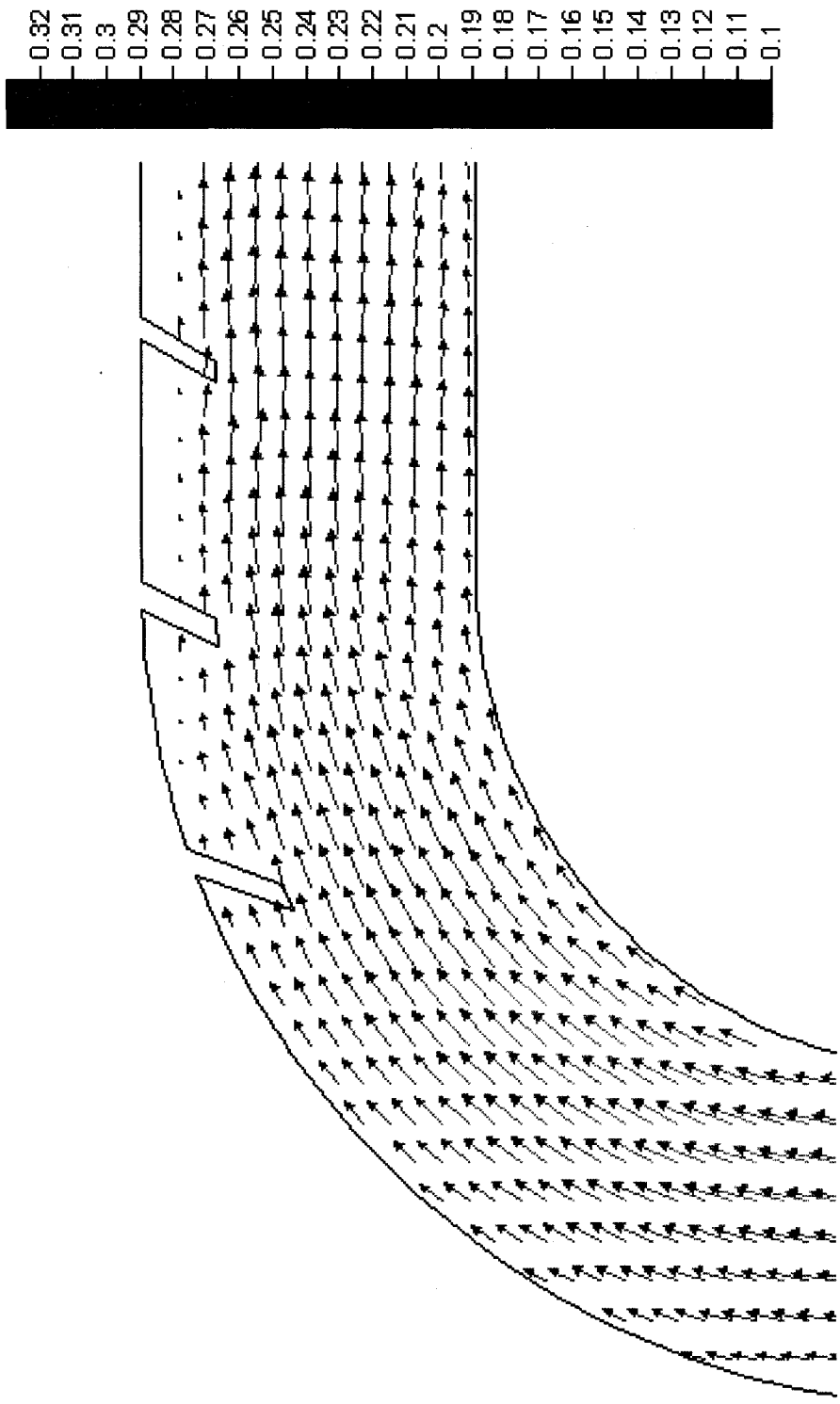

Figure B.17 Predicted depth-averaged horizontal velocity vectors: 90° bend, Group B, $\theta = 40^{o}$ (m/s)

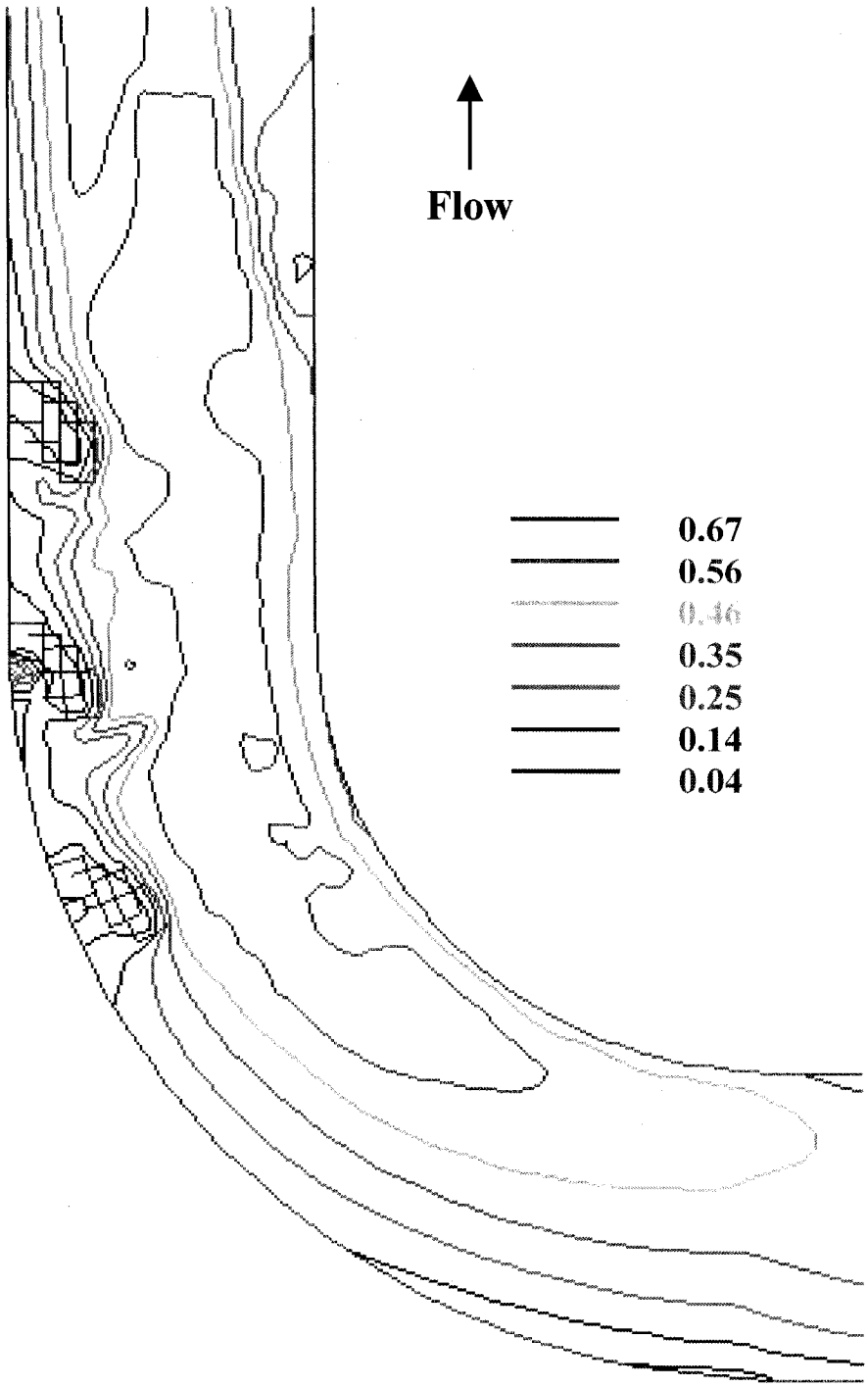

Figure B.18 Predicted bed shear stress distribution: 90° bend, Group B, $\theta = 40^{\circ}$ (in N/m^2). Channel wall and blocked out regions (barbs) in red.

APPENDIX C
Three-Dimensional Numerical Model Results for 135° Channel

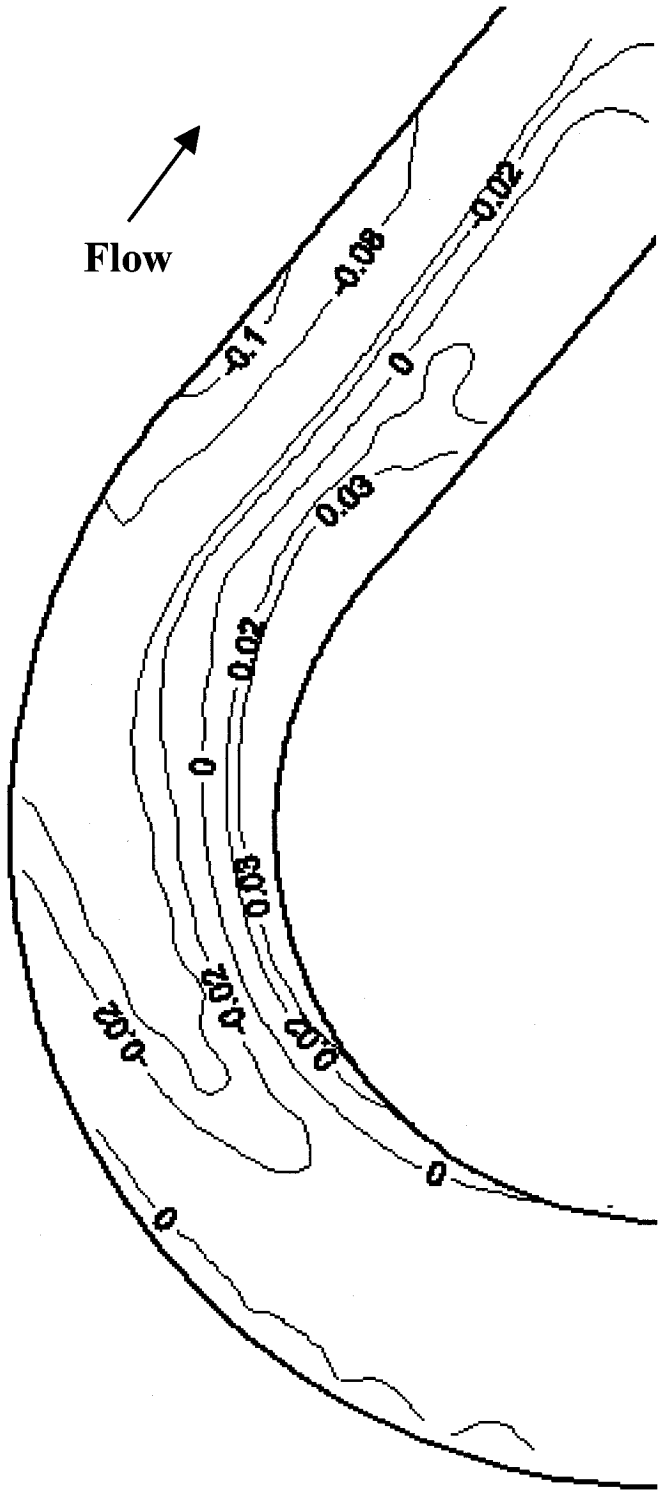

Figure C.1 Predicted reference bed elevation contour map for 135° reference bend (in m)

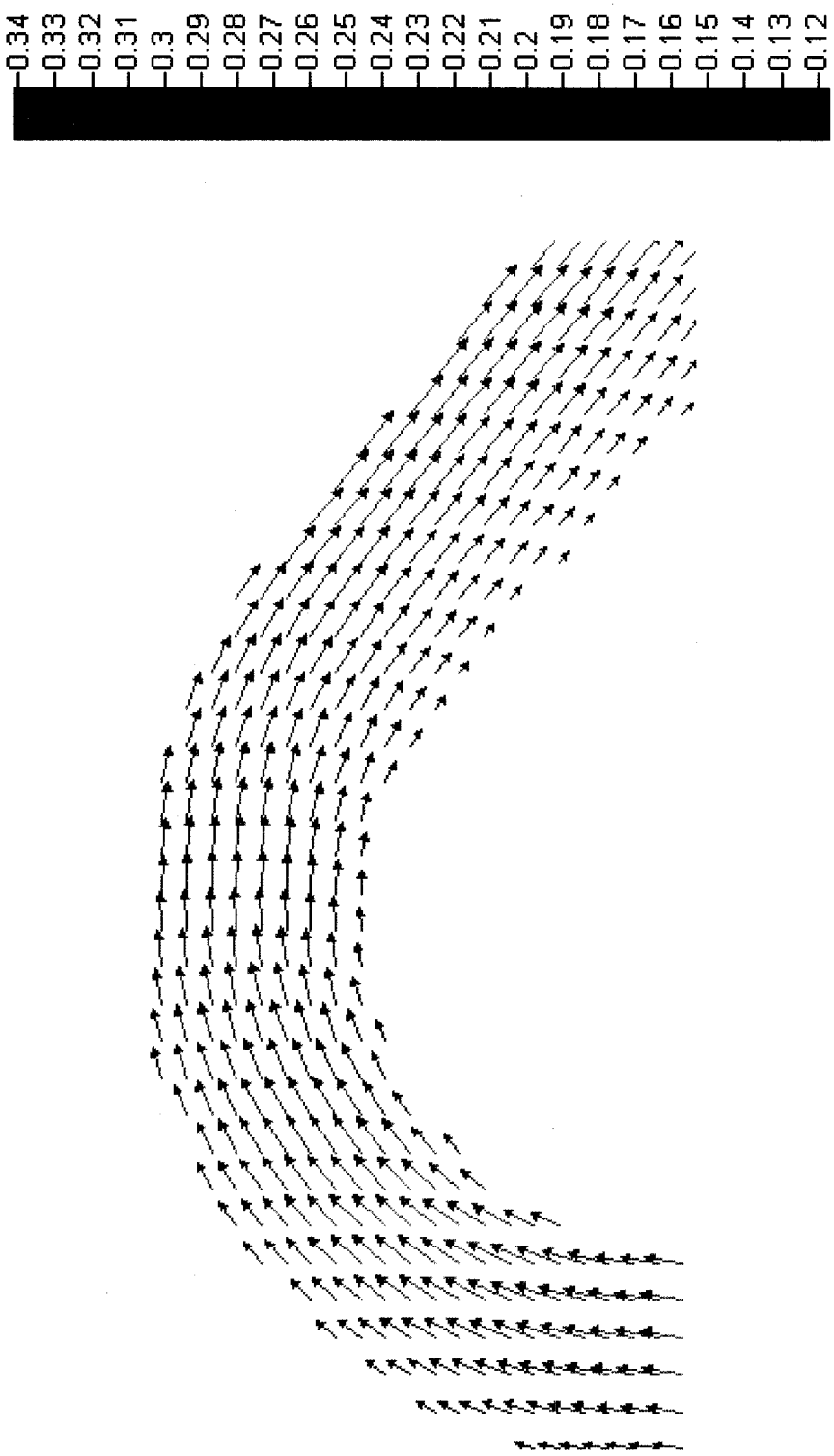

Figure C.2 Predicted depth-averaged horizontal velocity vectors for 135° reference bend (m/s)

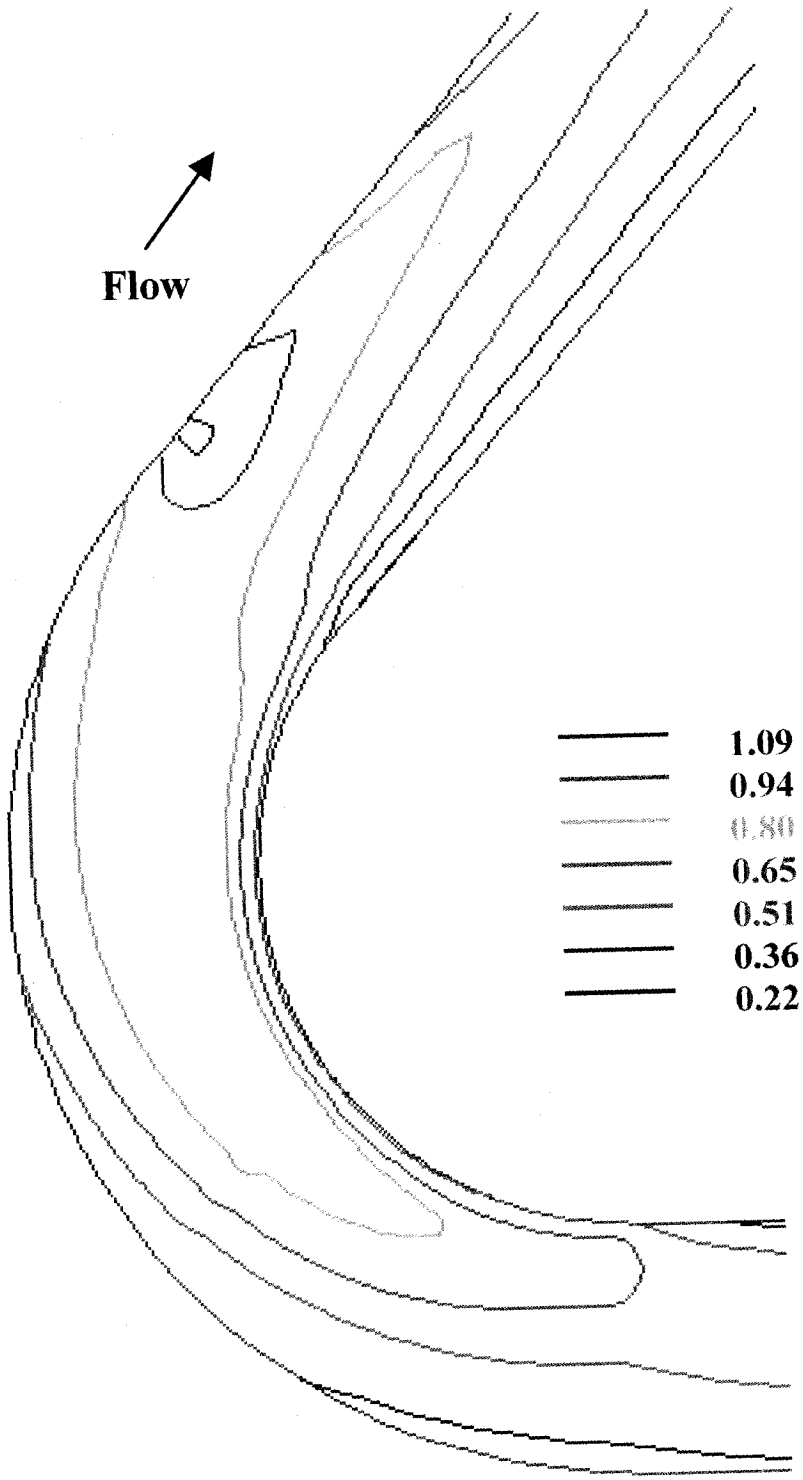

Figure C.3 Predicted bed shear stress distribution for the 135° reference bend (N/m^2). Channel wall and blocked out regions (barbs) in red.

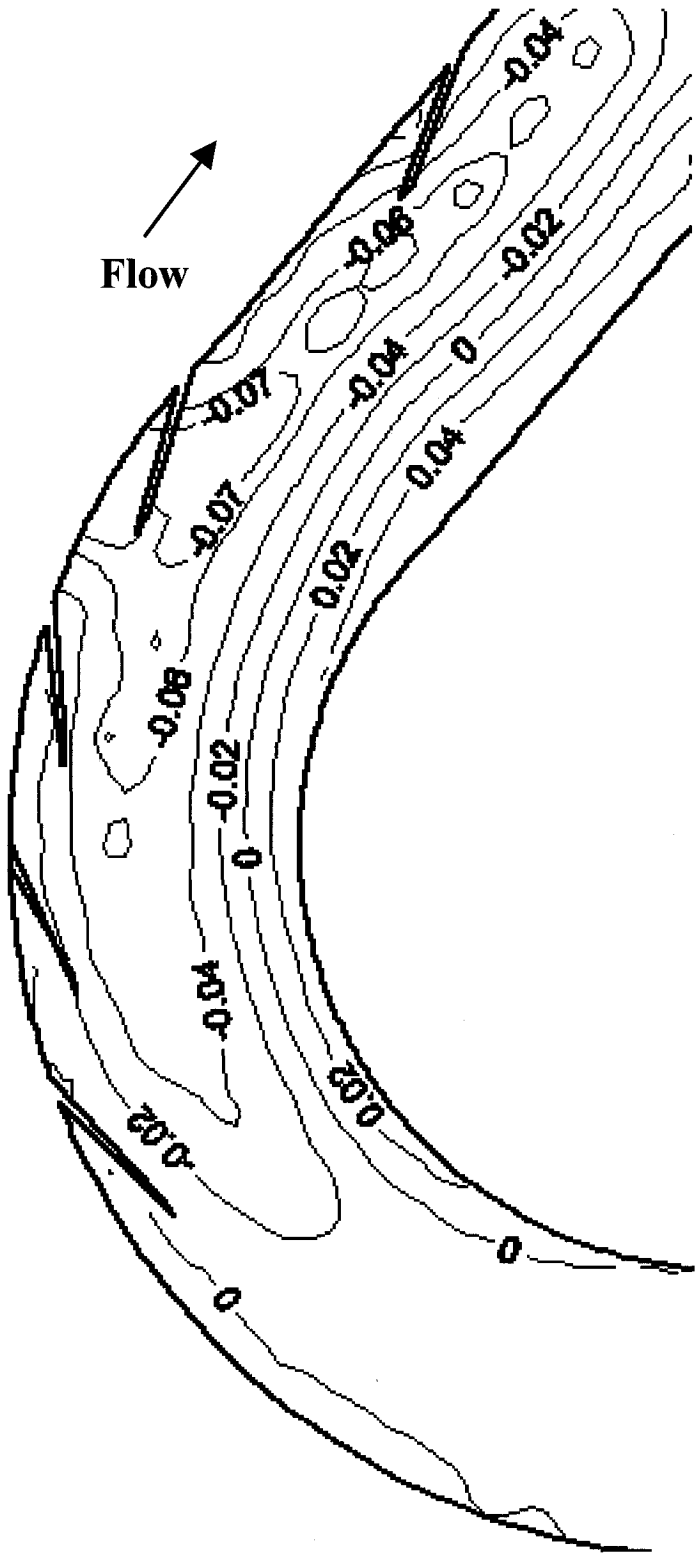

Figure C.4 Predicted bed elevation contour map: 135° channel, Group B, θ=20° (m)

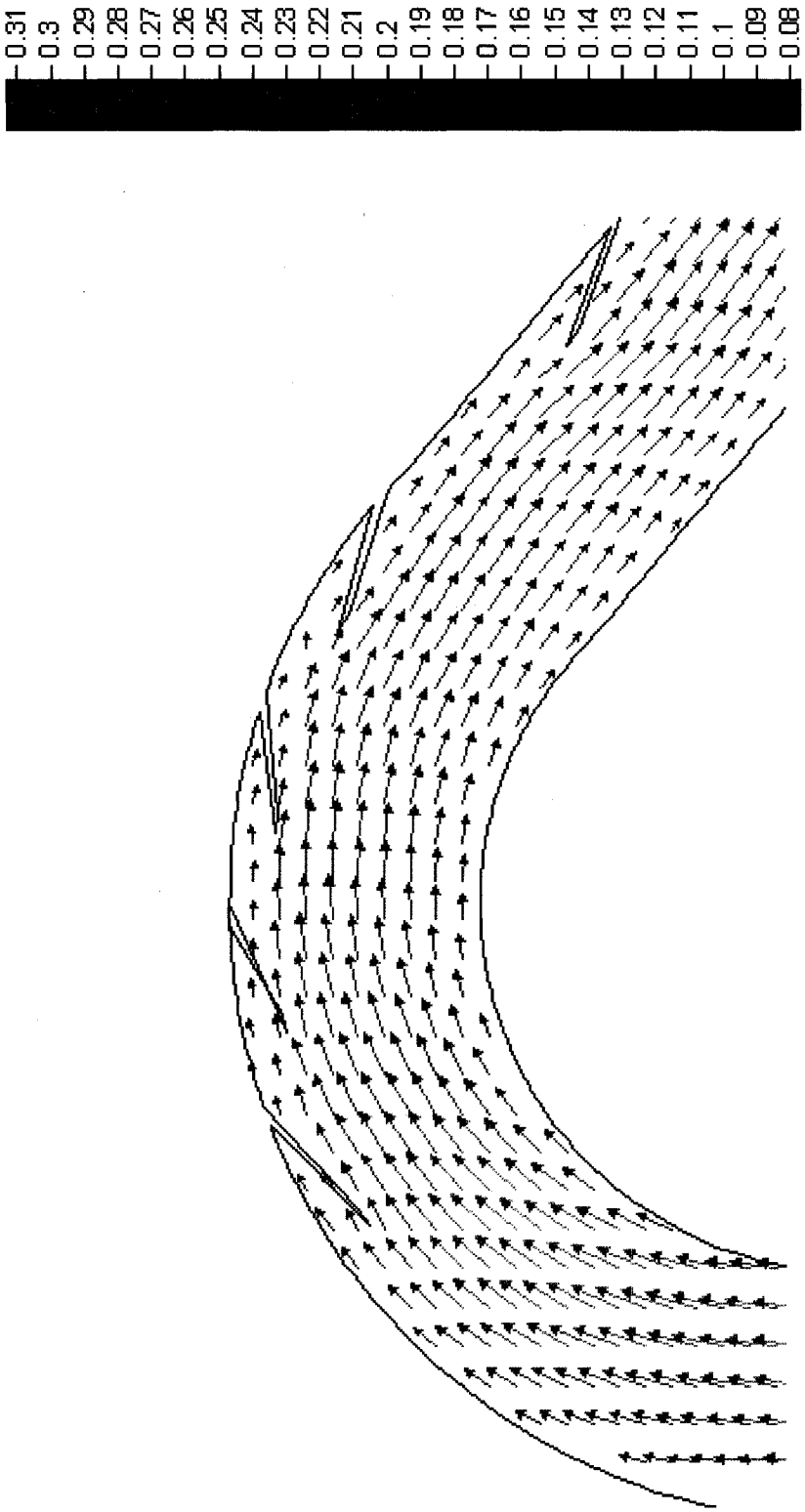

Figure C.5 Predicted depth-averaged horizontal velocity vectors: 135° bend, Group B, $\theta = 20^{o}$ (m/s)

Figure C.6 Predicted bed shear stress distribution: 135° bend, Group B, $\theta = 20^{\circ}$ (N/m^2). Channel wall and blocked out regions (barbs) in red.

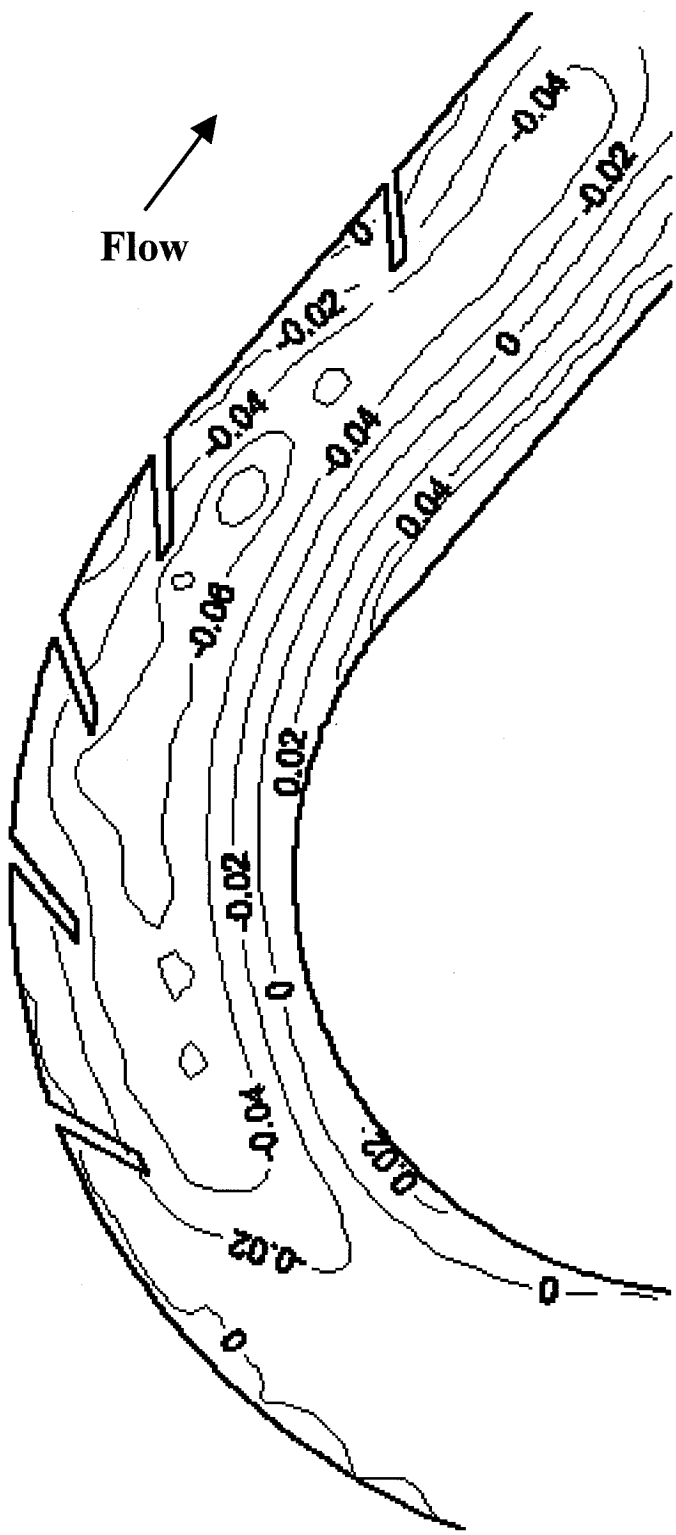

Figure C.7 Predicted bed elevation contour map: 135° channel, Group B, θ=30° (m)

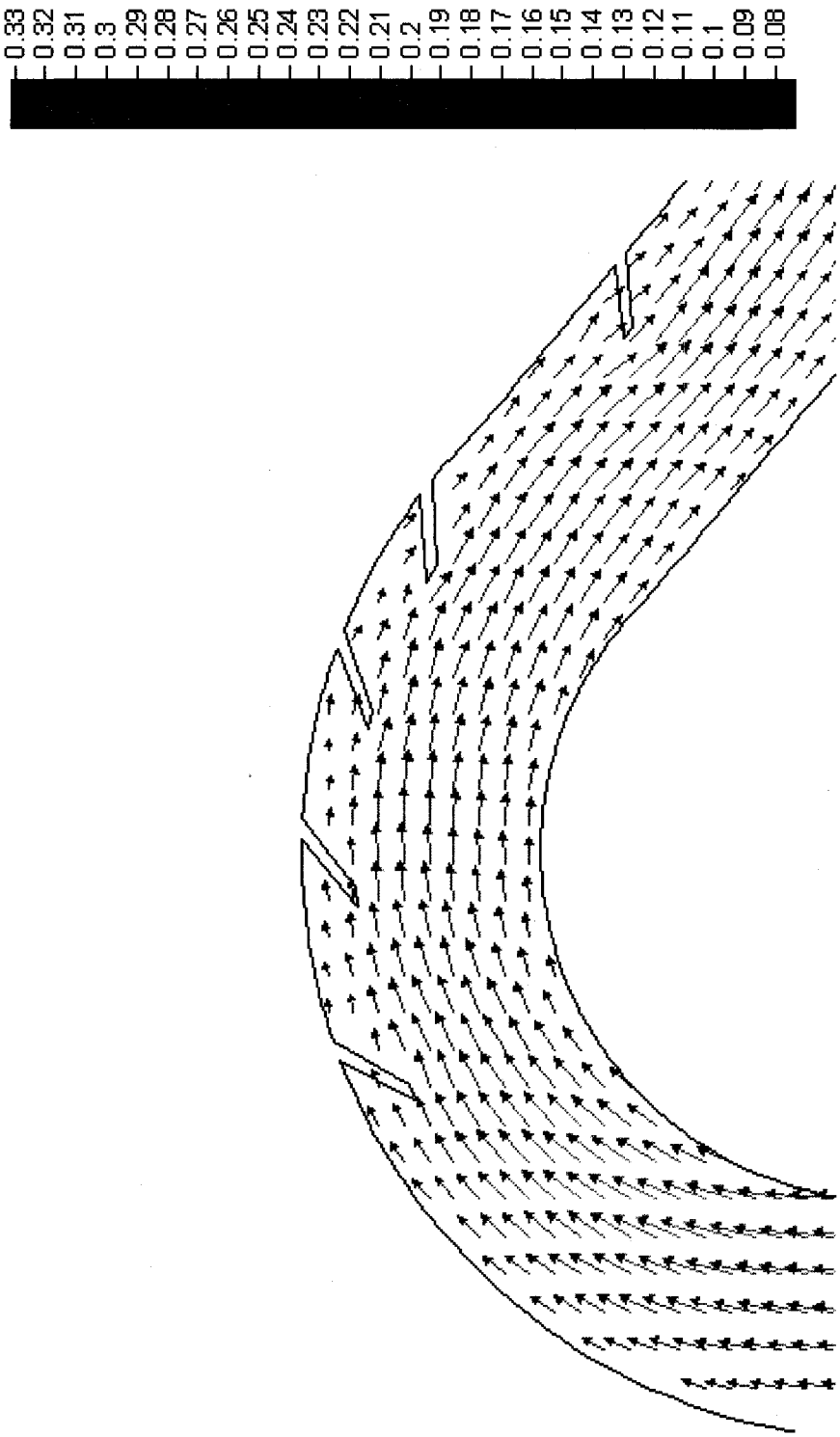

Figure C.8 Predicted depth-averaged horizontal velocity vectors: 135° bend, Group B, $\theta = 30^{o}$ (m/s)

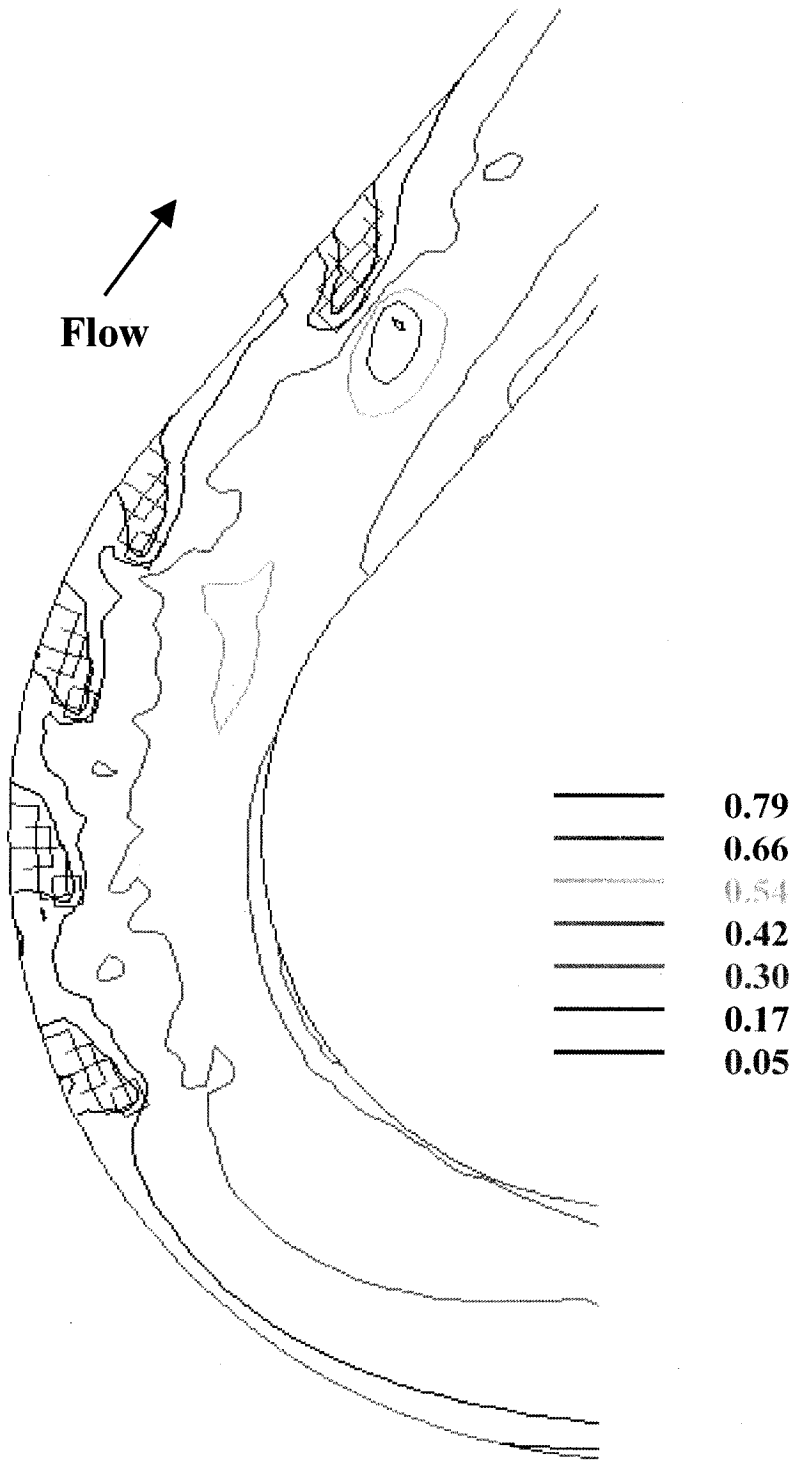

Figure C.9 Predicted bed shear stress distribution: 135° bend, Group B, $\theta = 30^{o}$ (N/m^2). Channel wall and blocked out regions (barbs) in red.

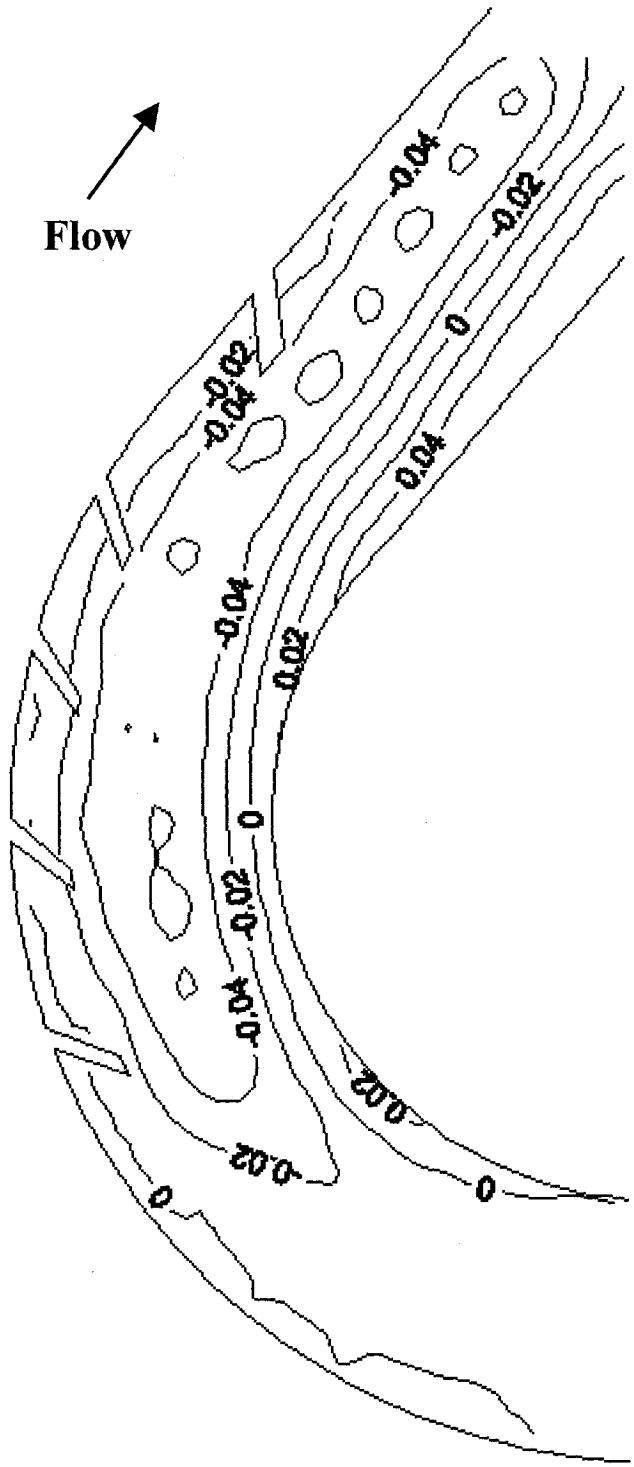

Figure C.10 Predicted bed elevation contour map: 135° channel, Group B, θ=40° (m)

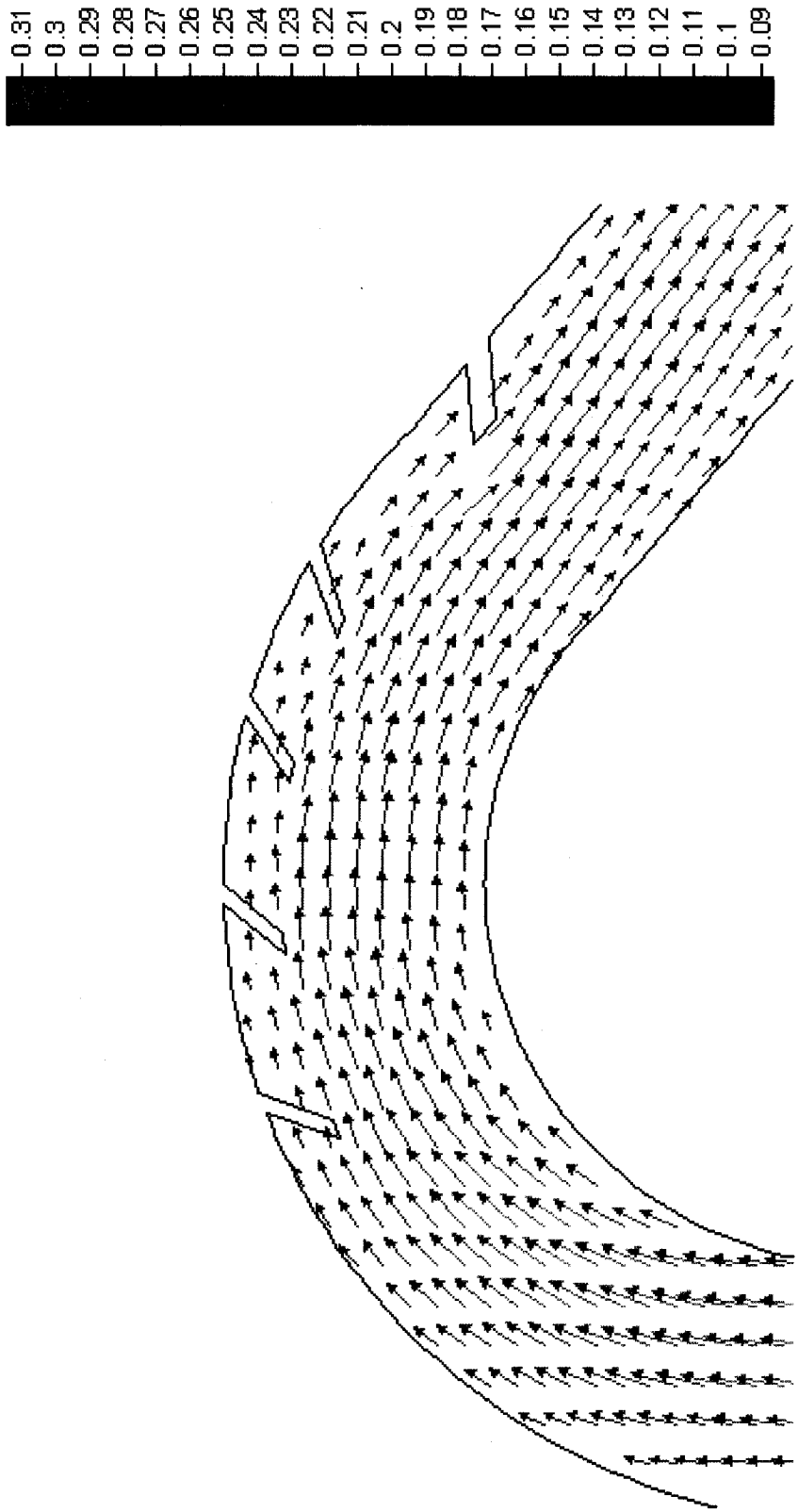

Figure C.11 Predicted depth-averaged horizontal velocity vectors: 135° bend, Group B, $\theta = 40^{\circ}$ (m/s)

Figure C.12 Predicted bed shear stress distribution: 135° bend, Group B, $\theta = 40^{o}$ (N/m^2). Channel wall and blocked out regions (barbs) in red. .

APPENDIX D
SSIIM Input Files

```
T water flow through 90 degree reference channel
F 2 W
F 10 R
F 11 2.65 0.047
F 33 1.0 1
G 1 124 19 13 4     grid and array sizes
G 3 0 5 10 20 30 40 50 60 70 80 90 95 100    vertical grid distribution
G 7 0 1 2 19 2 13 0 0 0.0132 1 0
G 7 1 -1 2 19 2 13 0 0 0.0132 1 0
P 2 1.0 1.0 1.0 0.0 0.0
P 3 12 4 13 4
I 1 0
I 2 0
I 3 0
I 4 0
S 1 0.0011 0.11
S 2 0.00085 0.105
S 3 0.0006589 0.08
S 4 0.00015 0.015
N 0 1 0.16
N 0 2 0.34
N 0 3 0.34
N 0 4 0.16
B 0 22 2 124 19
W 1 60 0.0132 0.28975
W 2 5 1 40 70 95 115
K 1 5000 7000
K 2 0 1
K 3 0.8 0.8 0.8 0.2 0.5 0.5
K 4 1 1 1 5 1 1
K 5 1 1 1 1 1 1
```

```
T sediment flow through 90 degree reference channel
F 2 RIS
F 4 0.5 50 0.001
F 7 B
F 11 2.65 0.055
F 16 0.0146
F 33 50 1
F 37 1
F 48 1 write bed levels to interess file
F 54 0.001
F 56 10 0.5
F 84 1
G 1 124 19 13 4     grid and array sizes
G 3 0 5 10 20 30 40 50 60 70 80 90 95 100    vertical grid distribution
G 7 0 1 2 19 2 13 0 0 0.0132 1 0
G 7 1 -1 2 19 2 13 0 0 0.0132 1 0
P 2 1.0 1.0 1.0 0.0 0.0
P 3 12 4 13 4
I 1 0.0
I 2 0.0
I 3 0.0
I 4 0.0
S 1 0.0011 0.11
S 2 0.00085 0.105
S 3 0.0006589 0.08
S 4 0.00015 0.015
N 0 1 0.16
N 0 2 0.34
N 0 3 0.34
N 0 4 0.16
B 0 22 2 124 19
W 1 60 0.0132 0.28975
W 2 5 1 40 70 95 115
K 1 1080 60000
K 2 0 1
K 3 0.8 0.8 0.8 0.3 0.5 0.5
K 4 1 1 1 5 1 1
K 5 1 1 1 1 1 1
K 6 0 0 0 0 0 0
```

```
T water flow through 90 degree bend, Group B, alignment 30
F 2 W
F 7 G
F 10 R
F 11 2.65 0.04
F 33 50 1
G 1 124 19 13 4     grid and array sizes
G 3 0 5 10 20 30 40 50 60 70 80 90 95 100     vertical grid distribution
G 7 0 1 2 19 2 13 0 0 0.0132 1 0
G 7 1 -1 2 19 2 13 0 0 0.0132 1 0
G 13 2 64 67 18 19 2 7
G 13 2 61 65 17 18 2 6
G 13 2 58 62 16 17 2 5
G 13 2 57 59 15 16 2 3
G 13 2 86 90 18 19 2 7
G 13 2 84 87 17 18 2 6
G 13 2 81 85 16 17 2 5
G 13 2 79 82 15 16 2 3
G 13 2 104 106 18 19 2 7
G 13 2 103 105 17 18 2 6
G 13 2 102 104 16 17 2 5
G 13 2 100 103 15 16 2 3
P 2 1.0 1.0 1.0 0.0 0.0
P 3 12 4 13 4
I 1 0
I 2 0
I 3 0
I 4 0
S 1 0.0011 0.13
S 2 0.00085 0.105
S 3 0.0006589 0.083
S 4 0.00015 0.015
N 0 1 0.16
N 0 2 0.34
N 0 3 0.34
N 0 4 0.16
B 0 22 2 124 19
W 1 68 0.0132 0.28975
W 2 5 1 40 70 95 115
K 1 360 60000
K 2 0 1
K 3 0.8 0.8 0.8 0.2 0.5 0.5
K 4 1 1 1 5 1 1
K 5 1 1 1 1 1 1
```

T sediment flow through 90 degree bend, Group B, alignment 30
F 2 RIS
F 4 0.5 50 0.001
F 7 BG
F 11 2.65 0.037
F 33 50 1
F 37 1
F 54 0.001
F 56 10 0.5
F 84 1
G 1 124 19 13 4
G 3 0 5 10 20 30 40 50 60 70 80 90 95 100
G 7 0 1 2 19 2 13 0 0 0.0132 1 0
G 7 1 -1 2 19 2 13 0 0 0.0132 1 0
G 13 2 64 67 18 19 2 7
G 13 2 61 65 17 18 2 6
G 13 2 58 62 16 17 2 5
G 13 2 57 59 15 16 2 3
G 13 2 86 90 18 19 2 7
G 13 2 84 87 17 18 2 6
G 13 2 81 85 16 17 2 5
G 13 2 79 82 15 16 2 3
G 13 2 104 106 18 19 2 7
G 13 2 103 105 17 18 2 6
G 13 2 102 104 16 17 2 5
G 13 2 100 103 15 16 2 3
G 23 60 66 16 19 6
G 23 57 63 15 18 5
G 23 56 60 14 17 3
G 23 83 88 16 19 6
G 23 80 86 15 18 5
G 23 80 83 14 17 3
G 23 102 106 16 19 6
G 23 101 105 15 18 5
G 23 99 104 14 17 3
P 2 1.0 1.0 1.0 0.0 0.0
P 3 12 4 13 4
I 1 0.0
I 2 0.0
I 3 0.0
I 4 0.0
S 1 0.0011 0.13
S 2 0.00085 0.105
S 3 0.0006589 0.083
S 4 0.00015 0.015
N 0 1 0.16

N 0 2 0.34
N 0 3 0.34
N 0 4 0.16
B 0 22 2 124 19
W 1 68 0.0132 0.28975
W 2 5 1 40 70 95 115
K 1 360 60000
K 2 0 1
K 3 0.8 0.8 0.8 0.3 0.5 0.5
K 4 1 1 1 5 1 1
K 5 1 1 1 1 1 1